VELOCITIES OF LONG PERIOD SURFACE WAVES AND MICROSEISMS AND THEIR USE IN STRUCTURAL STUDIES

PART I - MANTLE LOVE AND MANTLE RAYLEIGH WAVES AND THE STRUCTURE OF THE EARTH'S UPPER MANTLE

PART II - MICROSEISMS AND THEIR APPLICATION TO SEISMIC EXPLORATION

Thesis by

M. Nafi Toksöz

In Partial Fulfillment of the Requirements

For the Degree of

Doctor of Philosophy

California Institute of Technology

Pasadena, California

1963

GENERAL INTRODUCTION

The use of the dispersive properties of surface waves in studying the structure of the earth's crust and mantle has been one of the most powerful tools in seismology. The phase and group velocities of both Love and Rayleigh waves in the period range of 10 seconds to several minutes are being measured, and the elastic parameters with depth are being determined by comparing experimental velocity curves and those of the theoretical models. Waves of different wavelengths penetrate to different depths within the earth, and the structure to any depth can be investigated using waves in the appropriate period range. For instance, in the study of the earth's upper mantle the waves with periods of 50 to 400 seconds or longer must be used. In the investigation of very shallow crustal structures by the dispersion method, one has to work with surface waves whose periods are of the order of a few seconds.

In this paper the use of both very long and very short period surface waves are demonstrated in two parts. Part I is devoted to precise measurement of phase velocities of earthquake generated Love and Rayleigh waves over multiple paths. The various models for the earth's upper mantle are re-evaluated in the light of these new data, and two new models are computed. In Part II the phase velocity method is extended to short period, continuous

(non-transient), and somewhat random, surface waves. In this case the velocities of microseisms in the period range of 1 to 6 seconds are measured with the purpose of determining the very shallow structures in the earth's crust.

PART I

MANTLE LOVE AND MANTLE RAYLEIGH WAVES AND THE STRUCTURE OF THE EARTH'S UPPER MANTLE

ACKNOWLEDGEMENTS

The author is grateful to Professor Frank Press for his support and encouragement throughout this study. Many valuable discussions were held with Drs. D. L. Anderson and A. Ben-Menahem. Their cooperation and support is acknowledged with gratitude. The author also wishes to extend his thanks to Mr. S. S. Alexander for the use of some of his computer programs.

This research was supported by Grant No. AF-AFOSR-25-63 of the Air Force Office of Scientific Research as part of the Advanced Research Projects Agency Project VELA.

Mr. L. Lenches' help in preparation of the figures is acknowledged with special thanks.

ABSTRACT

Phase velocities of Love waves from five major earthquakes are measured over six great circle paths in the period range of 50 to 400 seconds. For two of the great circle paths the phase velocities of Rayleigh waves are also obtained. The digitized seismograph traces are Fourier analyzed, and the phase spectra are used in determining the phase velocities. Where the great circle paths are close, the phase velocities over these paths are found to be in very good agreement with each other indicating that the measured velocities are accurate and reliable. Phase velocities of Love waves over paths that lie far from each other are different, and this difference is consistent and much greater than the experimental error. From this it is concluded that there are lateral variations in the structure of the earth's mantle.

The phase velocity data are compared with theoretical dispersion curves of seven different earth models. None of these models fit the data. Two new upper mantle models, one to fit the data over an almost completely oceanic path and the other over a mixed oceanic and continental path, are designed. The significant features of these models are correlated with the body wave observations and with the hypothesized thermal model and the mineralogical structure in the mantle.

TABLE OF CONTENTS

INTRODUCTION

The investigation of the earth's mantle, and especially the upper mantle, is one of the current fields of interest in seismology. The properties of both the seismic body waves and surface waves are being utilized in these investigations. The questions for which answers are being sought are the following: 1. What is the structure of the mantle, and how do the elastic parameters vary with depth? 2. Is the upper mantle laterally homogeneous or inhomogeneous? 3. If inhomogeneous, how significant are the variations, and can they be correlated with oceans and continents? At the present time, some answers to the above questions are available. However, the data on which these answers and conclusions are based are sketchy, and in some cases are not accurate enough to be conclusive. This project was undertaken to obtain more accurate surface wave dispersion data and to answer the above questions in the light of these new data.

Most of the earlier information regarding the velocities of compressional and shear waves in the earth's mantle were obtained from body wave studies. Both travel time and amplitude information were utilized in these studies. For most regions within the earth's mantle, the velocity increases continuously as a function of depth, and

the travel time method can be used to obtain the velocity distribution. In the lower mantle (below the depth of 800 km) where the velocity variation is regular, the results of different investigators are in very good agreement (Gutenberg, 1959a; Jeffreys, 1959). In the upper mantle, however, the velocity structure is far from being regular. Where the velocity decreases with depth at a rate greater than $\frac{v}{r}$ (i.e. $-\frac{dv}{dr} + \frac{v}{r} < 0$), and where it varies discontinuously, the direct application of the travel time method fails (Bullen, 1961). This failure is the main reason for the discrepancies in various upper mantle models deduced from body wave data.

Using some indirect methods, such as the travel times of deep focus earthquakes and the amplitudes of the P and S waves, upper mantle velocity structures were determined in certain areas. The results of numerous investigations in this field are summarized by Anderson (1963) and Nuttli (1963). At this stage, other than the presence of the low velocity layer, there is no consistent picture about the details of the velocity structure between depths of 100 and 500 kms. Part of the disagreement may be due to regional variations, but with the available data it is not possible to isolate these changes.

The nature of the velocity variations immediately below the Mohorovičić discontinuity has been investigated

by deep seismic soundings in selected regions of the world. These studies have disclosed significant differences in Moho velocities (7.4 to 9.0 km/sec) in different areas (Aki, 1961; Aver'yanov, et. al., 1961; Beloussov, et. al., 1962; Healy, et. al., 1962; Pakiser and Hill, 1962). To what depth these strong lateral variations extend is a question that would most likely require the application of surface wave dispersion methods rather than indirect techniques using body wave data.

The use of the surface wave data in studying the upper mantle velocity structures has several advantages. First of all, the dispersion method does not fail in the presence of a low velocity layer or rapid velocity changes. Second, the surface waves can be used to determine average structure between the source and the station, or between two stations over regions inaccessible to body wave studies. The third advantage is the adequacy of a single seismogram to compute a dispersion curve over a path, and thus to interpret the structure for this path. With the utilization of high speed digital computers for computing theoretical dispersion curves, the major obstacle in the use of surface wave data has been eliminated. Today, however, the most serious shortage is accurate dispersion data over different regions.

The period range of surface waves most suitable for the study of the upper several hundred kilometers of the mantle is 60 to 400 seconds. At shorter periods the local effects on the waves are such that only regional, rather than universal, dispersion curves are justified. At very long periods, free oscillation data have fixed the phase velocity curves for both Love and Rayleigh waves (MacDonald and Ness, 1961; Smith, 1961; Bolt and Marussi, 1962). For the intermediate periods, there have been many measurements of phase and group velocities of Love and Rayleigh waves (Satô, 1958; Nafe and Brune, 1960; Brune, Ewing, and Kuo, 1961; Brune, Benioff, and Ewing, 1961; Båth and Arroyo, 1962; Ben-Menahem and Toksöz, 1962; Kuo, Brune, and Major, 1962; Matumoto and Satô, 1962). Most of the observational data, and especially those of Love waves, are scattered. Various measurements differ by as much as, and occasionally more than, one percent of the measured value (Kovach and Anderson, 1962). Part of this variation may be due to path differences and lateral variations. Before this question and the question of the best model for the earth's mantle can be resolved, it is essential that more precise and consistent surface wave dispersion data are obtained.

In this study, the phase velocities of Love waves are measured over six complete great circle paths from five

major earthquakes: New Guinea (February 1, 1938), Assam (August 15, 1950), Kamchatka (November 4, 1952), Mongolia (December 4, 1957), and Alaska (July 10, 1958). For two of these, Assam and Mongolia, phase velocities of Rayleigh waves are also determined. The epicenter, origin time, and other pertinent information regarding these earthquakes are given in Table I. The great circle paths are through Pasadena, California with one exception: Wilkes, Antarctica is used in addition to Pasadena for the Alaska earthquake. Figure 1 shows the great circle paths through Pasadena and Wilkes. With the exception of New Guinea, and Alaska-Wilkes, all paths are fairly close to one another, and one would expect the measured phase velocities to be approximately the same regardless of the lateral variation in the mantle structure.

The second half of this study is devoted to the determination of the upper mantle velocity structure for the different great circle paths. Then, the different structures are compared to determine the extent of the lateral variations. Until now, a few comparisons of this nature were made using only Rayleigh wave data, and flat models. From Rayleigh wave group velocity studies it was found that the structure of the uppermost part of the mantle is different under the Pacific Ocean from that under the continents (Dorman, Ewing, and Oliver, 1960; Aki and

Press, 1961). The difference between the Pacific mantle and the continental mantle was explained either by a reduction in the shear velocity of the low velocity layer under the ocean or by making the low velocity zone shallower. Phase velocities of Rayleigh waves in the period range of 30 to 140 seconds were measured by Kuo, Brune, and Major (1962) over different paths in the Pacific. From a comparison of their data, it was concluded that the uppermost portion of the mantle is fairly uniform under the Pacific Basin but must be different under the disturbed marginal areas.

The above comparisons were made on the basis of a flat layered earth. Since the effect of sphericity on phase velocities of mantle Love and mantle Rayleigh waves cannot be ignored (Bolt and Dorman, 1961; Kovach and Anderson, 1962; Sykes, Landisman, and Satô, 1962; Anderson and Toksöz, 1963), in this study the theoretical curves are computed for spherical earth models.

PHASE VELOCITY DETERMINATION USING FOURIER PHASE SPECTRA

The phase velocity determination involves the measurements of the phase delay of each component of the wave over a known distance. This can be done exactly by using the Fourier phase spectra, or approximately by measuring the time delay directly from the seismogram. The idea behind the direct time domain measurement is that one may associate a sine wave with each peak or trough of the dispersed wave train (Brune, Nafe, and Oliver, 1960). Then, a period can be assigned to each peak and trough. The condition of a long fully dispersed train, however, is an essential requirement. In the case of mantle Rayleigh waves, this condition is met, and the phase velocities measured utilizing the time domain and the Fourier phase spectra are in very good agreement (Ben-Menahem and Toksöz, 1962).

The mantle Love waves, which are also called G waves, are not dispersed like the Rayleigh waves in the same period range. The Love wave group velocity curve is flat between 100 and 300 seconds, and regardless of the distance traveled, the wave retains a pulse-like shape. The phase velocities in this case cannot be measured directly from time domain records without violating the dispersion condition and without encountering practical

difficulties. This is the main reason for the scarcity of the G wave phase velocity data, and for the large uncertainties in phase velocities measured directly from the seismogram.

The Phase Spectra Method

In the Fourier analysis method the time delays of each frequency are determined using the phase spectra. This method was first introduced to seismic velocity measurements by Valle (1949) and applied to G waves by Satô (1958). The present study, however, constitutes the first extensive application of this method for precise phase velocity measurements of mantle Love and Rayleigh waves.

Let us take two recording stations over the same great circle path, with distances Δ_1 and Δ_2 from the epicenter. Assume that a Love or Rayleigh wave train is recorded at both stations. The desired wave train can be digitized and Fourier analyzed. Let t_1 and t_2 be the travel time from the source to the beginning of each Fourier window, and let $\phi_1(\omega)$ and $\phi_2(\omega)$ be the corresponding Fourier phase spectra. Then, the phase velocity C is given by

$$C(T) = \frac{\Delta_2 - \Delta_1}{t_2 - t_1 + T\left[(\phi_2 - \phi_1) + N\right]} \qquad (1)$$

where T is the period and N is an integer. The need for N arises from the fact that the trigonometric functions are multi-valued, and one cannot determine uniquely the initial integer of Φ_2 relative to Φ_1. Once N is fixed, it remains unchanged over the whole spectrum. The changes in phase will normally exceed one circle, and every time Φ goes through zero it is incremented by one.

When the phase velocities are determined from a single station, two successive passages of the same wave in the same direction such as G_1 and G_3, $G_2 - G_4$, or $R_3 - R_5$ are used for determining the phase velocity. In this case equation 1 becomes

$$C(T) = \frac{\Delta_o}{\delta t + T\,(\delta \Phi + N - \frac{1}{2})} \qquad (2)$$

where Δ_o = length of great circle, $\delta t = t_{n+2} - t_n$, $\delta \Phi = \Phi_{n+2} - \Phi_n$, and the $-\frac{1}{2}$ circle phase shift is due to two extra polar passages, with a $\frac{\pi}{2}$ phase shift per polar passage (Brune, Nafe, and Alsop, 1961).

The use of pairs of odd or even order surface waves in velocity measurement, rather than odd-even combinations, is necessary to avoid the possibility of introducing an error due to the unknown character of the source. The source may contribute in a different way to waves leaving it in opposite directions. An error of this kind arises, for example, from the finiteness of source (Ben-Menahem, 1961)

where the differential phase between displacements of two opposite-going surface waves is given by:

$$D\phi = \frac{\phi_{n+1} - \phi_n}{2\pi} = \frac{f}{C}(\Delta_o - 2\Delta_1 + b\cos\theta_o) + M + \tfrac{1}{4}$$

$$n = 1, 3, 5 \ldots \quad (3)$$

and a similar formula for even values of n. Δ_1 is the distance from the source to the station, b = fault length, θ_o = angle between the fault trace and the great circle path. The term involving $bCos\theta_o$ is due to the finiteness of the source, and a fault of 100 km can perturb the phase as much as 0.2 circle at the period of 100 seconds. This is a considerable error in the phase, and it cannot be neglected.

Numerical Procedure

The phase velocities were determined over six great circle paths using the Fourier analysis method described above. The pertinent waves were identified and traced from photographic seismograms. Then the traces were digitized for processing using a digital computer. In all cases, recordings from either strain or long period Press-Ewing seismographs were used. On these records the periods of the recorded signal and noise were 10 seconds or longer. In digitization a 2-second sampling interval was used to enable the filtering of the shortest periods and to minimize aliasing. The mean and linear trend were removed from

the data, and then each trace was filtered with a low-pass digital filter to eliminate the short period crustal surface waves and other short period interferences. The frequency response of a typical filter used is shown in figure 2.

The mantle Love waves have the characteristic shape of a pulse. In the case of first or second passages of the wave the pulse is concealed in the higher amplitude short period waves, and it is difficult to identify the beginning and the end of the pulse by inspecting the unfiltered seismogram. The filtering process clears the wave form of excessive interference and facilitates the choosing of the beginning and the end of the pulse. The effectiveness of this process can be seen by comparing the unfiltered G_2 pulse shown in figure 3a with the filtered pulse in figure 3b.

The mantle Rayleigh waves are dispersed more than the Love waves in the period range of 80 to 400 seconds, and their known group velocities can be used to determine the beginning and the end of the wave train. The velocity window is chosen using the lowest and highest group velocities in the period range of interest. The onset and the end times were computed from the known epicentral distance and the origin time using these velocities. In the case of Rayleigh waves from the Assam and the Mongolia earthquakes,

the window was chosen between 3.45 and 4.10 km/sec. The lower value corresponds to the minimum of group velocity at the Airy phase and the higher one to the wave with a period of 400 seconds.

PHASE VELOCITIES

The phase velocities of Love waves were determined over six great circle paths. For two of these paths the velocities of Rayleigh waves were also measured. The Love and Rayleigh phases used in these measurements are listed in Table 2. In the same table the onset and end times of each pulse, the cut-off frequency of the filter used, epicentral distance to station, and the length of the great circle through the epicenter and the station are also listed. The pulses were Fourier analyzed after the completion of the pre-analysis operations, and the phases were used in equation 2 to compute the phase velocities.

Love Waves

(a) Alaska Earthquake. The G_2 and G_4 phases recorded by E-W component on the Press-Ewing seismograph system were used in determining the phase velocities over a great circle path through Pasadena. The re-traced unfiltered and filtered pulses are shown in figure 3. The spectra are shown in figure 4. Phase velocities were also computed from $G_2 - G_4$ combination of the recordings at Wilkes. The original seismogram and the filtered traces are shown in figure 5. The spectra are given in figure 6. Although the recordings were excellent at this station, the drum speed was not uniform causing the results to be somewhat unreliable.

(b) Mongolia Earthquake. The unfiltered Pasadena strain seismogram showing G_1 and G_3 are shown in figure 7, and the spectra are given in figure 8. Phase velocities are listed in Table 3.

(c) Assam Earthquake. The Pasadena E-W strain recordings of G_1 and G_3 are used for phase velocity measurement. Seismogram traces are shown in figure 9, and the spectra in figure 10.

(d) Kamchatka Earthquake. G_2 and G_4 phases from the Pasadena recordings of this earthquake were used for the determination of the phase velocity. The original seismogram was exhibited by Satô (1958). The filtered traces, however, are given in figure 11, and the corresponding spectra in figure 12.

(e) New Guinea Earthquake. $G_1 - G_3$ and $G_2 - G_4$ combinations were used to obtain two sets of phase velocities for the same path. The original Pasadena strain seismogram along with spectra of these phases had been given by Satô (1958). Since this is a completely independent analysis, the filtered traces and spectra are shown in figure 13 and figure 14, respectively. The velocities are listed in Table 3.

Rayleigh Waves

(a) Mongolia Earthquake. The phase velocities of

Rayleigh waves were computed and published earlier (Ben-Menahem and Toksöz, 1962). These same values are listed in Table 4 after a slight correction was made for the length of the great circle path.

(b) Assam Earthquake. The phase velocities are computed from R_3 and R_5, for the great circle path through Pasadena. The amplitude and phase spectra are shown in figure 15 and the phase velocities are tabulated in Table 4. The original seismograms have already been exhibited by Ewing and Press (1954).

For the sake of an easy comparison, the phase velocities of the Rayleigh waves are plotted in figure 16, and those of the Love waves in figure 17.

Analytic Expressions for Phase and Group Velocities

The group velocities can be computed from the phase velocities, using the expression

$$U = \frac{d\omega}{dk} = \frac{C}{1 + \frac{T}{C}\frac{dC}{dT}} \qquad (4)$$

where U = group velocity, $k = \frac{2\pi}{\lambda}$ = wave number, and ω = angular frequency. The only difficulty in this computation arises from the differentiation of the phase velocity curve. This could be accomplished by either a direct numerical differentiation or representing the phase velocity curve by an analytic function and computing the

derivatives of this function. It was chosen to fit a polynomial of the form $P_n(T) = \sum_{i=0}^{n} a_i \dot{X}^i(T)$ to the data where the coefficients were determined by the method of least squares. Different polynomials of order n = 4 to n = 9 were used. The lower order polynomials miss the finer variations in the data, whereas the higher order polynomials follow any scattering that may be present in the original data resulting in undesired oscillations. The group velocities shown in figures 16 and 17 are the average values derived from two or more different order polynomials. It is important to mention that differentiation magnifies greatly the error that may be present in the phase velocity data, and the group velocities computed by this method are much less reliable than the phase velocities. In spite of this, these group velocities agree reasonably well with the velocities computed directly from the filtered records. The value of the method of computing the group velocity from the phase velocities is greater for Love waves than for Rayleigh waves. The group velocity curve of Love waves is nearly flat from T = 100 to T = 300 seconds. The wave disperses very little and tends to preserve its initial shape. Unless one performs an extensive amount of narrow band filtering, it is very difficult to compute group velocities for different periods. This is one of the reasons for the greater scatter in the time domain measurements of phase and group velocities of Love waves in this

particular period range (see Brune, Benioff, and Ewing, 1961, figure 7).

For more general use, simple functions can be fit to phase velocity data. For Rayleigh waves, one may write (Ben-Menahem and Toksöz, 1962)

$$C(T) = 3.85 + 0.0046T - 0.25 \sin (0.01T + 0.28)$$

$$100 < T < 500 \text{ seconds} \quad (5)$$

which is a good approximation. Also, the group velocities obtained from the above expression using equation 4 agree with the measured values. For Love waves one can utilize the nearly constant value of the group velocity in the plateau of the dispersion curve to derive an expression for the phase velocity (Satô, 1958). Differentiating the group velocity, and setting $\frac{dU}{dT} = 0$, one obtains the differential equation

$$2\left(\frac{dC}{dT}\right)^2 = C\,\frac{d^2C}{dT^2} \quad (6)$$

A solution to this equation is,

$$C = \frac{U_o}{1 - \alpha T} \quad (7)$$

where U_o is the constant value of the group velocity. It should be noted that equation 6 is approximate, since the group velocity in the plateau is not a true constant but varies slowly with the period. The values $U_o = 4.37$ and $\alpha = 5.35 \times 10^{-4}$ give a reasonably good fit to the observed

phase velocities (New Guinea excepted) between T = 100 and T = 300 seconds. This indicates that the group velocity curve is nearly constant over that period range.

Sources of Error in the Phase Velocity Measurements

It is important that the sources of error in phase velocity measurements are clarified before one can judge the accuracy of the various measurements. Here the errors involved in Fourier analysis method will be discussed briefly. In the phase velocity measurement with the Fourier analysis method using equation 2 only the phase term can be in error, provided the integer N is chosen correctly. The great circle distance may have an uncertainty of 10 km, but this will only result in a 0.025 percent error in phase velocity since

$$\frac{\partial C}{C} = \frac{\partial \Delta}{\Delta} \quad , \quad \Delta \approx 40{,}000 \text{ km} \qquad (8)$$

The error in the phases is due to interference, noise, digitizing, and numerical inaccuracies. The latter two quantities are random errors and will show as scattering in the data. The extent of this error can be estimated from the behavior of the phase spectra, and one finds that no measurable scattering occurs in the frequency range of interest. Errors that may result from "window-shaping," and inadequate detrending are discussed by Gratsinsky (1962), but these can be avoided by proper care in the analysis.

The interference (superimposition of two similar signals with a time delay, or two different signals with power in the same frequency range) is a serious problem in Fourier analysis. A typical indication of such interference is the presence of power-minima in the amplitude spectra accompanied by minima or turning points in the phase spectra (Pilant, 1962, personal communication). The effect of the interference on the phases, and the error introduced is difficult to evaluate without knowing the true nature of the interference. In the case of two similar signals, one of which is delayed relative to the other by Δt, the error in the phase is (Knopoff and Press, 1962)

$$\Delta \phi = \frac{\alpha \sin \omega \Delta t}{\omega} \tag{9}$$

where α is the normalized amplitude of the delayed signal. The amplitude spectra of the original pulse is modulated by the factor $(1 + \alpha \cos \omega \Delta t)$. The maxima and minima in the amplitude spectra corresponds to $(1 + \alpha)$ and $(1 - \alpha)$ from which α can be found. The maximum phase error, $|\Delta \phi|_{max} = \alpha \Delta t$, can be computed if Δt is known.

The error in the phase velocity due to phase inaccuracies is found by differentiating equation 2 with respect to $\delta \phi$

$$\frac{\partial C}{C} = - \frac{CT}{\Delta} \partial(\delta \phi) \tag{10}$$

From equation 10 one observes that the fractional error in phase velocity is inversely proportional to distance Δ. Therefore, as the distance increases the relative effect of the phase errors decreases. This is one of the main reasons for obtaining more precise results when phase velocities are measured over a complete great circle path.

Discussion of the Accuracy of the Results

The phase velocities listed in Tables 2 and 3 are probably within 0.5 percent of the correct value. Since the absolute values were not previously known, reproducibility and the agreement between different measurements are the major bases for the judgment of accuracy. In examining the values listed in Tables 3 and 4 one observes that for the Mongolian and Assam earthquakes, the phase velocities agree with less than a 0.02 km/sec discrepancy, over a wide frequency range, for both Love waves and Rayleigh waves. Phase velocities of Love waves from the Alaska earthquake (through Pasadena) agree with those of Assam and Mongolia, while Kamchatka yields slightly lower phase velocities. The New Guinea-Pasadena path has the highest values of phase velocities of all the paths. As to the reliability of the New Guinea results, it can be pointed out that the agreement between $G_1 - G_3$ and $G_2 - G_4$ combinations is excellent. These results are also in accord

with Satô's measurements as given by Brune, Benioff, and Ewing (1961). It should be noted here that the New Guinea-Pasadena great circle path is quite different from the other paths, being almost entirely oceanic. Alaska-Wilkes great circle phase velocities are between those of New Guinea and Mongolia. The slope of the phase velocity curve, however, is greater than the slopes of the others shown in figure 17. This discrepancy may be due to the larger error in the Wilkes phase velocities compared to the others. It is also possible that the Alaska-Wilkes path represents a considerably different structure than the other paths.

The group velocities for different paths vary in a manner similar to the variation of phase velocities. For the close paths (Mongolia, Alaska, Assam), the group velocities computed from the phase velocities and the group velocities measured from the seismograms agree. The New Guinea-Pasadena path, on the other hand, has considerably higher group velocities than the others. In computing the group velocities from the seismograms, no attempt was made to correct for source effects. In the case of major earthquakes, the effect of source finiteness could be significant, and is given by the following expressions (Press, Ben-Menahem, and Toksöz, 1961)

$$U' = \frac{U}{1 + \frac{b}{2\Delta}\frac{U}{V_f} - \cos\theta_o} \approx U\left[1 - \frac{b}{2\Delta}\left(\frac{U}{V_f} - \cos\theta_o\right)\right] \quad (11)$$

where $U = \frac{d\omega}{dk}$, $U' = \frac{\Delta}{t}$ is the group velocity as measured from the seismogram, b = fault length, V_f = rupture velocity along the fault, and θ_o = azimuthal angle. This could explain the observed apparent delay of the arrival of G_1 of the Assam earthquake by as much as 170 seconds (arrival group velocity of 4.07 km/sec instead of the usual 4.35 - 4.40 km/sec). For the Mongolia earthquake the source mechanism is known, and b = 560 km, V_f = 3.5 km/sec, $\theta_o = 70^o$ (Ben-Menahem and Toksöz, 1962). Then, the apparent group velocity U' should be about 2 percent less than U. The maximum of the envelope of the Mongolia G_1 pulse arrives with a velocity of 4.25 km/sec, which is in agreement with the predicted apparent group velocity. It should be mentioned that the group velocities which were computed from the phase velocities are true group velocities, rather than U', since the phase velocities were computed from successive odd or even order wave trains.

UPPER MANTLE MODELS

Before evaluating the validity of the several models for the earth's upper mantle in the light of the new data, one can derive some conclusions with regard to lateral structural variations. Examining the great circle paths shown in figure 1 and the corresponding phase velocities in figures 16 and 17, one can see that the agreement between phase velocities is very good where the paths are close. Where the paths are quite different, there are consistent variations in the phase velocities of the Love waves, and these are more pronounced at the shorter periods. The very obvious conclusion regarding the earth's upper mantle is that the structure and the velocities vary laterally. At the present there are not sufficiently reliable Love wave phase velocity data to definitely correlate these with the oceans and the continents. The New Guinea-Pasadena path has the highest percentage (89 percent) of ocean compared to paths from Mongolia, Alaska, and Kamchatka (average 65 percent). The New Guinea phase velocities are higher than the others.

Comparison of the Data with Mantle Models

Let us now compare these new data with the theoretical curves for five different earth models determined in earlier studies. These models combine the velocity curves given

by Gutenberg, Lehman, and Jeffreys with the upper mantle density-depth curves of Bullen and Birch. Figures 18 and 19 show the shear velocity and density variations with depth for these models (Kovach and Anderson, 1962). Because of the strong curvature effect, only the theoretical curves computed for the spherical earth are used in the comparison.

The paths for the data are not completely oceanic nor completely continental. One would expect that the theoretical phase velocity curves of the oceanic models should fall above the data, and those of the continental models to fall below the data. Figure 20 shows the theoretical Rayleigh wave dispersion curves for the five models (Anderson, 1963) and the observed phase and group velocity data over Mongolia-Pasadena and Assam-Pasadena complete great circle paths. Leaving out the Gutenberg-Bullen B curve which has the wrong slope, both the continental and oceanic theoretical phase velocities are higher than the observed. The closest fitting model is the Gutenberg-Bullen A, and for this also, the theoretical curve is slightly higher than the data for the periods longer than 150 seconds. The group velocity curve for this model is in fairly good agreement with the observed data.

A good earth model should fit both the Rayleigh and Love wave data. In figure 22 the theoretical phase and group velocity curves for the Gutenberg-Bullen A continental

model are compared with the observed Love wave data over the same Mongolia-Pasadena and Assam-Pasadena great circle paths. The agreement between the theoretical and observed curves is good for the periods longer than 200 seconds. For shorter periods, however, the theoretical curve falls considerably below the observed data.

Let us discuss two other upper mantle models which are described in the recent literature. These are 8099 and CIT-6, and their shear velocity profiles are shown in figure 21. 8099 was designed as an oceanic model to fit the observed group velocities of the Rayleigh waves (Dorman, Ewing, and Oliver, 1961). The theoretical group velocity curve was computed using a flat layered earth, and it agrees with the data reasonably well up to a period of 200 seconds, but for longer periods the theoretical curve is much higher than the data. The correction for sphericity would improve the fit for long periods, but the whole curve is slightly higher than the data (Anderson, 1963). The theoretical Love wave phase velocities for this model were computed by Sykes, Landisman, and Satô (1962) using a spherical earth program. The structure that was used in the computation is referred to as Case 122. The theoretical phase velocity curve is higher than all the existing data for periods longer than 200 seconds. Thus, one has to conclude that the 8099 (or Case 122) is not a completely

satisfactory model in the light of both Love and Rayleigh wave dispersion data.

CIT-6 mantle model is an oceanic structure with a Gutenberg type low velocity channel and a Birch density distribution (Kovach and Anderson, 1962). The theoretical Love wave phase velocity curve for a spherical earth is in agreement with the Mongolia-Pasadena data up to about 170 seconds. For longer periods (up to 400 seconds), however, the data fall much below the theoretical curve.

New Models

The comparison of the theoretical dispersion curves with the data shows that all the reference models described above fail to fit the new data well over the entire frequency range where phase velocities are available. Because of this disagreement, it was necessary to design new mantle models that would fit the data. In examining Table 3 and figure 17, one sees that there are two distinct trends in the measured phase velocities. The New Guinea-Pasadena path is definitely identified with higher phase and group velocities compared to the others, which are in close agreement among themselves. Two different structures, CIT-11 and CIT-12, were synthesized to fit these two groups of data. In the computation of the theoretical Love wave dispersion curves, a spherical dispersion program was used (Anderson and Toksöz, 1963). The process of structure

fitting was speeded up greatly by the utilization of the computed tables of partial derivatives of phase velocity with respect to rigidity and density (Anderson, 1963). In the case of Rayleigh waves, the theoretical phase velocities at eigenfrequencies were computed using a spheroidal oscillation program (Alsop, 1963).

The New Guinea-Pasadena great circle path is about 90 percent oceanic. CIT-11 theoretical model is designed for this particular path, and it is an oceanic model. The theoretical Love wave phase and group velocities are shown in figure 22 and the shear velocity profile in figure 23. The complete list of the velocity and density parameters with depth is given in Table 5. From figure 22, one sees that the agreement between the theoretical and observed phase velocities is excellent. There is no Rayleigh wave data available for this particular path, and it is not possible to check the consistency of this model for both Love and Rayleigh waves.

The Mongolia, Assam, Kamchatka, and Alaska-Pasadena paths are fairly close to each other, and in the average are about 65 percent oceanic. Model CIT-12 was designed for these particular mixed paths, and it represents a weighted average between a completely continental and a completely oceanic model. The biggest difference between the oceanic and continental areas is in the crust which is

about 5 - 10 km thick under the oceans and 30 - 50 km under the continents. This difference was taken into account in the CIT-12 model by stretching both continental and oceanic crusts over the whole great circle path. This does not change the velocities but reduces the thicknesses. The variation of the elastic parameters with depth for CIT-12 are listed in Table 6 and the shear velocity profile is plotted in figure 23 for comparison with that of CIT-11. Figure 24 illustrates the theoretical phase and group velocity curves of CIT-12 with the mixed path data. Free oscillation data and the long period phase and group velocities of Brune, Benioff, and Ewing (1961) are also plotted to extend the comparison to 500 seconds. Over the entire band (80 - 530 seconds) the agreement obtained is excellent.

The compatibility of CIT-12 model with the observed Mongolia and Assam Rayleigh wave data was also checked. The compressional velocities were initially computed from the shear velocities using the Poisson's ratios at various depths given by Gutenberg (1959b). Then these velocities were increased by about 0.1 km/sec between the depths of 50 and 200 km to improve the fit. The comparison of the theoretical phase velocity curve with the observed Rayleigh wave data is shown in figure 25. The agreement is very good for periods longer than 200 seconds. For shorter

periods, the theoretical curve is slightly below the data. It should be mentioned here that the accuracy of the data is questionable below 140 seconds. There is an unusual "hump" in the phase velocity curve centered around the 130 second period. Also, as one observes in figure 25, the phase velocities listed by Brune, Nafe, and Alsop (1961) for the Assam-Pasadena path and those reported herein are not in very good agreement below 140 seconds. For longer periods these two independently determined phase velocities are in excellent agreement. This suggests that the discrepancy between the data and the theoretical phase velocities may very well be due to the inaccuracy of the measurements rather than the slight incompatibility of the model.

A question may arise with regard to the uniqueness of the models CIT-11 and CIT-12. The possibility of finding two different models to fit the same dispersion data cannot be ruled out. However, if the data is fitted over a wide frequency range with one model, it is very unlikely that another model with grossly different velocity structure can be found to fit the same data. Each layer within the earth has the maximum effect on the phase velocity of Love waves at some period T_o. The contribution of this layer to the velocities becomes less at the periods far from T_o. The phase velocity at a given period is determined by the

weighted effects of all the layers within the earth. The effect of one layer cannot be compensated for over the entire frequency band by changing the parameters of another layer. The phase velocity data has a finite accuracy. Some small variations could be made in the shear velocity structures of the CIT-11 and the CIT-12 without affecting the quality of the agreement between the data and the theoretical dispersion curves. The more significant features of the velocity profiles, such as the wide low velocity zone, rapid velocity increases around the depths of 400 and 700 km, could not be replaced by smoother velocity variations.

Another problem regarding the uniqueness of the mantle models arises from the fact that there are more than one elastic parameters which control the velocities of the surface waves. Love wave velocities are affected by the shear velocity and the density, leaving out the geometry, of each layer. In the case of Rayleigh waves the compressional velocity is still another parameter, although its effect is very small compared to that of the shear velocity. These different parameters are constrained, and they cannot be changed freely. The velocity constraints are the travel time data of body waves and a reasonable value for the Poisson's ratio. The density distribution must satisfy the known values of the total mass and the moment of inertia of

the earth, and the empirical linear relation with the P-wave velocity obtained by Birch (1961). From the surface wave data, the most accurately determined elastic parameter is the shear velocity, since it affects the dispersion most strongly. Therefore, the shear velocity profiles of the models CIT-11 and CIT-12 are more reliable than the compressional velocity and the density profiles.

DISCUSSION

In the previous section it was pointed out that the existing mantle models did not fit the new data, and two new models were designed. Among these, CIT-11 was constructed to fit the oceanic New Guinea Love wave data, and CIT-12 to fit the Love and Rayleigh wave data from Mongolia and Assam. In this chapter these two models will be compared with the others, and their characteristic features as well as the significance of these features in the light of other geophysical evidence will be discussed.

Let us compare the shear velocity profiles of CIT-11 and CIT-12. These are shown in figure 23. Both models are characterized by a thick low-velocity zone extending from about 50 km below the surface to a depth of 350 km. CIT-11 has a channel between 80 and 160 km in which the shear velocity drops to a minimum value of 4.34 km/sec. From 160 to 360 km the velocity is a constant 4.5 km/sec. Below 360 km, the velocity increases very rapidly for 100 km to reach a value of 5.4 km/sec at a depth of 450 km. There is another rapid increase in the velocity at 700 km depth, where there is a 0.5 km/sec jump from 5.7 km/sec to 6.2 km/sec. Below 800 km the shear velocity behavior is smooth and in agreement with that of Gutenberg (1959a).

The shear velocity profile of CIT-12 is similar to that of CIT-11 with the difference in velocities at a given

depth in general being less than 0.1 km/sec. There are some distinct differences between the two models in the low-velocity zone. CIT-12 does not have a channel around 100 km depth. In fact, the velocity remains nearly constant from 90 km below the surface to 350 km with a value of 4.4 km/sec. There is a very shallow secondary channel between 190 and 310 km depths. From 350 km to 460 km the velocity increases rapidly in a manner similar to CIT-11. Below 460 km the two models, CIT-11 and CIT-12, are identical.

There are three outstanding features of these two new models which the other mantle models do not have. These features are: (1) The extreme thickness of the low-velocity zone, (2) the rapid and significant increase of the velocity between 350 km and 450 km, (3) another anomalous velocity increase around 700 km depth. Let us discuss these features in detail.

Low-Velocity Layer

Both of the new mantle models confirm the existence of the low-velocity layer for shear waves. This is not surprising, however, since the presence of such a zone for S-waves in the upper mantle of the earth is generally accepted. The body wave studies have not been conclusive in determining the depth of the lower boundary of the channel. The results will be discussed in connection with the "20° discontinuity." For some reason the models designed

in the light of surface wave dispersion data have not extended this zone below 250 km. Numerous investigators have ended the low shear velocity zone at depths less than 250 km (Dorman, Ewing, and Oliver, 1960; Aki and Press, 1961; Kovach and Anderson, 1962; Sykes, Landisman, and Satô, 1962; Anderson, 1963). In our models, however, shear velocities are 4.5 km/sec or less to a depth of 350 km. This is necessary to fit the data for periods longer than 200 seconds. In the case of 8099 (Dorman, et. al., 1960; Anderson, 1963) the theoretical group velocity curve was, on the average, above the Rayleigh wave data. A similar discrepancy is demonstrated by Case 122 (Sykes, et. al., 1962) and CIT-6 (Kovach and Anderson, 1962) where spherical Love wave phase velocity curves are higher than the data for periods of 200 seconds and longer. Hence, it is not at all conflicting with other investigations to extend the low-velocity zone down to the depth of 350 km. Also, Gutenberg (1959a, p. 84) states that "The 'low-velocity' channel ends approximately at the depth where the maximum velocity existing at or near the top of the mantle is reached again, that is at a depth of about 250 km for P, 350 km for S. Both depths are not well defined...."

The behavior of compressional velocities with depth for model CIT-12 is illustrated in figure 26. The P-profile is almost parallel to that of the S. Within the low-velocity

zone, however, there are some differences. First of all, the "channel" in the P-profile is not as deep as that of the S-profile. Second, the deepest part of the P channel is between 80 and 180 km, whereas in the case of S, it is between 200 and 300 km. Third, the P-wave velocities start increasing at 200 km, although this increase is small compared to the change at 350 km. It should be mentioned that the effect of the P velocities on the Rayleigh wave phase velocity curve is very much less than that of S velocities. As a result, one does not have as much control on the P-profile as on the S-profile.

The presence of a low-velocity layer can partly be explained in terms of the combined effects of pressure and temperature on the seismic wave velocities. In general, elastic velocities are increasing functions of pressure and decreasing functions of temperature. If the temperature gradient is such that temperature effect exceeds the pressure effect, a low-velocity zone would result. Various investigators (Birch, 1952; Valle, 1956; MacDonald and Ness, 1961) determined critical temperature gradients for the existence of a low-velocity zone. The values range from 6 to 10°C/km. The gradients for thermal models of Lubimova (1958) and MacDonald (1959) are compared with the critical gradients by Anderson (1963). The results show that between depths of 40 - 160 km, the gradients exceed the

critical, thus explaining the lowering of the seismic velocities in this zone. Below 200 km, however, this process cannot account for the presence of a low-velocity zone.

The excessive softening or partial melting of the rocks in the upper mantle would result in a lowering of the velocities, and especially of the shear velocity. Press (1961) hypothesized that rocks near the melting point in the low-velocity zone may be the source of the primary basaltic magma. Anderson (1963), comparing several temperature-depth models with the extrapolated melting curves of basalt and diopside, not allowing for any phase changes, stated that "Most of the solutions imply at least partial melting in the region between 100 and 400 km...." Partial melting, or excessive "softening" would lower the shear velocity more than the compressional velocity. In examining the velocity curves in figure 26, one observes that the S velocity decreases to a minimum below the depth of 200 km. This is the behavior one would expect in the case of partial melting starting at this depth. It should be mentioned that although this is a consistent picture, the changes in the velocities are very small. With the existing data, it is difficult to justify with certainty such small variations in the velocities. One definite feature, however, is that the S velocity does not increase in spite of the increasing pressure until the depth of 350 km.

In conclusion one can say that the low-velocity layers of models CIT-11 and CIT-12 extend from about 60 to 350 km. The lowering of the velocities may be explained in terms of high temperature gradients down to a depth of 200 km, and in terms of partial melting below this depth.

Discontinuities

In the upper mantle models CIT-11 and CIT-12 there are two particular depths around which the velocities increase rapidly. Both figures 23 and 26 illustrate this clearly. At the depth of 350 km both the shear and compressional velocities start to increase very rapidly. Although it is difficult to say whether the initial velocity increase is continuous or not, it is clear that the gradient is discontinuous at this depth. From 350 to 450 km there is a 1 km/sec increase in S velocity. Around 700 km the velocity gradient is not as high, but still much above the average gradients. The shear velocity increases by 0.5 km/sec between the depths of 650 and 750 km. The shallower "discontinuity" could well be the much discussed and controversial "20° discontinuity." The slope of the travel time curve changes abruptly at a distance of about 20°. This indicates the arrival of a refracted wave. The depth or the nature of the discontinuity responsible for the refraction has been a point of speculation and controversy.

Because of complications and uncertainties in the low-velocity zone, the direct application of the ray theory fails. From detailed investigations and auxiliary methods, the depth to the discontinuity is estimated anywhere from 220 km (Lehman, 1961) to 500 km (Jeffreys, 1952). Some investigators suggested depths between 350 and 400 km (Gutenberg, 1959a; Shirokova, 1959). Dorman, Ewing, and Oliver (1960) discussed the implications of the "20° discontinuity" in connection with the group velocities of Rayleigh waves. Their final oceanic model 8099, however, does not have any single outstanding discontinuity which may be identified as the "20° discontinuity." To summarize the present status, one may say that there is strong evidence for the presence of a "discontinuity" but the depth is highly uncertain.

The new models CIT-11 and CIT-12 not only confirm the presence of a "discontinuity," but also remove some of the uncertainty about the depth of this discontinuity. The sharp and significant increase in both shear and compressional velocities starting at a depth of 350 km clearly define a second order "discontinuity." Whether the velocities as well as the gradients are actually discontinuous cannot be settled. However, a truly discontinuous change in velocity at such a depth would be unlikely.

The shape of the discontinuity around the depth of 700 km is less clearly defined. From the surface wave studies one cannot determine how sharp this discontinuity is. Also the depth could be moved by about 50 km without seriously affecting the dispersion curves. The presence of such a change of slope in the velocity curves is clearly shown by the P and S velocity profiles of Gutenberg and Jeffreys (Gutenberg, 1959a). This shows that the new velocity curves converge with those of Gutenberg and Jeffreys at a depth where body wave results become reliable. Once again, this demonstrates the consistency of the models CIT-11 and CIT-12 with the existing data.

It would be of interest to investigate the causes of the "discontinuities" at depths of 350 and 700 km. Since such sharp features of the velocity cannot be explained as the effect of self-compression alone, some alternate explanations in terms of compositional and phase changes must be sought. One such explanation is a multi-stage phase change discussed by Ringwood (1962). At the pressures corresponding to the depth of approximately 400 km, it is determined that the pyroxene ($MgSiO_3$) to olivine (Mg_2SiO_4) transition would take place for enstatite. The extra silica released would exist in the high pressure form of quartz, as stishovite. Such a transition from lower to higher pressure phases of silicates could explain the rapid increase

of velocity starting at a depth of about 350 km. At an approximate depth of about 500 to 600 km, olivine to spinel conversion would further increase the density.

Other changes involving silicates to oxide and stishovite transitions would take place at depths greater than about 600 km (Ringwood, 1962). The "discontinuity" around 700 km, then, could be explained in terms of such a transition. It should also be mentioned that in a multi-component system the overall transitions would be spread over a substantial depth interval. These phase changes would also account for nearly all the increase in density between 300 and 800 km without the need for change in composition.

Anderson (1963) readjusted the boundaries of Bullen's region C in terms of the extremal points of a K/μ curve, where K is bulk modulus and μ is the rigidity. With this criterion the upper and lower boundaries of the region C are placed at 300 and 800 km, respectively. A very similar division can be made in terms of the velocity profiles shown in figure 26. The bottom of the low-velocity zone at the depth of 350 km can be chosen as the boundary between regions B and C. The lower boundary could be placed at 750 km, where the regular behavior of the velocity curves start. Such a division is also consistent with the lower

limits of the intermediate and deep focus earthquakes which are in general accepted to be at 300 and 700 km, respectively.

Anisotropy

A true earth model would explain both the observed Love and Rayleigh wave dispersion data over the same path. In earlier investigations it was found that when the Rayleigh wave phase velocity curve agreed with the data, the Love wave curve fell considerably below the data. Conversely, when the Love wave data were fitted, the theoretical Rayleigh curve was above the data. This discrepancy, together with other evidence, led to the idea that the upper mantle might be anisotropic (Anderson, 1962). An apparent anisotropy could result from the presence of thin isotropic layers. If the fine layering is not included in theoretical dispersion curve calculations, then a discrepancy between Rayleigh and Love wave results would arise. If the material within each layer is inherently anisotropic, then regardless of the layering used the isotropic computations would lead to a discrepancy between Love and Rayleigh wave results.

In comparing the theoretical phase velocity curves of CIT-12 with the Love and Rayleigh wave data of Assam and Mongolia earthquakes in figures 24 and 25, one does not see any discrepancy. In fact, the Rayleigh wave data is slightly

higher than the theoretical curve for periods below 200 seconds. At least for this particular great circle path, one can conclude that CIT-12 model fits both the Love and Rayleigh wave dispersion data without requiring anisotropy.

CONCLUSIONS

The conclusions derived from the measured phase velocity data of the mantle Love and the mantle Rayleigh waves, the comparison of the data with theoretical dispersion curves of earth models, and the significant features of the two new models designed are listed below.

(1) The phase velocity data of the mantle Love waves depend on the particular paths over which they are measured. The almost completely oceanic New Guinea-Pasadena path is identified with the higher phase and group velocities compared to the less oceanic Assam and Mongolia great circle paths. This indicates that there are lateral variations in the structure of the upper mantle.

(2) The dispersion curves of the standard mantle models do not fit the new Love and Rayleigh wave phase velocity data.

(3) The new models CIT-11 and CIT-12 are designed to fit the New Guinea-Pasadena and Mongolia-Assam group to Pasadena great circle paths. Leaving out the shallow crustal features, the differences between the two models are concentrated in the low velocity zone. Below 350 km the two models are very similar and below 450 km they are identical. This indicates that lateral inhomogeneities in the upper mantle are not likely to extend below about 400 km.

(4) The low-velocity zone for the shear waves extends down to 350 km, a depth which is greater than that suggested from earlier investigations. The lowering of the velocity may be explained as a combined effect of high temperature gradients and partial melting or softening, the former being more effective above 200 km, and the latter between 200 and 350 km.

(5) Two discontinuities are observed in the velocity gradient profiles. The shallower discontinuity starting at a depth of 350 km may be the much sought "20° discontinuity." The deeper discontinuity at 700 km is also indicated in the velocity profiles of Gutenberg and Jeffreys. These discontinuities could be explained in terms of phase changes. The possibility of composition change, however, is not ruled out.

(6) The dispersion curves of CIT-12 fit the Love and Rayleigh wave data measured over the same great circle path. It is not necessary to require the presence of an appreciable anisotropy in the upper mantle for this particular path.

(7) CIT-11 and CIT-12 models represent velocity distributions which are consistent not only with surface wave dispersion data, but also with the body wave results, the thermal models, and the thermodynamic and compositional studies.

REFERENCES

Aki, K., Crustal structure in Japan from the phase velocity of Rayleigh waves, Bull. Earthquake Res. Inst., Univ. of Tokyo, 39, 255-283, 1961

Aki, K., and F. Press, Upper mantle structure under oceans and continents from Rayleigh waves, Geophys. J. Roy. Astron. Soc., 4, 292-305, 1961.

Alsop, L. E., Free spheroidal vibrations of the earth, Part 1, Bull. Seism. Soc. Am., 53, 483-502, 1963.

Anderson, D. L., Surface wave dispersion in layered anisotropic media, Thesis, California Institute of Technology, 1962.

Anderson, D. L., Recent evidence concerning the structure and the composition of the earth's mantle, Physics and Chemistry of the Earth, 6, (in press), 1963.

Anderson, D. L., and M. N. Toksöz, Surface waves on a spherical earth. 1. Upper mantle structure from Love waves, J. Geophys. Res., (in press), 1963.

Aver'yanov, et. al., Deep seismic sounding in the zone of transition from the Asian Continent to the Pacific, Bull. (Izv.) Acad. Sciences USSR, Geophys. Ser., 169-184, 1961.

Båth, M., and A. L. Arroyo, Attenuation and dispersion of G waves, J. Geophys. Res., 67, 1933-1942, 1962.

Beloussov, V. G., B. S. Vol'vovski, I. S. Vol'vovski, and V. A. Ryaboi, Experimental investigation of the recording of deep reflected waves, Bull. (Izv) Acad. Sciences USSR, Geophys. Ser., 1034-1044, 1962.

Ben-Menahem, A., Radiation of seismic surface waves from finite moving sources, Bull. Seism. Soc. Am., 51, 401-435, 1961.

Ben-Menahem, A., and M. N. Toksöz, Source-mechanism from spectra of long-period seismic surface waves. 1. The Mongolian earthquake of December 4, 1957, J. Geophys. Res., 67, 1943-1955, 1962.

Birch, F., Composition of the earth's mantle, Geophys. J. Roy. Astron. Soc., 4, 295-311, 1961.

Birch, F., Elasticity and constitution of the earth's interior, J. Geophys. Res., 57, 227-286, 1952.

Bolt, B., and J. Dorman, Phase and group velocities of Rayleigh waves in a spherical, gravitating earth, J. Geophys. Res., 66, 2965-2981, 1961.

Bolt, B., and A. Marussi, Eigenvibrations of the earth observed at Trieste, Geophys. J., 6, 299-311, 1962.

Brune, J. N., H. Benioff, and M. Ewing, Long period surface waves from the Chilean earthquake of May 22, 1960, recorded on linear strain seismographs, J. Geophys. Res., 66, 2895-2910, 1961.

Brune, J. N., M. Ewing, and J. Kuo, Group and phase velocities for Rayleigh waves of period greater than 380 seconds, Science, 133, 3455, 1961.

Brune, J. N., J. E. Nafe, and L. E. Alsop, The polar phase shift of surface waves on a sphere, Bull. Seism. Soc. Am., 51, 247-257, 1961.

Bullen, K. E., Seismic ray theory, Geophys. J. Roy. Astron. Soc., 4, 93-106, 1961.

Dorman, J., M. Ewing, and J. Oliver, Study of shear velocity distribution in the upper mantle by mantle Rayleigh waves, Bull. Seism. Soc. Am., 50, 87-115, 1960.

Ewing, M., and F. Press, An investigation of mantle Rayleigh waves, Bull. Seism. Soc. Am., 44, 127-148, 1954a.

Gratsinsky, V. G., Distortions of seismic pulse spectra during analysis, Bull. (Izv.) Acad. Sciences USSR, Geophys. Ser., 233-239, 1962.

Gutenberg, B., Physics of the earth's interior, Academic Press, New York and London, 1959a.

Gutenberg, B., Wave velocities below the Mohorovičić discontinuity, Geophys. J. Roy. Astron. Soc., 2, 348-352, 1959b.

Healy, J. H., et. al., Crustal structure in the Western United States, Part IV, U. S. Geol. Survey report under VELA UNIFORM program, 1962.

Jeffreys, H., The earth, 3rd ed., Cambridge Univ. Press, London and New York, 1952.

Jeffreys, H., The earth, 4th ed., Cambridge Univ. Press, London and New York, 1959.

Knopoff, L., and F. Press, Study of the earth's crust in selected regions of the world, Final report, Univ. of California, Institute of Geophysics, Los Angeles, and California Institute of Technology, Seismological Laboratory, Pasadena, 1962.

Kovach, R. L., and D. L. Anderson, Long period Love waves in a heterogeneous spherical earth, J. Geophys. Res., 67, 5243-5255, 1962.

Kuo, J., J. Brune, and M. Major, Rayleigh wave dispersion in the Pacific Ocean for the period range 20 to 140 seconds, Bull. Seism. Soc. Am., 52, 333-358, 1962.

Lehman, I., The times of P and S in Northeastern America, Ann. di Geofis., 8, 351-370, 1955.

Lehman, I., S and the structure of the upper mantle, Geophys. J. Roy. Astron. Soc., 4, 124-137, 1961.

Lubimova, H. A., Thermal history of the earth with consideration of the variable thermal conductivity of its mantle, Geophys. J. Roy. Astron. Soc., 1, 115-134, 1958.

MacDonald, G. J. F., Calculations on the thermal history of the earth, J. Geophys. Res., 64, 1967-2000, 1959.

MacDonald, G. J. F., and N. F. Ness, A study of the free oscillations of the earth, J. Geophys. Res., 66, 1865-1912, 1961.

Matumoto, T., and Y. Satô, Phase velocity of long-period Rayleigh and Love waves as observed in the Chilean earthquake of May 22, 1960, presented orally at 43rd annual meeting American Geophys. Union, Washington, D. C.

Nafe, J. E., and J. N. Brune, Observations of phase velocity for Rayleigh waves in the period range 100 to 400 seconds, Bull. Seism. Soc. Am., 50, 427-439, 1960.

Nuttli, O., Seismological evidence pertaining to the structure of the earth's upper mantle, VESIAC State-of-the-Art Report, Institute of Science and Technology, Univ. of Michigan, 1963.

Pakiser, L. C., and D. P. Hill, Crustal structure in Nevada and southern Idaho from nuclear explosions, Crustal Studies Technical Letter No. 4, USGS, Denver, 1962.

Press, F., The earth's crust and upper mantle, Science, 133, 1455-1463, 1961.

Press, F., A. Ben-Menahem, and M. N. Toksöz, Experimental determination of earthquake fault length and rupture velocity, J. Geophys. Res., 66, 3471-3485, 1961.

Ringwood, A. E., Mineralogical constitution of the deep mantle, J. Geophys. Res., 67, 4005-4010, 1962.

Satô, Y., Attenuation, dispersion, and the wave guide of the G wave, Bull. Seism. Soc. Am., 48, 231-251, 1958.

Shirokova, E. I., Some facts on the character of the velocity change in the upper layers of the earth's mantle, Bull. (Izv.) Acad. Sciences USSR, Geophys. Ser., 1127-1137, 1959.

Smith, S., An investigation of the earth's free oscillations, Thesis, California Institute of Technology, 1961.

Sykes, L., M. Landisman, and Y. Satô, Mantle shear velocities determined from oceanic Love and Rayleigh wave dispersion, J. Geophys. Res., 67, 5257-5271, 1962.

Toksöz, M. N., and A. Ben-Menahem, Velocities of mantle Love and Rayleigh waves over multiple paths, Bull. Seism. Soc. Am., (in press), 1963.

Valle, P. E., Sulla misura della velocita di gruppo delle onde sismiche superficiali, Ann. di Geofis., 2, 370-376, 1949.

Valle, P. E., Sur gradiente di temperature necessario per la formazione di "low-velocity layers," Ann. di Geofis., 9, 371-377, 1956.

LIST OF TABLES

TABLE 1

List of Earthquakes and Coordinates of the Recording Stations

Name	Date	Origin Time	Epicenter	
			Latitude	Longitude
New Guinea	Feb. 1, 1938	19:04:21	05°00' S	131°30' E
Assam	Aug. 15, 1950	14:09:29	28°24' N	096°42' E
Kamchatka	Nov. 4, 1952	16:58:20	52°42' N	160°18' E
Mongolia	Dec. 4, 1957	03:37:45	45°15' N	099°24' E
Alaska	July 10, 1958	06:15:54	58°18' N	136°54' W
Stations	Pasadena, California		34°08'54"N	118°10'18"W
	Wilkes, Antarctica		66°35' S	110°35' E

TABLE 2

List of Phases, Filter Characteristics, and Epicentral Distances

Earthquake	Station	Phase	Time of the Pulse		Filter Cut-off (sec)	Epicentral Distance	Length of Great Circle
			Onset	End			
New Guinea	Pasadena	G_1	19:47:40	19:51:40	55	12194	40054
	Pasadena	G_2	20:48:04	20:53:02	55		
	Pasadena	G_3	22:17:52	22:24:40	55		
	Pasadena	G_4	23:16:40	23:23:48	55		
Assam	Pasadena	R_3	17:42:53	18:19:53	90	12174	40022
	Pasadena	R_5	20:23:53	21:30:51	90		
	Pasadena	G_1	14:57:23	15:01:23	67		
	Pasadena	G_3	17:27:47	17:36:33	67		
Kamchatka	Pasadena	G_2	19:05:06	19:10:26	100	6539	40032
	Pasadena	G_4	21:35:06	21:46:00	100		
Mongolia	Pasadena	G_1	04:16:15	04:21:50	80	10434	40018
	Pasadena	G_3	06:46:15	06:55:45	80		
Alaska	Pasadena	G_2	08:31:16	08:42:26	125	3025	40016
	Pasadena	G_4	10:59:52	11:15:18	125		
Alaska	Wilkes	G_2	07:38:00	07:48:12	125	16583	40018
	Wilkes	G_4	10:04:52	10:20:50	125		

TABLE 3

Phase Velocities of Love Waves

Frequency (cps)	Period (sec)	Phase Velocities (km/sec)						
		Mongolia G_3-G_1	Assam G_3-G_1	Alaska-Pasadena G_4-G_2	Kamchatka G_4-G_2	Alaska-Wilkes G_4-G_2	New Guinea G_3-G_1	New Guinea G_4-G_2
.0028	357.14	5.403		5.414				
.0030	333.33	5.317		5.331		5.324		
.0032	312.50	5.244		5.258	5.218	5.274		
.0034	294.12	5.181	5.155	5.193	5.167	5.221		
.0036	277.78	5.126	5.109	5.137	5.119	5.171		
.0038	263.16	5.078	5.070	5.089	5.076	5.123		5.113
.0040	250.00	5.036	5.034	5.047	5.037	5.078		5.074
.0042	238.09	4.998	5.002	5.010	5.002	5.037		5.038
.0044	227.27	4.965	4.973	4.977	4.971	5.001		5.007
.0046	217.39	4.934	4.945	4.948	4.942	4.968		4.973
.0048	208.33	4.907	4.919	4.921	4.916	4.940		4.953
.0050	200.00	4.882	4.894	4.896	4.891	4.914	4.942	4.930

TABLE 3 (Cont.)

Phase Velocities of Love Waves

Frequency (cps)	Period (sec)	Phase Velocities (km/sec)						
		Mongolia G_3-G_1	Assam G_3-G_1	Alaska-Pasadena G_4-G_2	Kamchatka G_4-G_2	Alaska-Wilkes G_4-G_2	New Guinea G_3-G_1	New Guinea G_4-G_2
.0052	192.31	4.860	4.872	4.874	4.869	4.891	4.918	4.909
.0054	185.19	4.840	4.851	4.853	4.848	4.870	4.897	4.889
.0056	178.57	4.821	4.832	4.834	4.829	4.851	4.877	4.871
.0058	172.41	4.804	4.814	4.816	4.810	4.834	4.859	4.854
.0060	166.67	4.789	4.797	4.800	4.791	4.818	4.842	4.839
.0062	161.29	4.774	4.780	4.785	4.772	4.804	4.826	4.824
.0064	156.25	4.760	4.765	4.771	4.754	4.792	4.812	4.811
.0066	151.52	4.748	4.750	4.758	4.737	4.781	4.801	4.798
.0068	147.06	4.736	4.736	4.746	4.723	4.770	4.787	4.786
.0070	142.86	4.724	4.723	4.734	4.711	4.761	4.775	4.775
.0072	138.89	4.713	4.710	4.724	4.701	4.752	4.765	4.765
.0074	135.14	4.703	4.698	4.714	4.692	4.744	4.755	4.755

TABLE 3 (Cont.)

Phase Velocities of Love Waves

Frequency (cps)	Period (sec)	Phase Velocities (km/sec)						
		Mongolia G_3-G_1	Assam G_3-G_1	Alaska-Pasadena G_4-G_2	Kamchatka G_4-G_2	Alaska-Wilkes G_4-G_2	New Guinea G_3-G_1	New Guinea G_4-G_2
.0076	131.58	4.693	4.686	4.704	4.685	4.736	4.745	4.746
.0078	128.21	4.683	4.676	4.695	4.680	4.729	4.736	4.737
.0080	125.00	4.674	4.666	4.686	4.674	4.722	4.728	4.729
.0084	119.05	4.657	4.648				4.713	4.714
.0088	113.64	4.642	4.633				4.699	4.701
.0092	108.70	4.628	4.620				4.687	4.689
.0096	104.17	4.615	4.609				4.677	4.678
.0100	100.00	4.603	4.598				4.667	4.668
.0104	96.15	4.592	4.589				4.659	4.659
.0108	92.59	4.582	4.580				4.651	4.651
.0112	89.29	4.572	4.572				4.643	4.643
.0116	86.21	4.564	4.565				4.635	4.637

TABLE 3 (Cont.)

Phase Velocities of Love Waves

Frequency (cps)	Period (sec)	Phase Velocities (km/sec)						
		Mongolia G_3-G_1	Assam G_3-G_1	Alaska-Pasadena G_4-G_2	Kamchatka G_4-G_2	Alaska-Wilkes G_4-G_2	New Guinea G_3-G_1	G_4-G_2
.0120	83.33	4.555	4.557				4.622	
.0128	78.12		4.543				4.604	
.0140	71.43						4.585	
.0148	67.57						4.576	
.0156	64.10						4.568	
.0164	60.98						4.560	
.0172	58.14						4.553	
.0180	55.56						4.546	

TABLE 4

Phase Velocities of Rayleigh Waves

Frequency (cps)	Period (sec)	Phase Velocity (km/sec)	
		Mongolia, R_5-R_3	Assam, R_5-R_3
.0028	357.14	5.627	-----
.0029	344.83	5.554	-----
.0030	333.33	5.485	5.509
.0031	322.58	5.415	5.428
.0032	312.50	5.358	5.364
.0033	303.03	5.301	5.312
.0034	294.12	5.229	5.244
.0035	285.71	5.171	5.179
.0036	277.78	5.118	5.121
.0037	270.27	5.060	5.067
.0038	263.16	5.003	5.004
.0039	256.41	4.957	4.957
.0040	250.00	4.913	4.919
.0041	243.90	4.862	4.867
.0042	238.09	4.817	4.818
.0043	232.56	4.781	4.780
.0044	227.27	4.744	4.743
.0045	222.22	4.710	4.713
.0046	217.39	4.682	4.680
.0047	212.77	4.651	4.648

TABLE 4 (Cont.)

Phase Velocities of Rayleigh Waves

Frequency (cps)	Period (sec)	Phase Velocity (km/sec)	
		Mongolia, R_5-R_3	Assam, R_5-R_3
.0048	208.33	4.612	4.613
.0049	204.08	4.588	4.595
.0050	200.00	4.568	4.566
.0052	192.31	4.523	4.524
.0054	185.19	4.479	4.483
.0056	178.57	4.434	4.436
.0058	172.41	4.398	4.403
.0060	166.67	4.370	4.381
.0062	161.29	4.349	4.339
.0064	156.25	4.316	4.319
.0066	151.52	4.288	4.291
.0068	147.06	4.279	4.271
.0070	142.86	4.268	4.253
.0072	138.89	4.255	4.243
.0074	135.14	4.247	4.232
.0076	131.58	4.234	-----
.0078	128.21	4.217	4.227
.0080	125.00	4.203	4.224

TABLE 5
Elastic Parameters of Model CIT-11

Depth km	Thickness km	β km/sec	ρ g/cc
2.5	5.0	1.00	1.00
5.5	1.0	1.00	2.10
8.5	5.0	3.70	2.84
15.5	9.0	4.60	3.53
22.5	5.0	4.61	3.55
27.5	5.0	4.61	3.55
35.0	10.0	4.61	3.55
50.0	20.0	4.56	3.52
70.0	20.0	4.45	3.47
90.0	20.0	4.34	3.42
110.0	20.0	4.34	3.40
130.0	20.0	4.34	3.39
150.0	20.0	4.34	3.39
170.0	20.0	4.50	3.40
190.0	20.0	4.50	3.41
210.0	20.0	4.50	3.46
230.0	20.0	4.50	3.52
250.0	20.0	4.50	3.58
270.0	20.0	4.50	3.62
290.0	20.0	4.50	3.66
310.0	20.0	4.50	3.72
330.0	20.0	4.50	3.76
350.0	20.0	4.50	3.79
380.0	40.0	4.80	3.83
425.0	50.0	5.04	3.89
455.0	10.0	5.40	3.95
530.0	150.0	5.40	4.01
650.0	100.0	5.40	4.21
750.0	100.0	6.20	4.40
850.0	100.0	6.23	4.56
950.0	100.0	6.32	4.63
1100.0	200.0	6.42	4.74
1300.0	200.0	6.55	4.85
1500.0	200.0	6.69	4.96
1700.0	200.0	6.78	5.07
1875.0	150.0	6.85	5.15
2000.0	100.0	6.90	5.20
2100.0	100.0	6.95	5.27
2200.0	100.0	7.00	5.32
2300.0	100.0	7.05	5.37
2400.0	100.0	7.10	5.42
2500.0	100.0	7.14	5.47
2600.0	100.0	7.19	5.52
2700.0	100.0	7.23	5.56
2800.0	100.0	7.28	5.61
2900.0	100.0	7.30	5.66

TABLE 6

Elastic Parameters of Model CIT-12

Depth km	Thickness km	α km/sec	β km/sec	ρ g/cc
1.5	3.0	1.52	1.00	1.00
3.5	1.0	2.10	1.00	2.10
12.5	17.0	6.41	3.65	2.84
25.5	9.0	8.11	4.61	3.53
35.0	10.0	8.14	4.62	3.55
45.0	10.0	8.11	4.61	3.55
60.0	20.0	8.02	4.56	3.52
80.0	20.0	7.90	4.45	3.47
140.0	100.0	7.90	4.40	3.40
220.0	60.0	8.06	4.38	3.46
280.0	60.0	8.06	4.38	3.62
330.0	40.0	8.10	4.40	3.74
360.0	20.0	8.65	4.70	3.79
390.0	40.0	9.01	4.90	3.83
435.0	50.0	9.39	5.10	3.89
530.0	140.0	9.94	5.40	4.01
650.0	100.0	10.49	5.70	4.21
750.0	100.0	11.00	6.20	4.40
850.0	100.0	11.12	6.23	4.56
950.0	100.0	11.35	6.32	4.63
1100.0	200.0	11.60	6.42	4.74
1300.0	200.0	11.93	6.55	4.85
1500.0	200.0	12.20	6.69	4.96
1700.0	200.0	12.40	6.78	5.07
1875.0	150.0	12.60	6.85	5.15
2000.0	100.0	12.70	6.90	5.21
2100.0	100.0	12.85	6.95	5.27
2200.0	100.0	12.97	7.00	5.32
2300.0	100.0	13.09	7.05	5.37
2400.0	100.0	13.21	7.10	5.42
2500.0	100.0	13.33	7.14	5.47
2600.0	100.0	13.46	7.19	5.52
2700.0	100.0	13.53	7.23	5.56
2800.0	100.0	13.61	7.28	5.61
2900.0	100.0	13.65	7.30	5.66

FIGURE CAPTIONS

Figure 1. Great circle paths.

Figure 2. Typical low-pass digital filter response.

Figure 3. Unfiltered (a) and low-pass filtered (b) G_2 and G_4 phases (E-W component) from the Alaska earthquake recorded at Pasadena by the Press-Ewing seismograph system.

Figure 4. Amplitude and phase spectra of the Pasadena recordings of G_2 and G_4 from the Alaska earthquake.

Figure 5. Unfiltered (a) and low-pass filtered (b) G_2 and G_4 phases (N-S component) from the Alaska earthquake recorded at Wilkes by the Press-Ewing seismograph system.

Figure 6. Spectra of G_2 and G_4 from the Alaska earthquake recorded at Wilkes.

Figure 7. G_1 and G_3 traces from the Mongolia earthquake recorded by the Pasadena E-W strain seismograph.

Figure 8. Amplitude and phase spectra of the Mongolia G_1 and G_3.

Figure 9. Unfiltered traces of the Pasadena strain recordings of G_1 and G_3 from the Assam earthquake.

Figure 10. Spectra of G_1 and G_3 from the Assam earthquake.

Figure 11. Filtered traces of the Pasadena N-S strain recordings of G_2 and G_4 from the Kamchatka earthquakes.

FIGURE CAPTIONS (Cont.)

Figure 12. Spectra of G_2 and G_4 from Kamchatka.

Figure 13. Filtered traces of the Pasadena N-S strain recordings of G_1, G_2, G_3, and G_4 traces from the New Guinea earthquake.

Figure 14. Amplitude and phase spectra of G_1, G_2, G_3, and G_4 from New Guinea.

Figure 15. Amplitude and phase spectra of R_3 and R_5 of the Assam earthquake.

Figure 16. Phase and group velocities of Rayleigh waves for the Mongolia-Pasadena and the Assam-Pasadena great circle paths. Group velocities are derived from phase velocities.

Figure 17. Phase and group velocities of Love waves over several great circle paths. The group velocities with circles around the symbol are measured directly from the seismogram. Others derived from the phase velocities.

Figure 18. Shear wave velocity distribution for continental models.

Figure 19. Density distribution for continental and oceanic models.

Figure 20. Comparison of the Mongolia and the Assam-Pasadena Rayleigh wave phase velocities with those of five theoretical models.

FIGURE CAPTIONS (Cont.)

Figure 21. Shear wave velocity distribution for the oceanic models CIT-6 and Case 122 (8099).

Figure 22. Love dispersion curves for the Gutenberg-Bullen A continental and the CIT-11 oceanic models. The experimental data are the same as in Figure 17.

Figure 23. Shear wave velocity distributions for the CIT-11 oceanic and the CIT-12 mixed path models.

Figure 24. Comparison of the CIT-12 mixed path Love wave dispersion curves with the Mongolia, Assam, Kamchatka, and Alaska-Pasadena data. The additional ultra-long period data are from torsional oscillation observations and from Brune, Benioff, and Ewing (1961).

Figure 25. Rayleigh wave dispersion curve for the CIT-12 mixed path model and the observed data over the Mongolia and the Assam-Pasadena paths. The experimental points shown as triangles are for the Assam-Pasadena path measured by Nafe and Brune (1960) and corrected by Brune, Nafe, and Alsop (1961).

Figure 26. Compressional and shear velocity profiles of CIT-12.

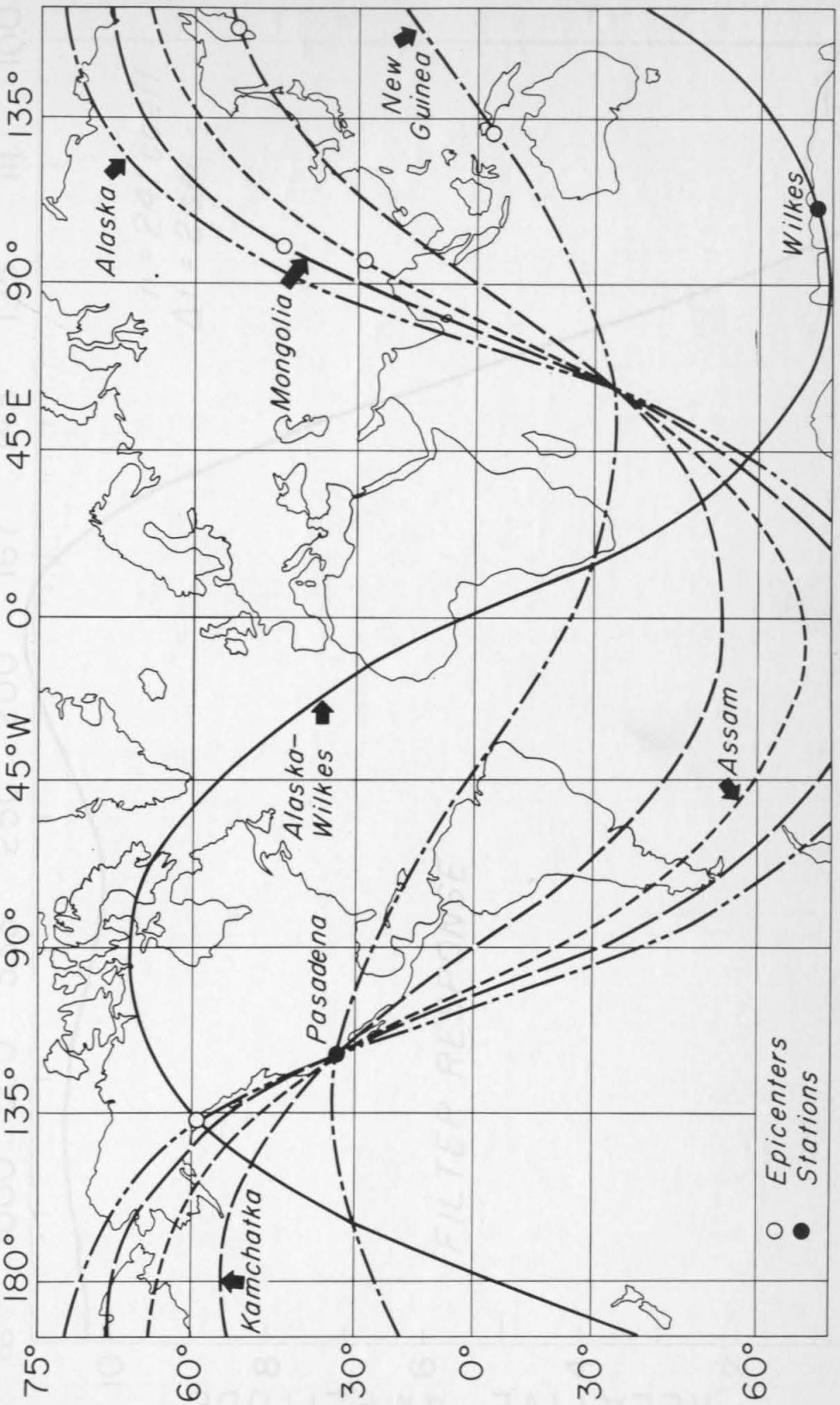
75°
60°
30°
0°
30°
60°
180°
135°
90°
45°W
0°
45°E
90°
135°
Alaska
Mongolia
New Guinea
Wilkes
Alaska-Wilkes
Pasadena
Assam
Kamchatka
Epicenters
Stations

Fig. 1

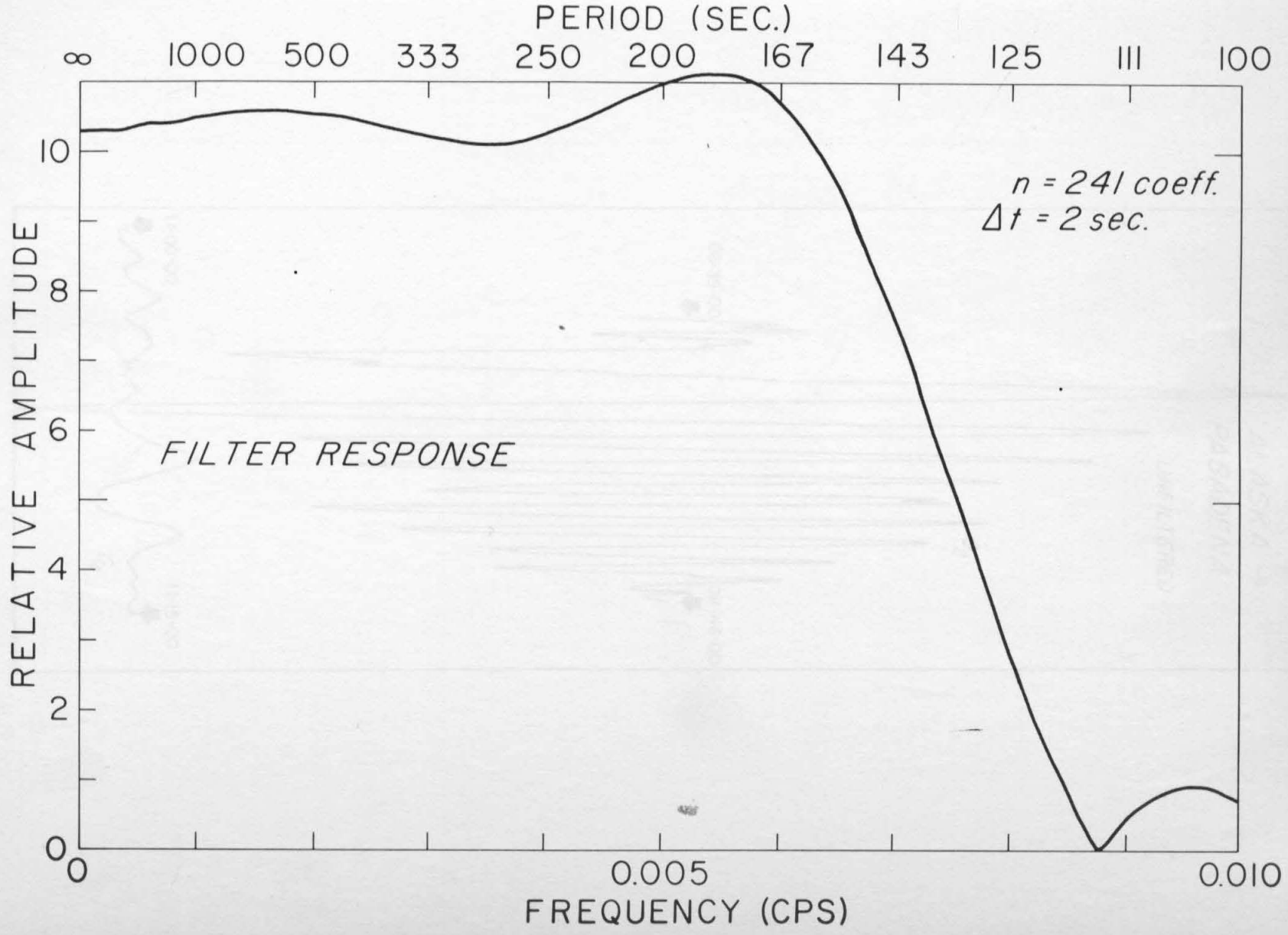
PERIOD (SEC.)
∞
1000
500
333
250
200
167
143
125
111
100
RELATIVE AMPLITUDE
0
2
4
6
8
10
n = 241 coeff.
Δt = 2 sec.
FILTER RESPONSE
0
0.005
0.010
FREQUENCY (CPS)

Fig. 2

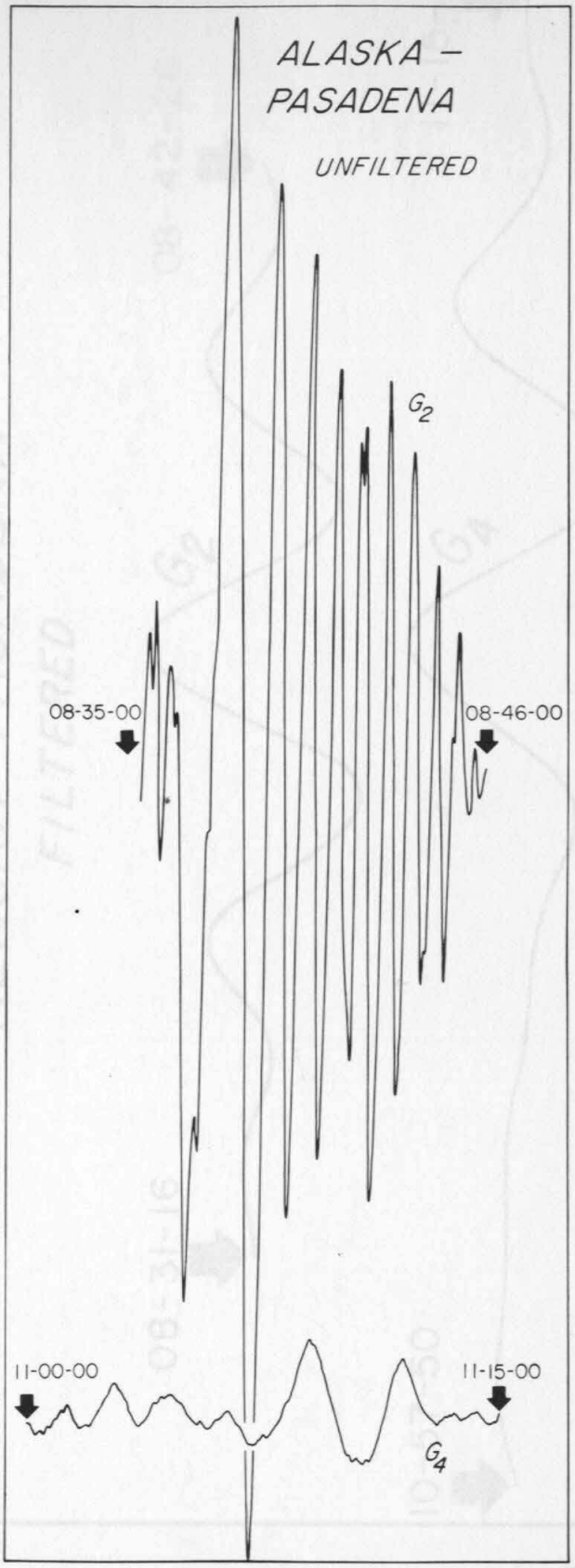
ALASKA –
PASADENA
UNFILTERED
G_2
08-35-00
08-46-00
11-00-00
11-15-00
G_4

Fig. 3(a)

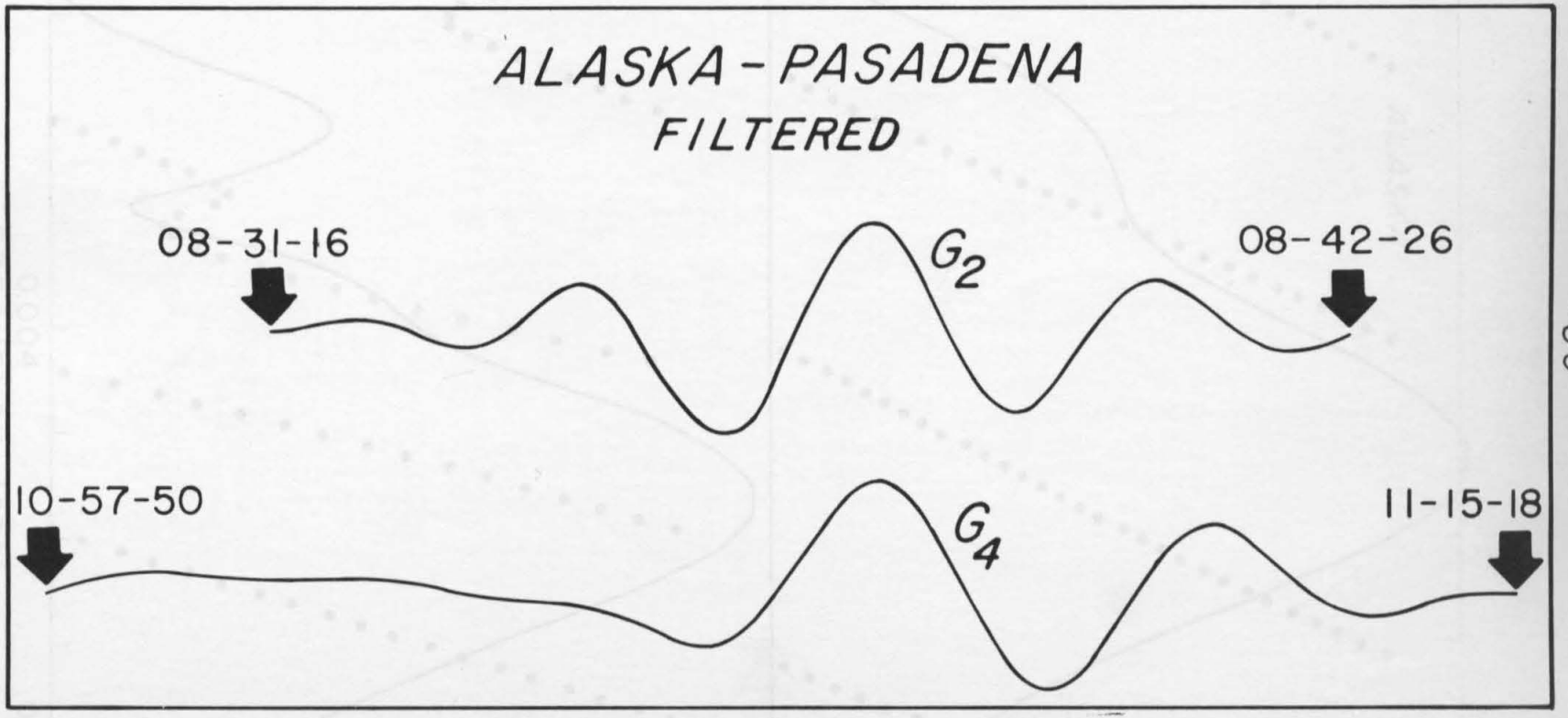
ALASKA - PASADENA
FILTERED
08-31-16
G_2
08-42-26
10-57-50
G_4
11-15-18

Fig. 3(b)

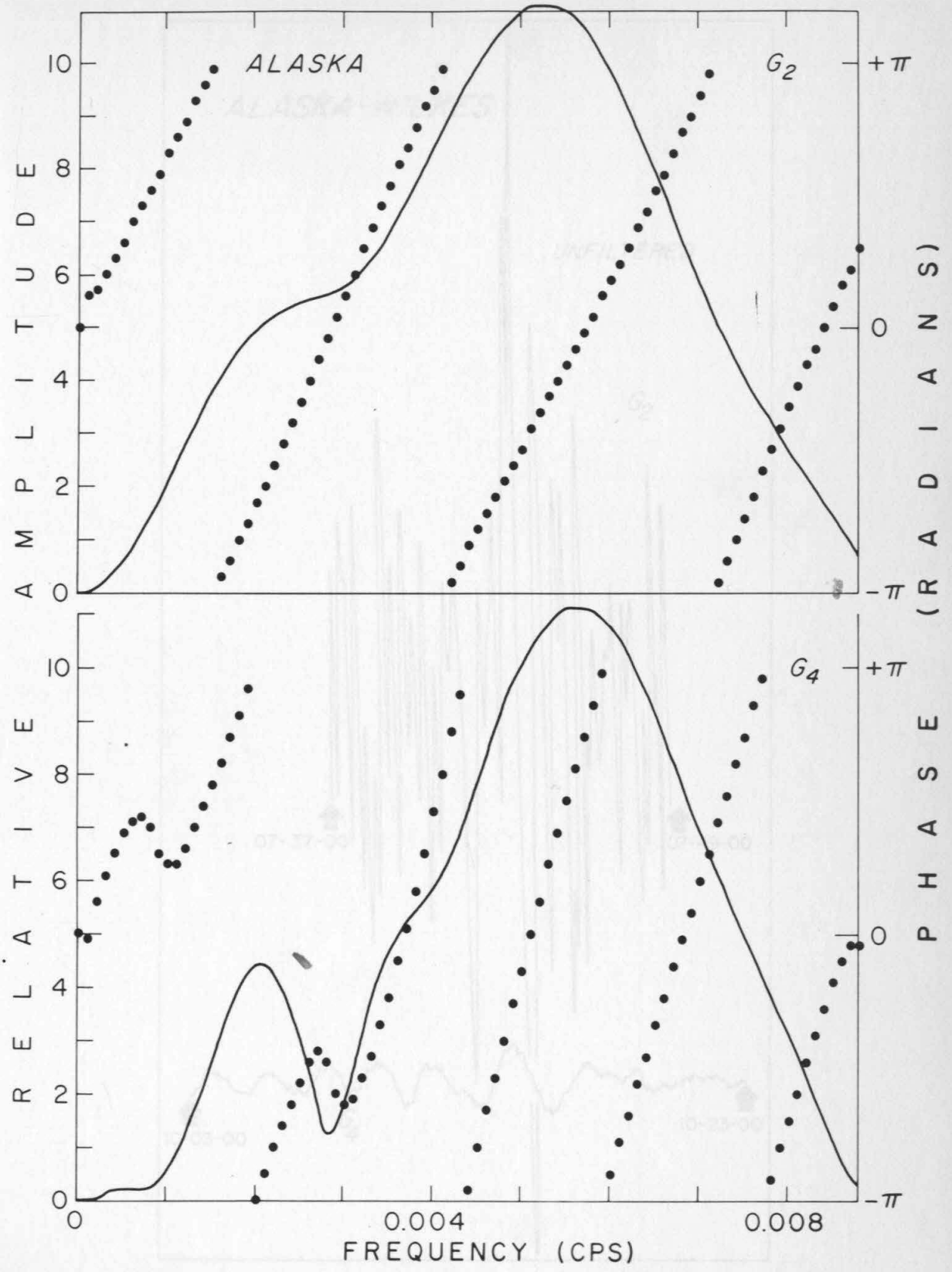
ALASKA
G_2
G_4
RELATIVE AMPLITUDE
PHASE (RADIANS)
+π
0
-π
0
2
4
6
8
10
0.004
0.008
FREQUENCY (CPS)

Fig. 4

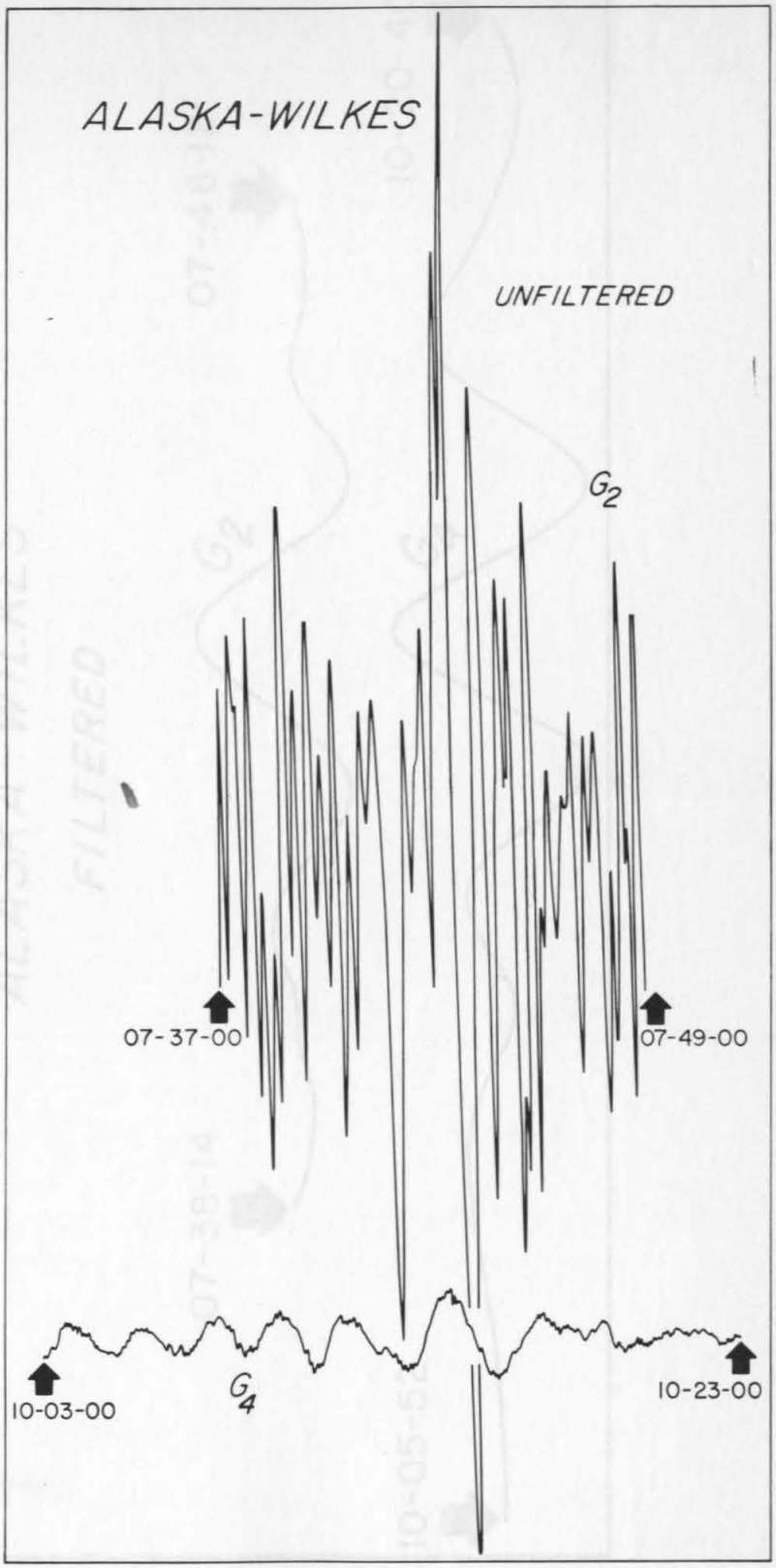
ALASKA-WILKES
UNFILTERED
G_2
07-37-00
07-49-00
G_4
10-03-00
10-23-00

Fig. 5(a)

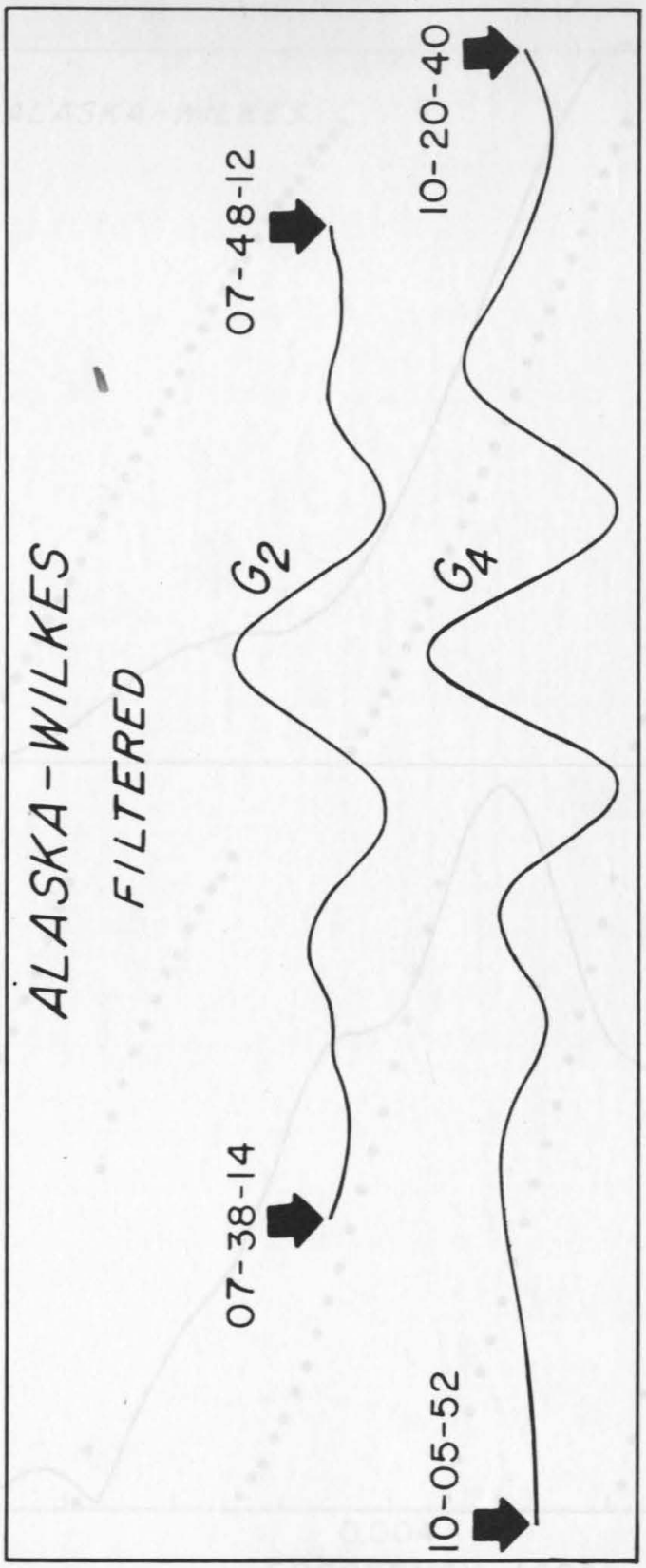

Fig. 5(b)

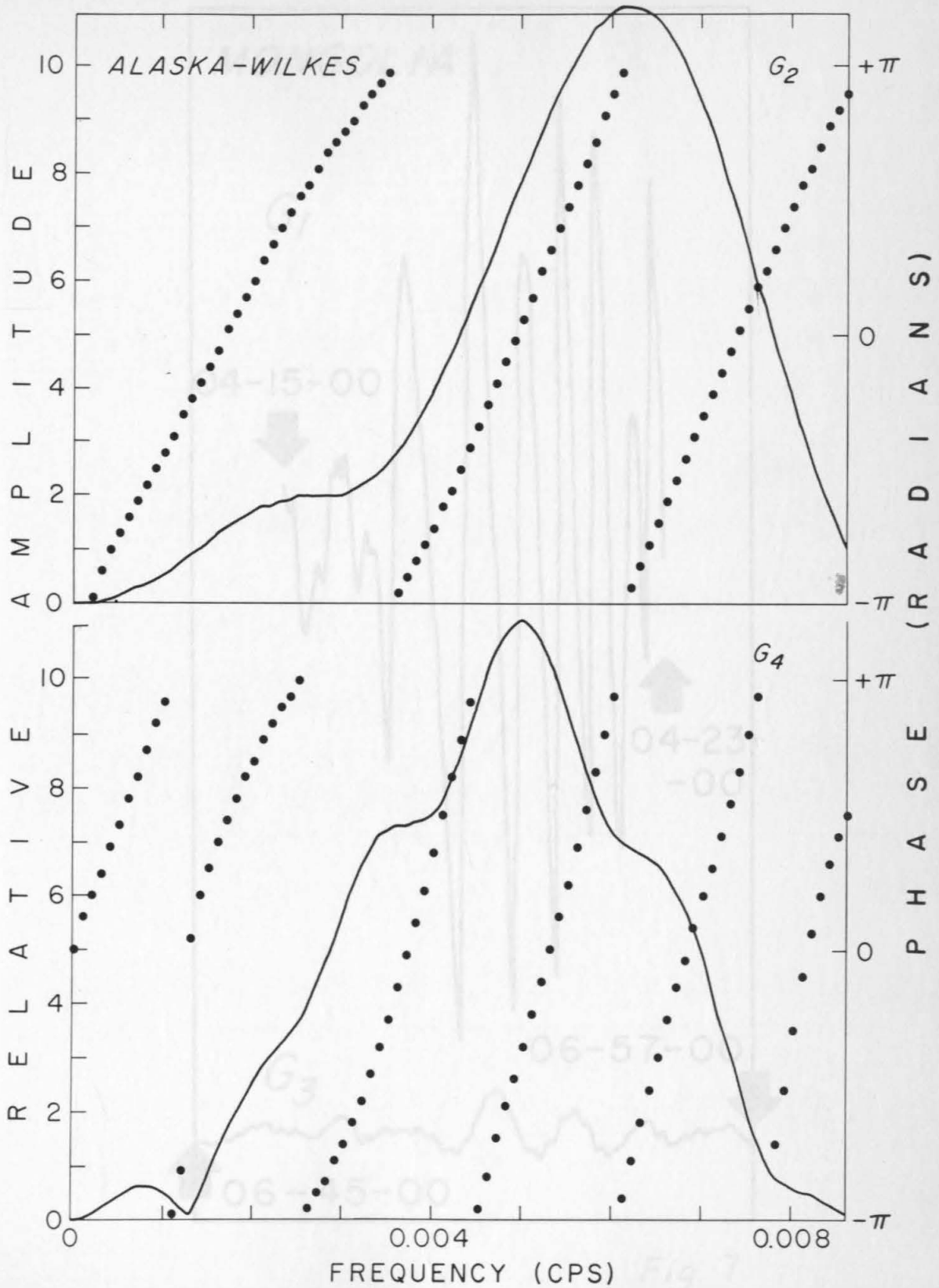
ALASKA-WILKES
G_2
G_4
RELATIVE AMPLITUDE
PHASE (RADIANS)
0
2
4
6
8
10
$+\pi$
0
$-\pi$
0.004
0.008
FREQUENCY (CPS)

Fig. 6

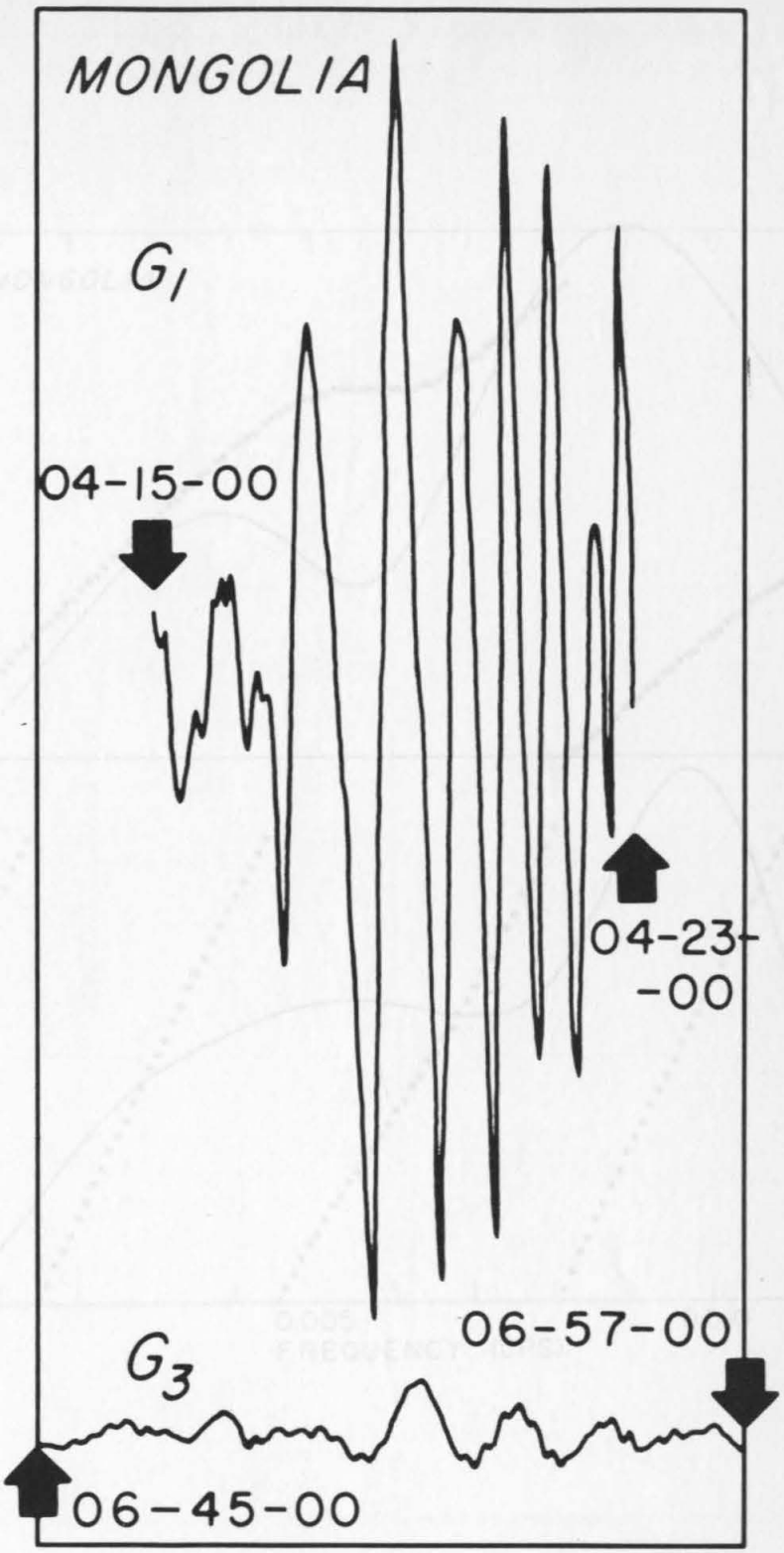

Fig. 7

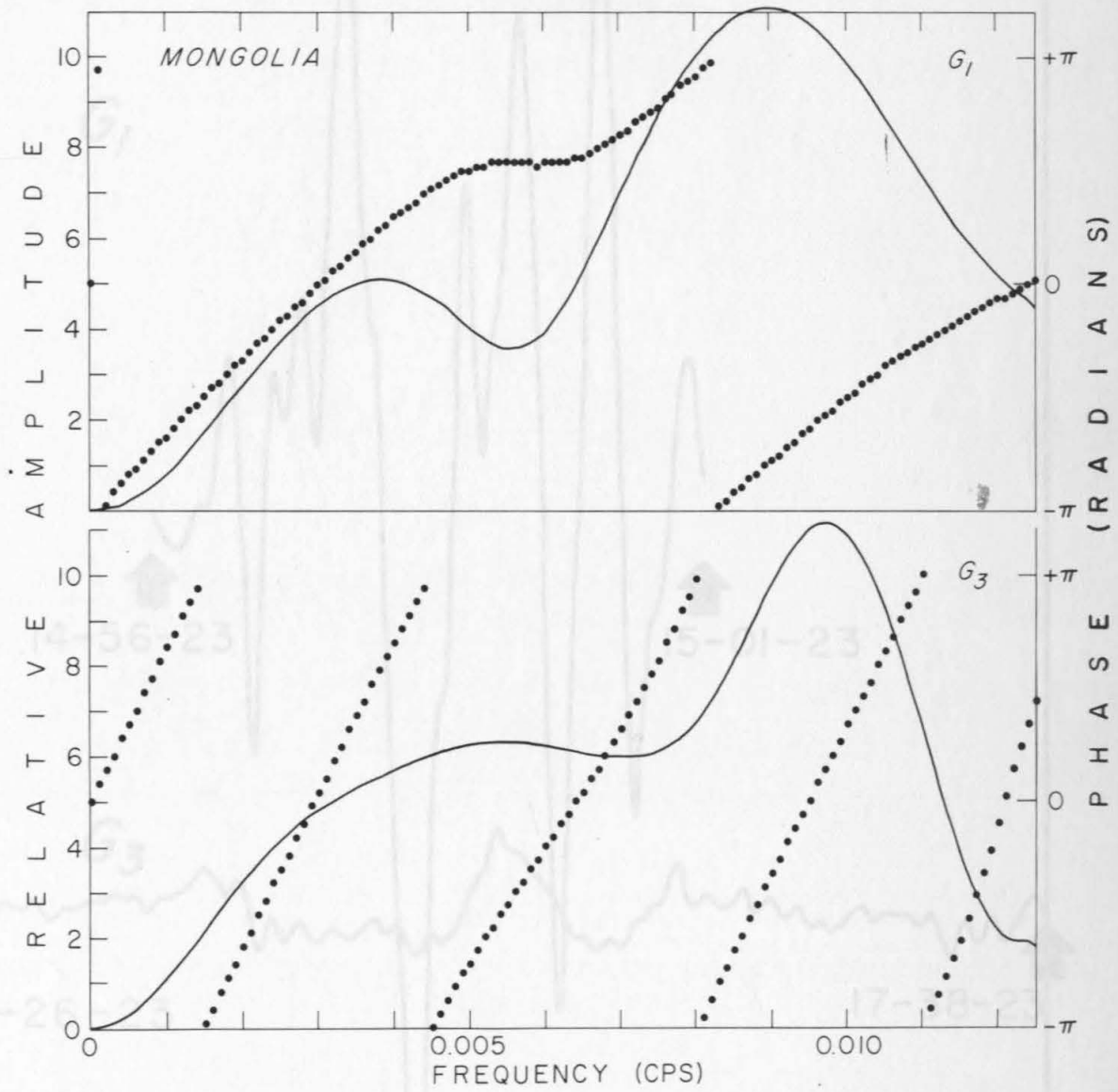
MONGOLIA
G_1
G_3
RELATIVE AMPLITUDE
PHASE (RADIANS)
10
8
6
4
2
0
+π
0
-π
0.005
0.010
FREQUENCY (CPS)

Fig. 8

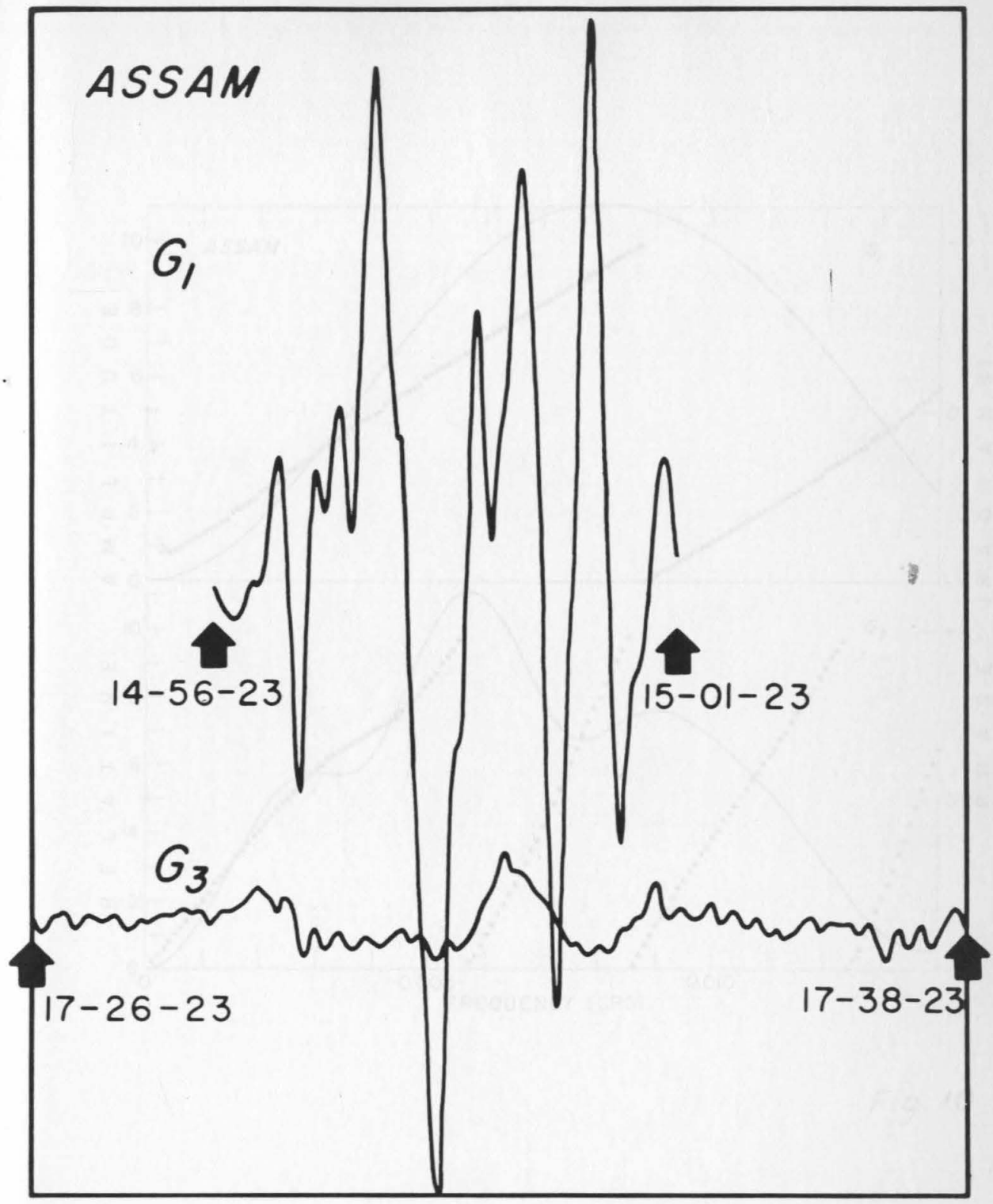

Fig. 9

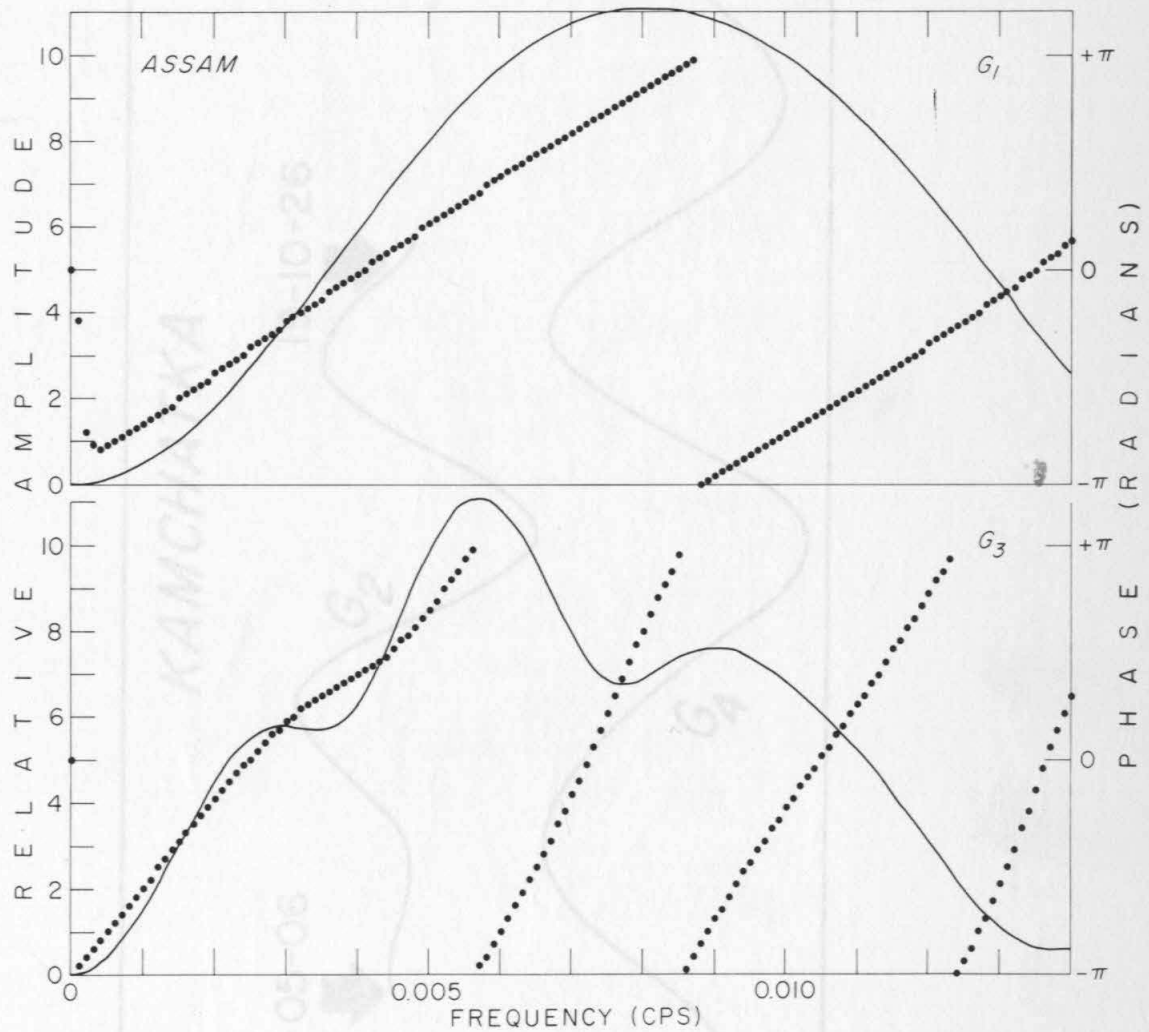
ASSAM
G_1
G_3
RELATIVE AMPLITUDE
PHASE (RADIANS)
FREQUENCY (CPS)
0
2
4
6
8
10
0.005
0.010
$+\pi$
0
$-\pi$

Fig. 10

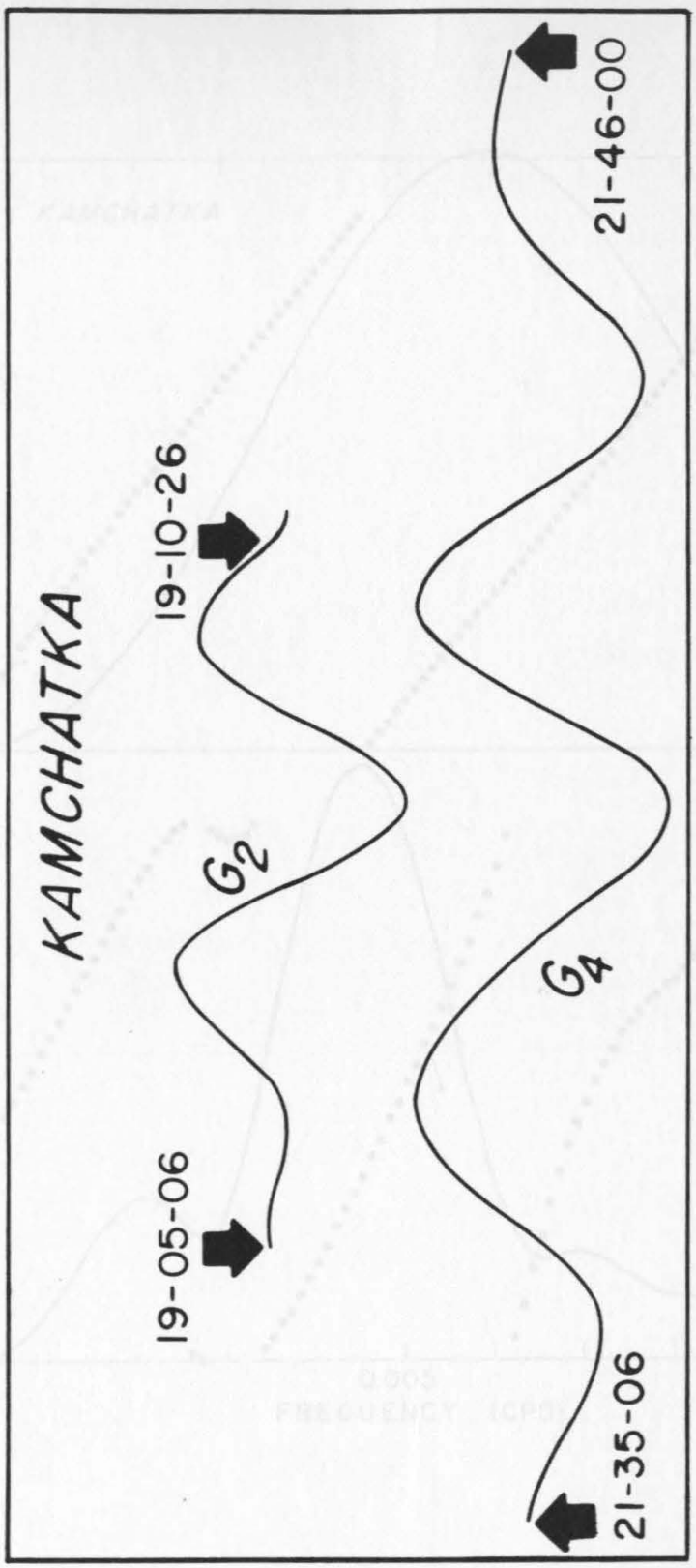

Fig. 11

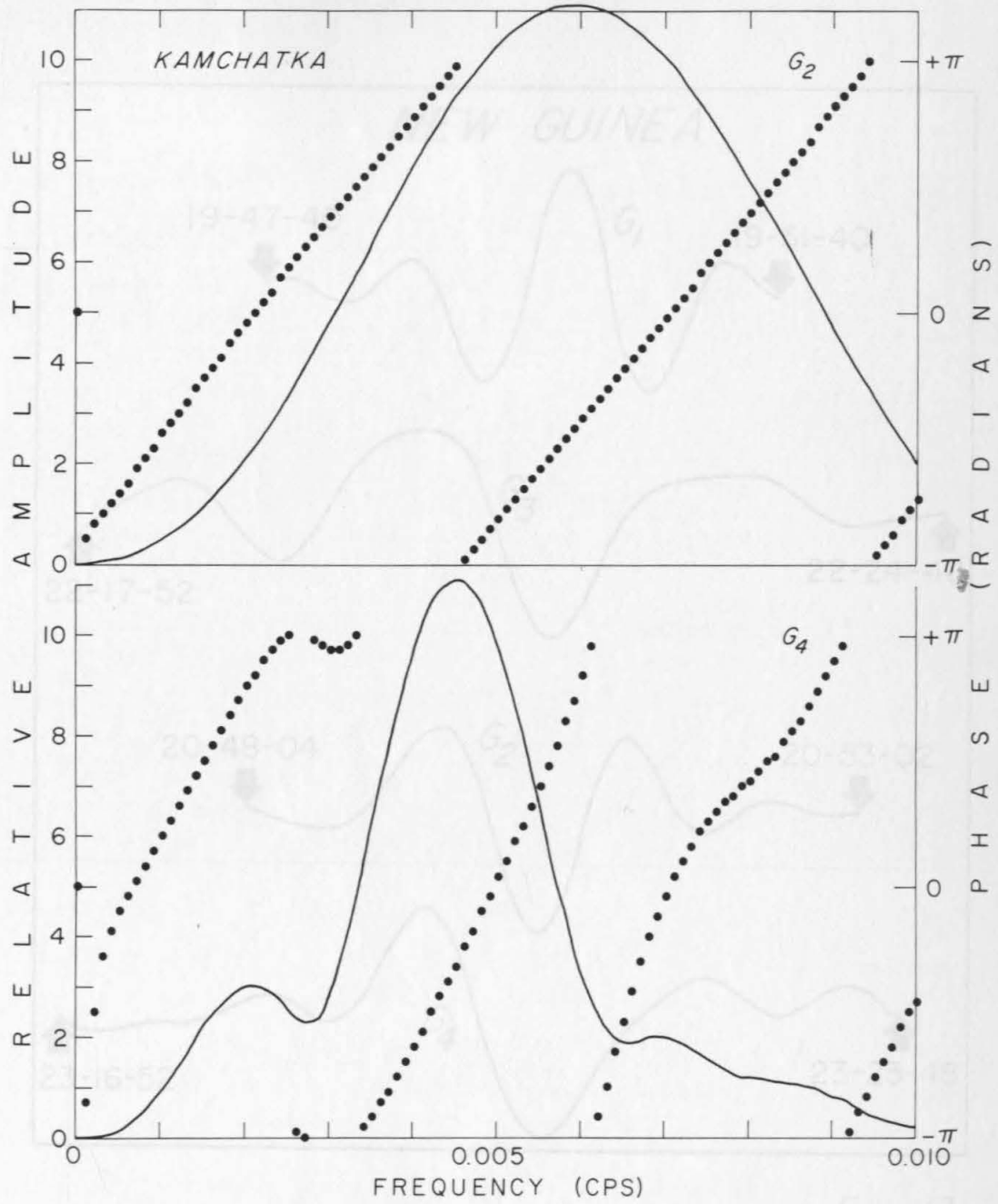
KAMCHATKA
G_2
G_4
RELATIVE AMPLITUDE
PHASE (RADIANS)
+π
0
-π
0
2
4
6
8
10
0
0.005
0.010
FREQUENCY (CPS)

Fig. 12

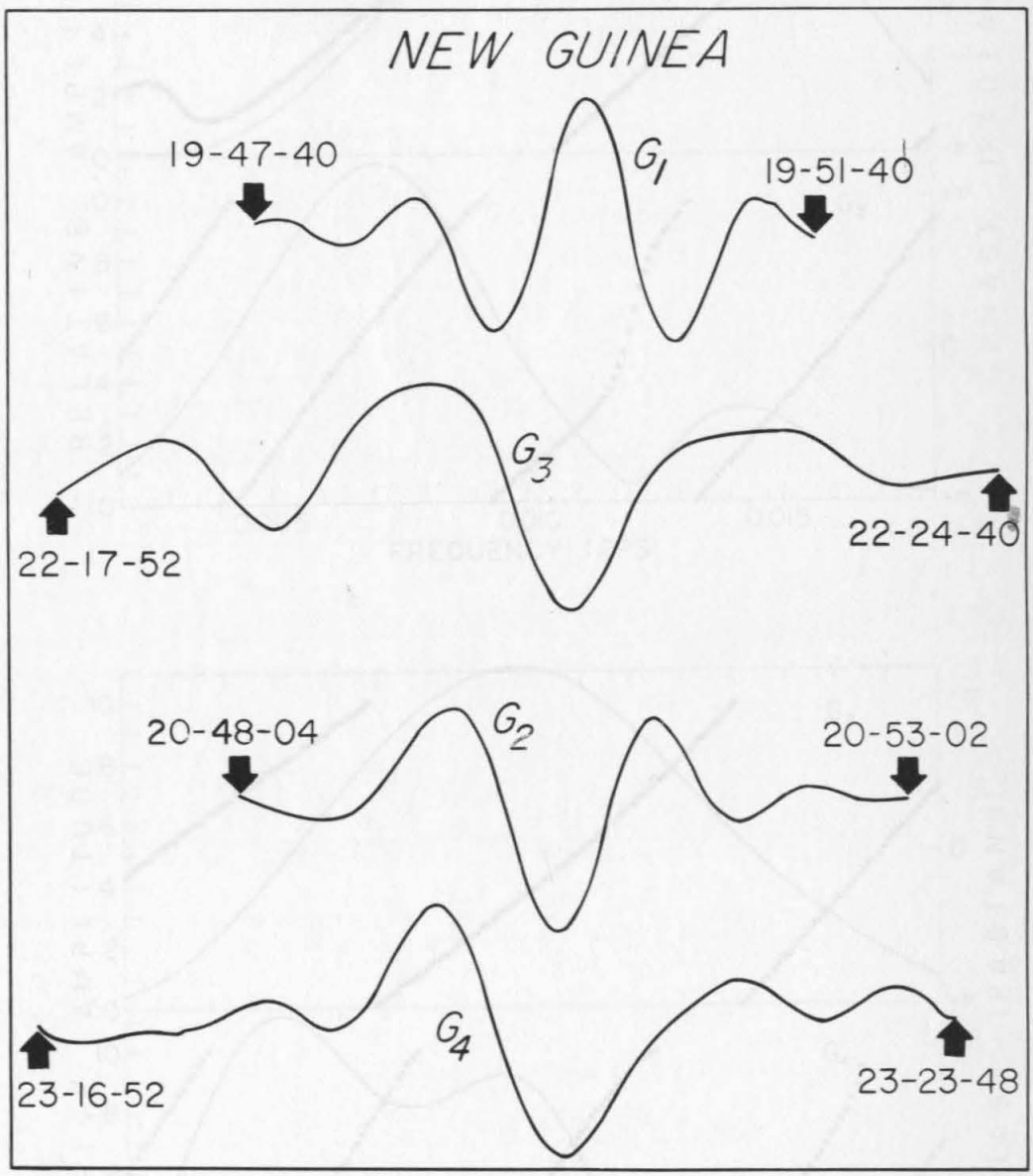
NEW GUINEA
19-47-40
G1
19-51-40
G3
22-17-52
22-24-40
20-48-04
G2
20-53-02
G4
23-16-52
23-23-48

Fig. 13

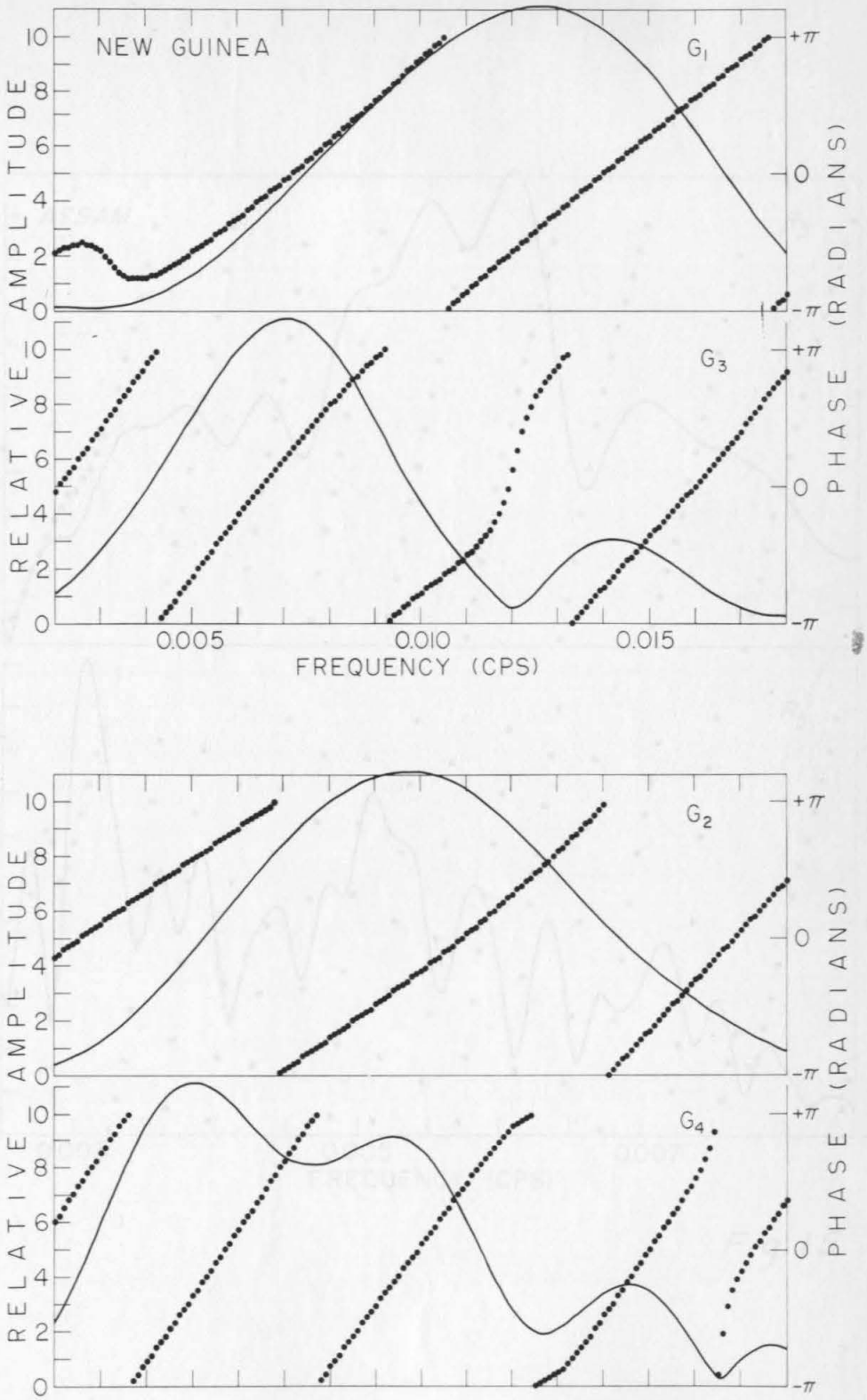
NEW GUINEA
G1
G3
G2
G4
RELATIVE AMPLITUDE
PHASE (RADIANS)
+π
0
-π
0.005
0.010
0.015
FREQUENCY (CPS)

Fig. 14

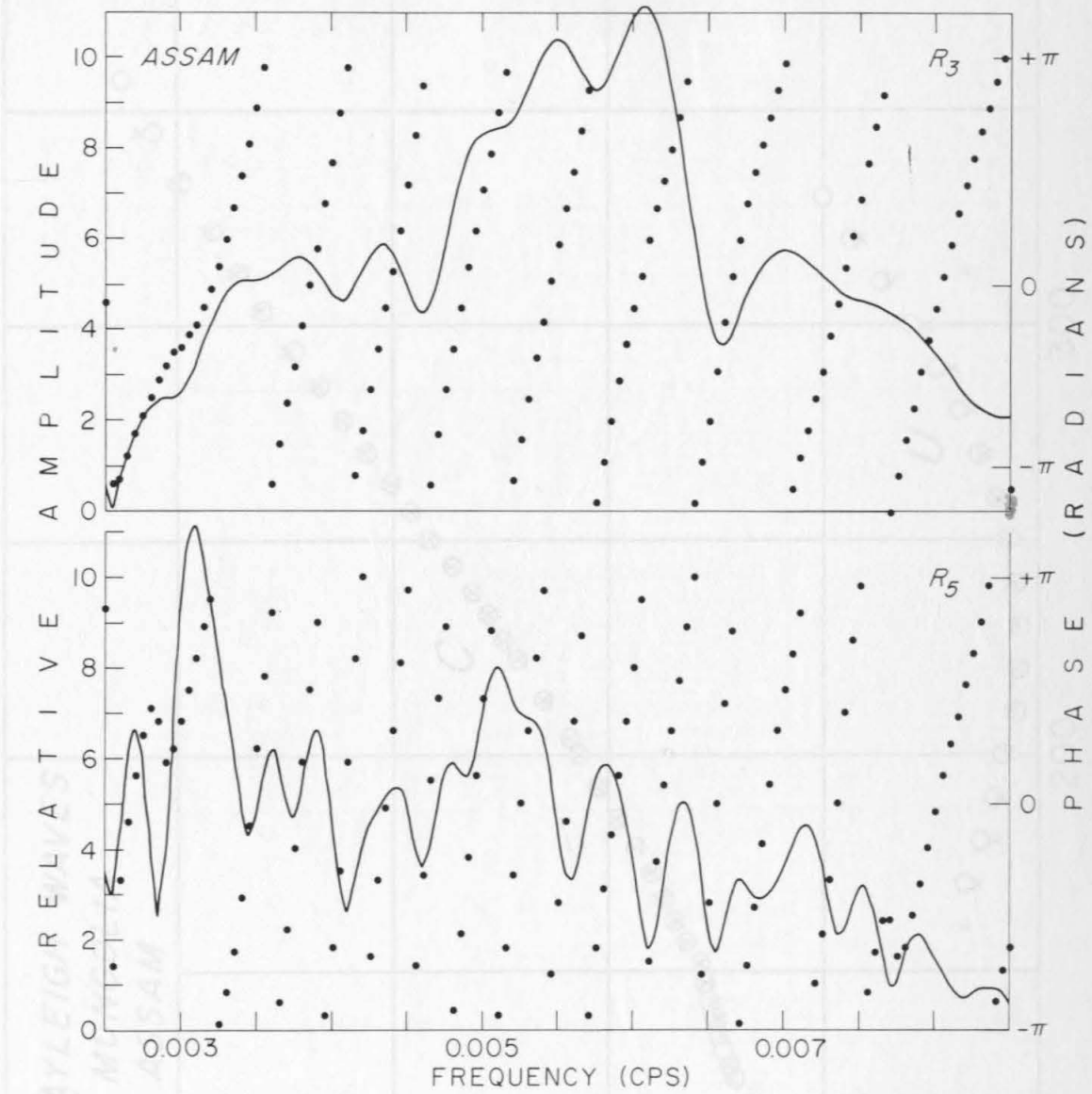
ASSAM
R_3
R_5
RELATIVE AMPLITUDE
PHASE (RADIANS)
+π
0
-π
0
2
4
6
8
10
0.003
0.005
0.007
FREQUENCY (CPS)

Fig. 15

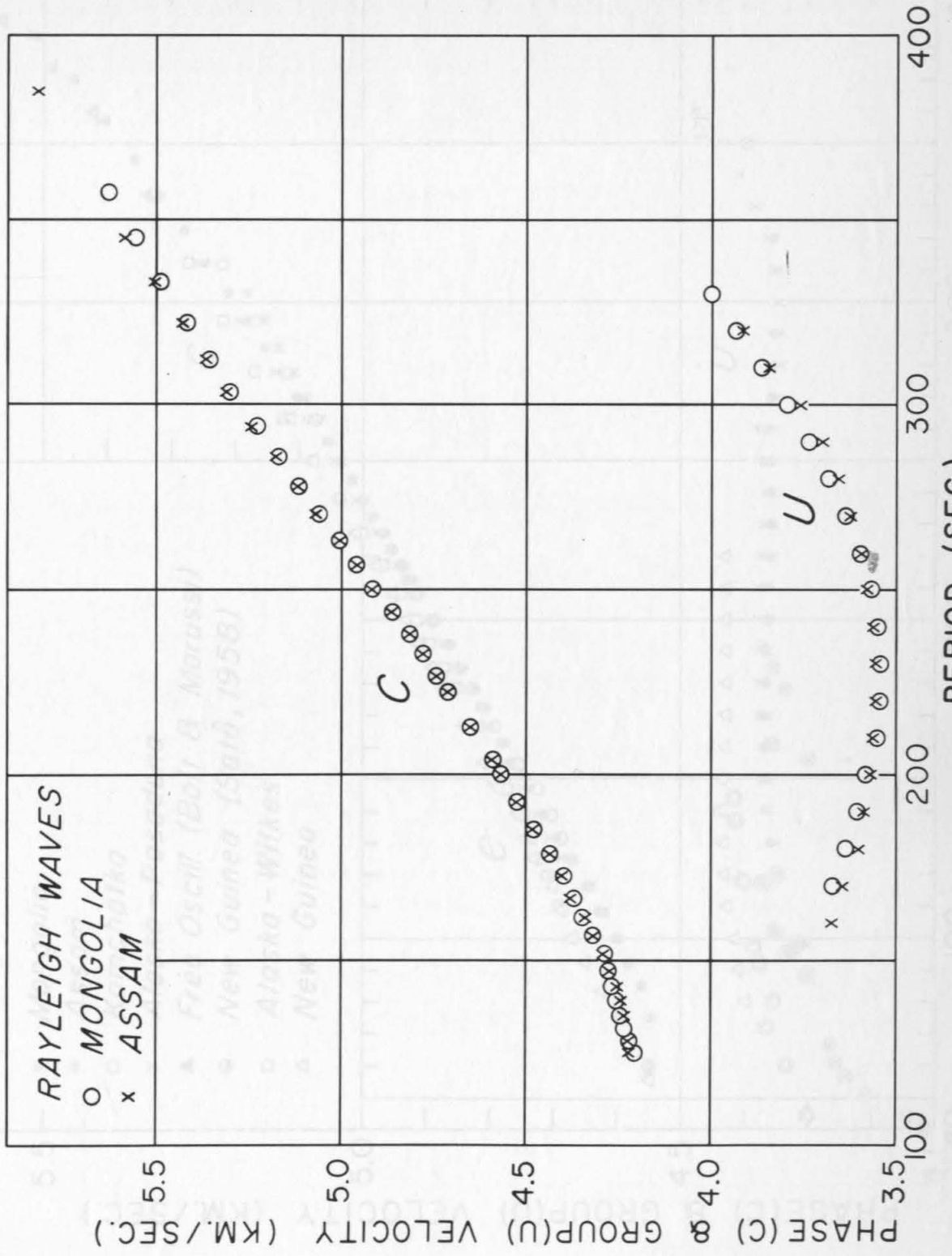
RAYLEIGH WAVES
O MONGOLIA
x ASSAM
C
U
PHASE (C) & GROUP (U) VELOCITY (KM./SEC.)
PERIOD (SEC.)
5.5
5.0
4.5
4.0
3.5
100
200
300
400

Fig. 16

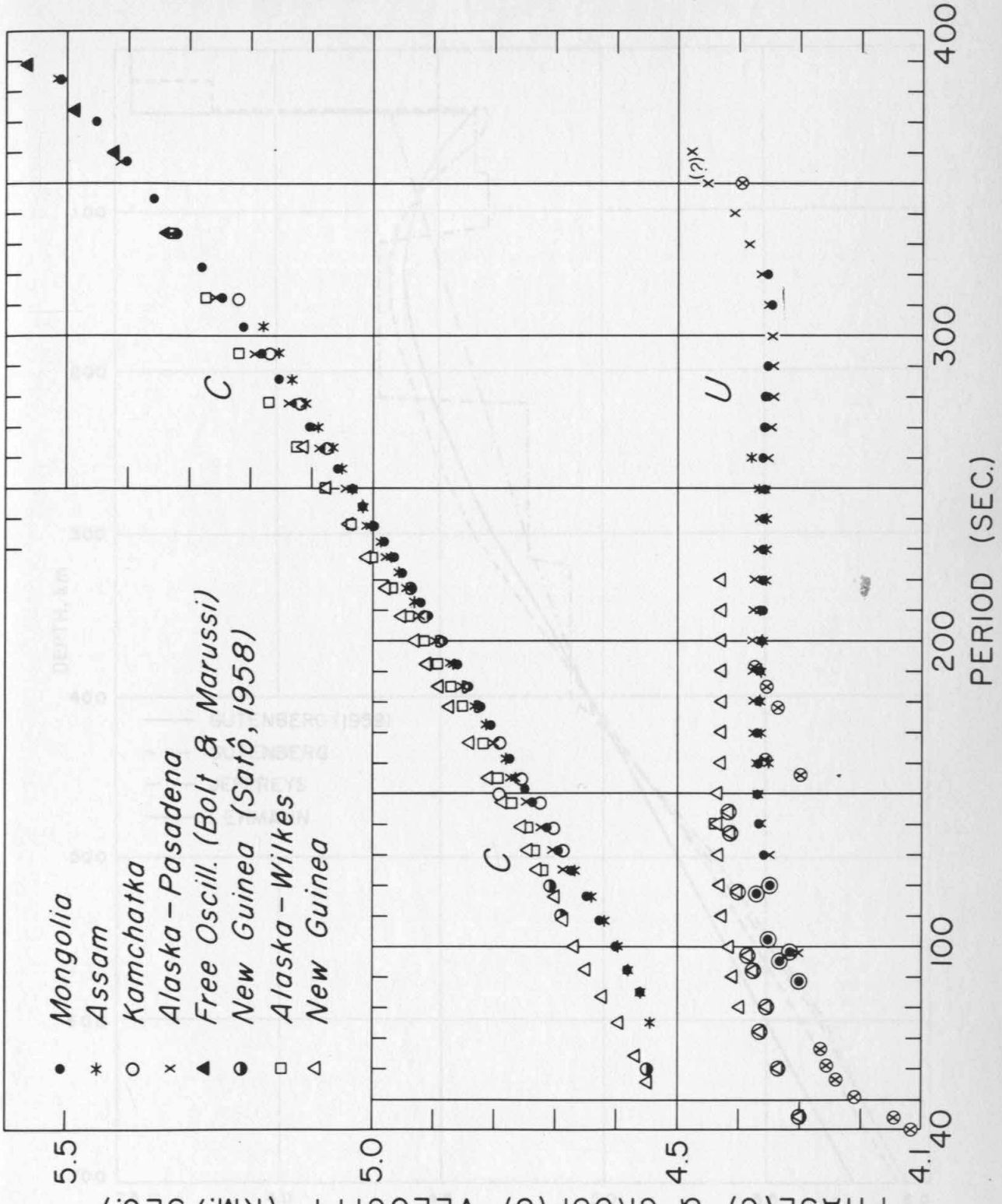
Mongolia
Assam
Kamchatka
Alaska–Pasadena
Free Oscill. (Bolt & Marussi)
New Guinea (Satô, 1958)
Alaska–Wilkes
New Guinea
C
C
U
x(?)x
5.5
5.0
4.5
4.1
40
100
200
300
400
PERIOD (SEC.)
PHASE(C) & GROUP(U) VELOCITY (KM./SEC.)

Fig. 17

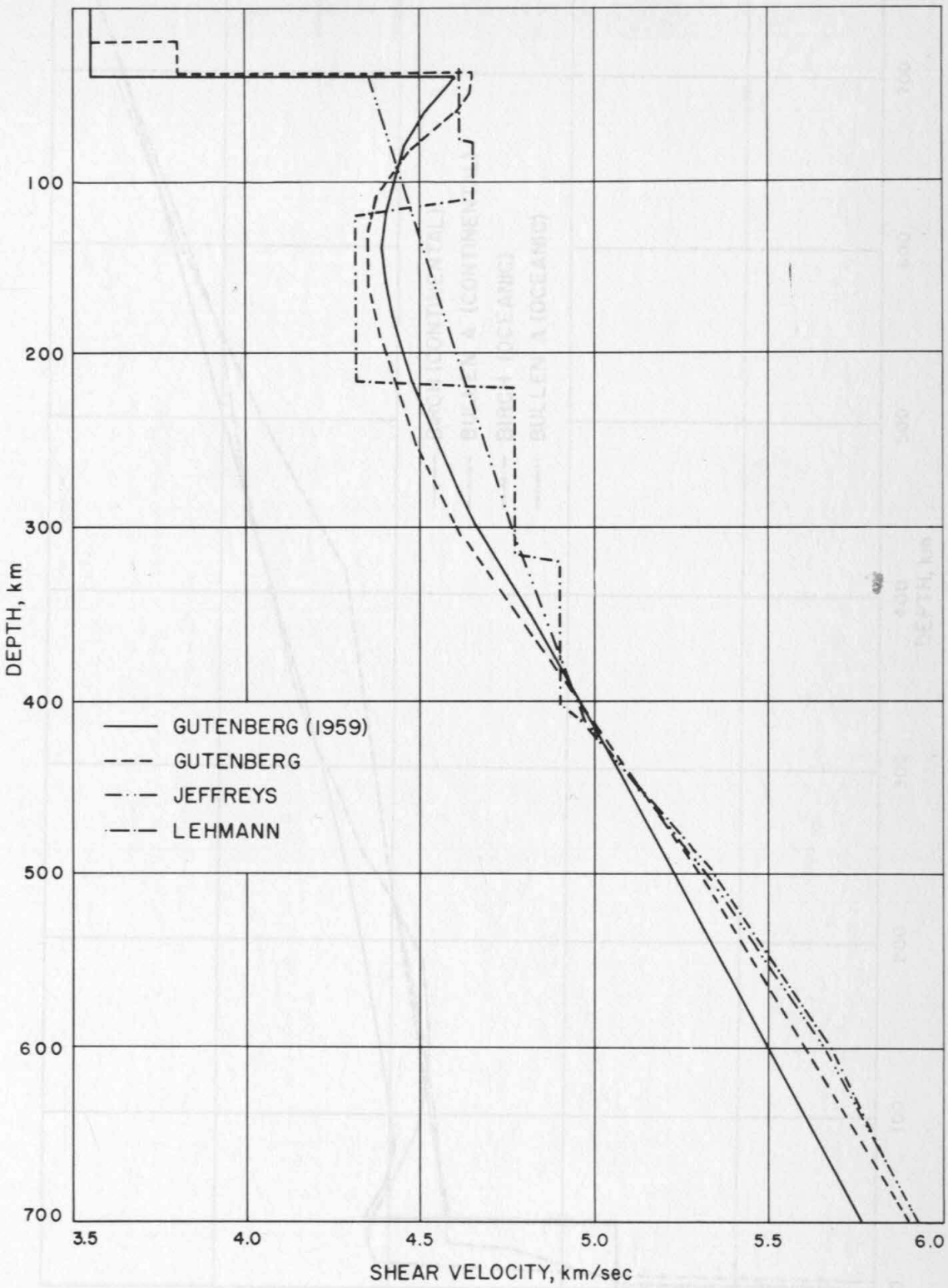
100
200
300
400
500
600
700
DEPTH, km
GUTENBERG (1959)
GUTENBERG
JEFFREYS
LEHMANN
3.5
4.0
4.5
5.0
5.5
6.0
SHEAR VELOCITY, km/sec

Fig. 18

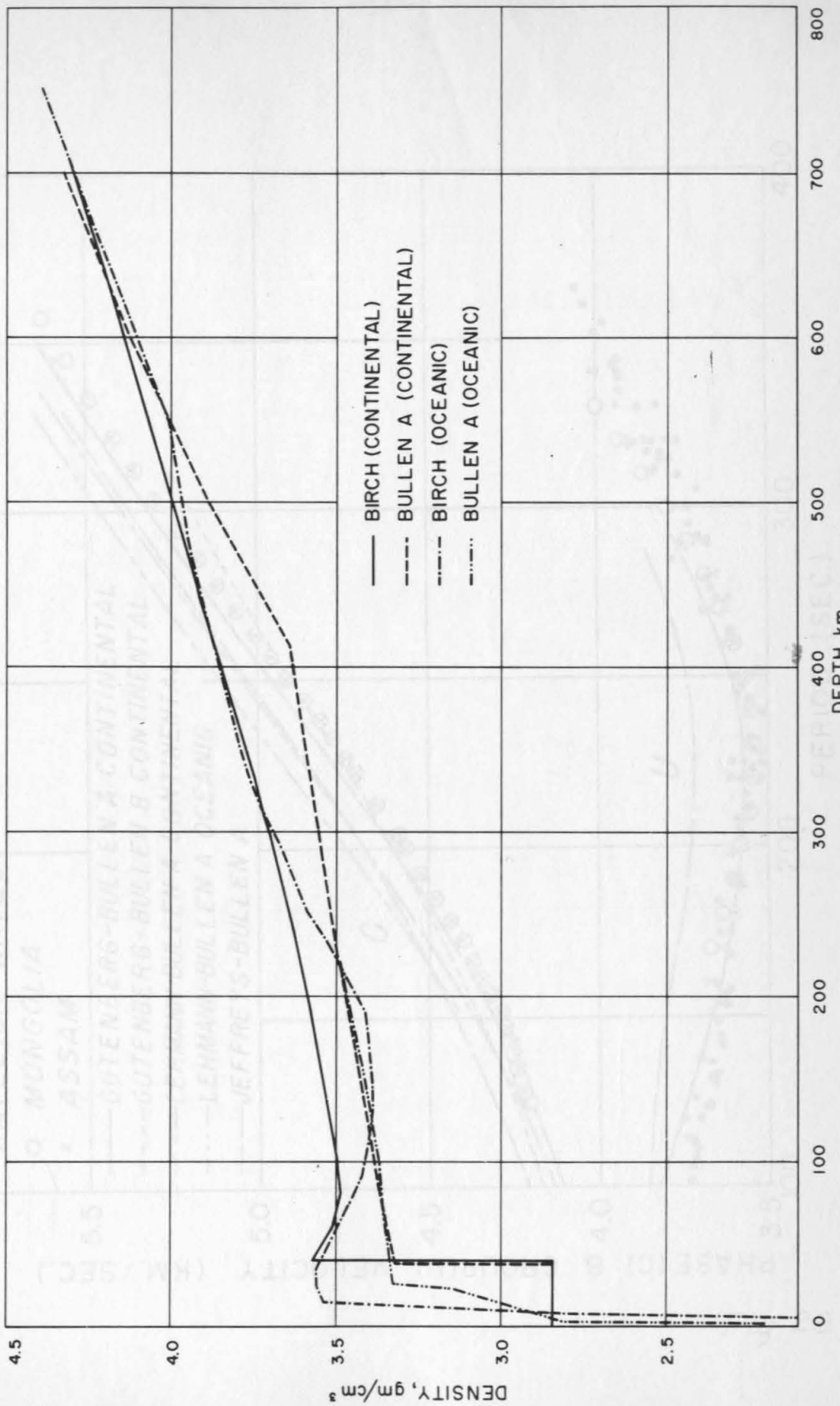
BIRCH (CONTINENTAL)
BULLEN A (CONTINENTAL)
BIRCH (OCEANIC)
BULLEN A (OCEANIC)
DENSITY, gm/cm³
4.5
4.0
3.5
3.0
2.5
0
100
200
300
400
500
600
700
800
DEPTH, km

Fig. 19

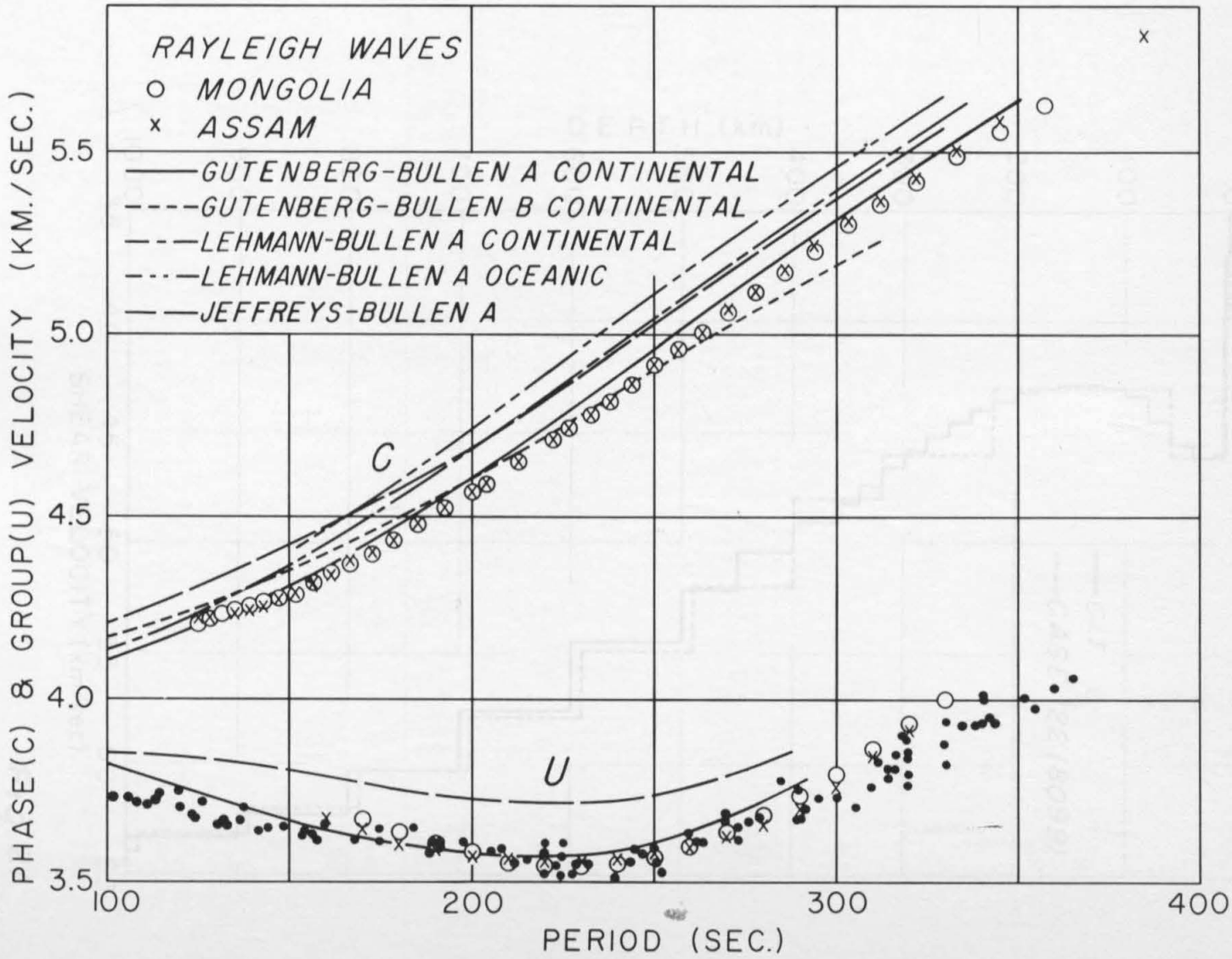
RAYLEIGH WAVES
MONGOLIA
ASSAM
GUTENBERG-BULLEN A CONTINENTAL
GUTENBERG-BULLEN B CONTINENTAL
LEHMANN-BULLEN A CONTINENTAL
LEHMANN-BULLEN A OCEANIC
JEFFREYS-BULLEN A
C
U
PHASE (C) & GROUP (U) VELOCITY (KM./SEC.)
PERIOD (SEC.)
5.5
5.0
4.5
4.0
3.5
100
200
300
400

Fig. 20

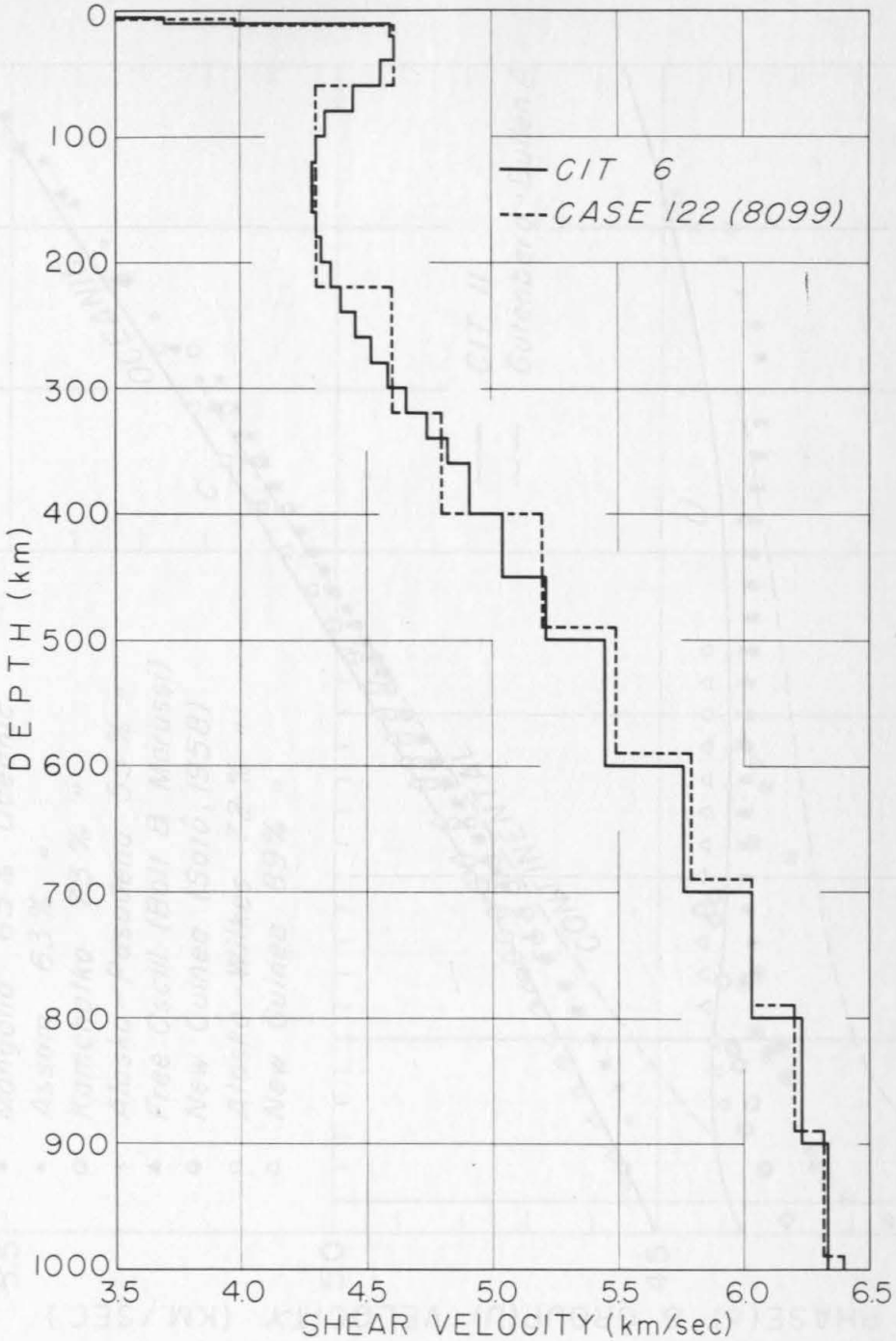
0
100
200
300
400
500
600
700
800
900
1000
DEPTH (km)
3.5
4.0
4.5
5.0
5.5
6.0
6.5
SHEAR VELOCITY (km/sec)
CIT 6
CASE 122 (8099)

Fig. 21

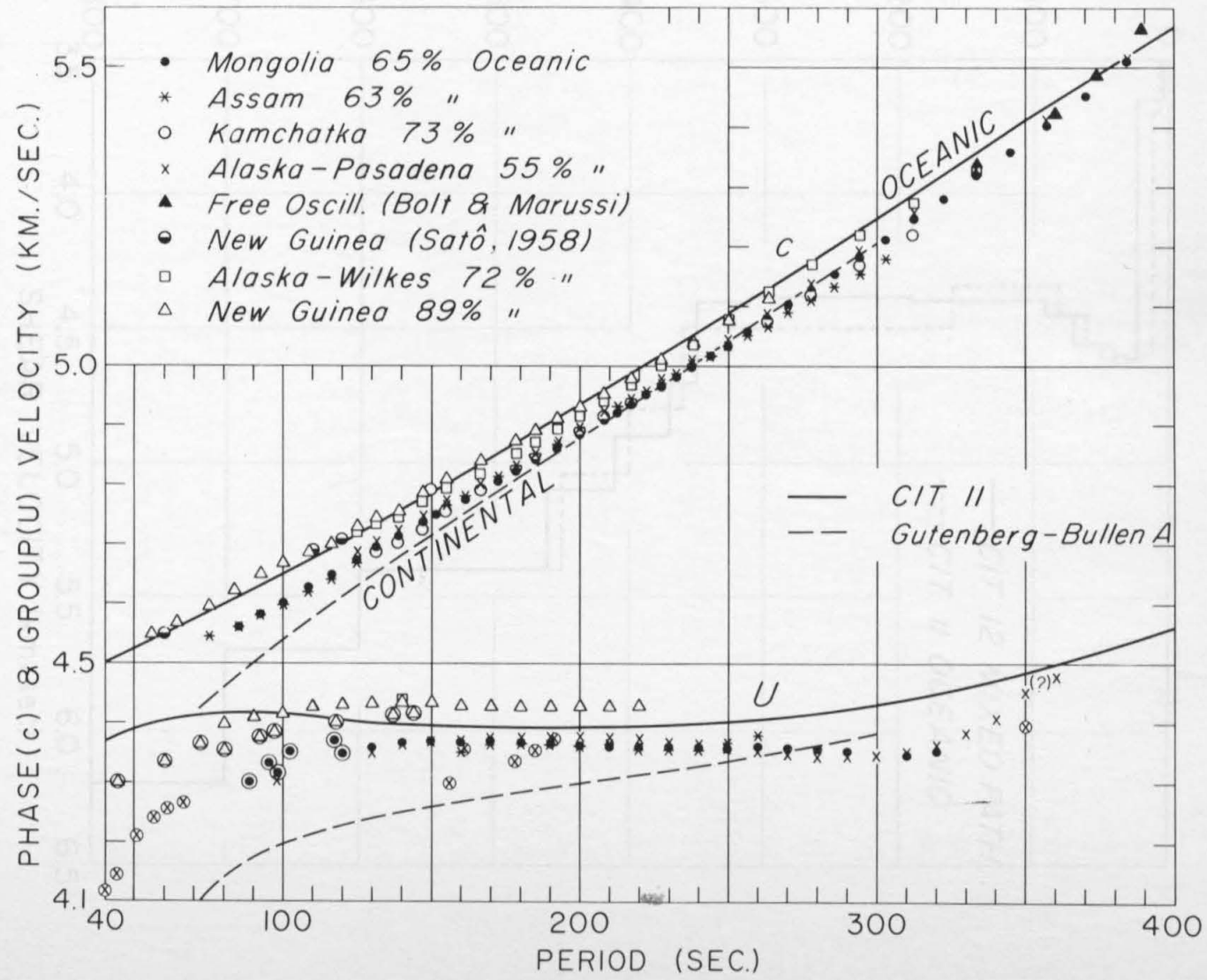
Mongolia 65% Oceanic
Assam 63% "
Kamchatka 73% "
Alaska-Pasadena 55% "
Free Oscill. (Bolt & Marussi)
New Guinea (Satô, 1958)
Alaska-Wilkes 72% "
New Guinea 89% "
OCEANIC
C
CONTINENTAL
U
CIT II
Gutenberg-Bullen A
(?)
PHASE(c) & GROUP(U) VELOCITY (KM./SEC.)
PERIOD (SEC.)
5.5
5.0
4.5
4.1
40
100
200
300
400

Fig. 22

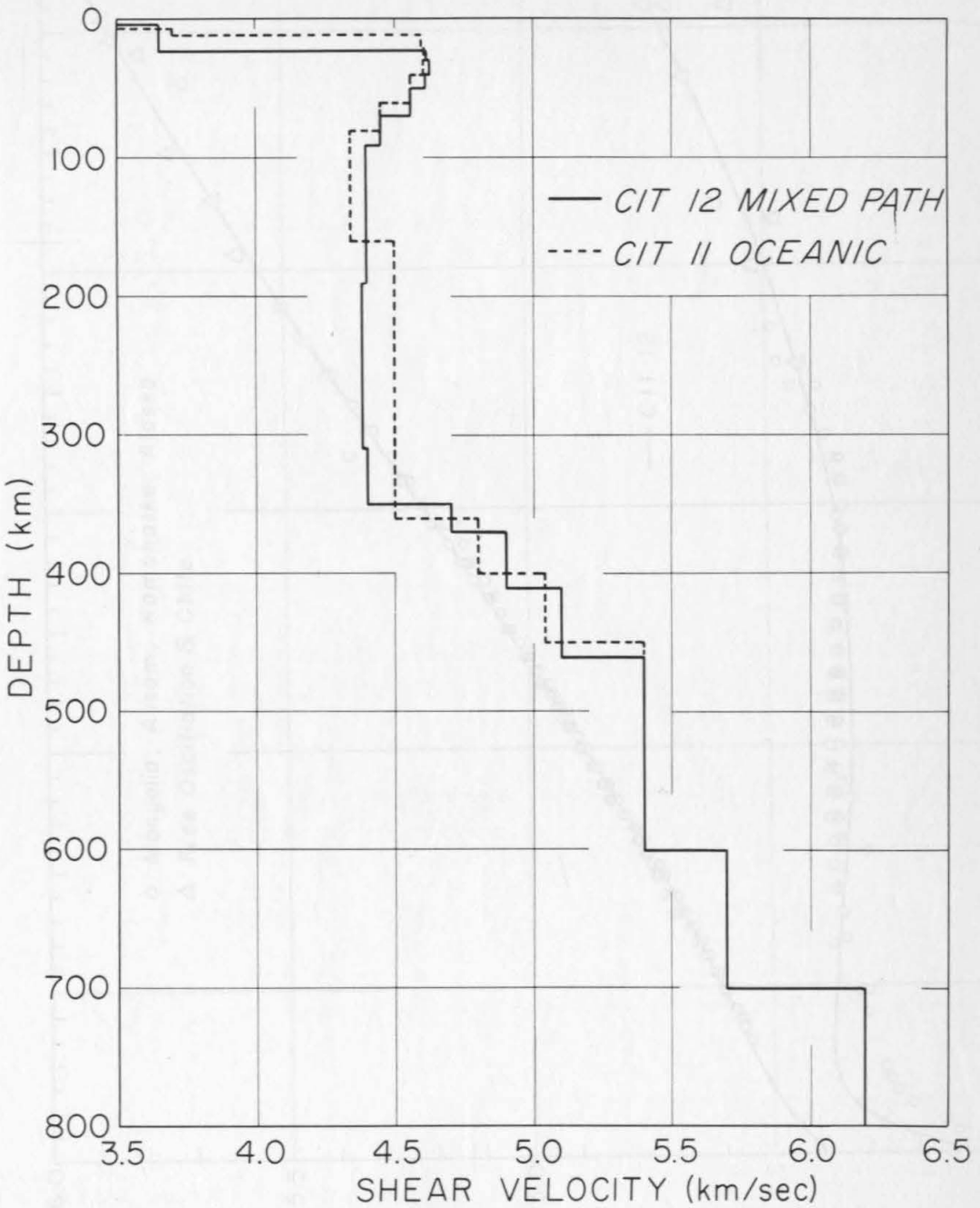
0
100
200
300
400
500
600
700
800
DEPTH (km)
3.5
4.0
4.5
5.0
5.5
6.0
6.5
SHEAR VELOCITY (km/sec)
CIT 12 MIXED PATH
CIT 11 OCEANIC

Fig. 23

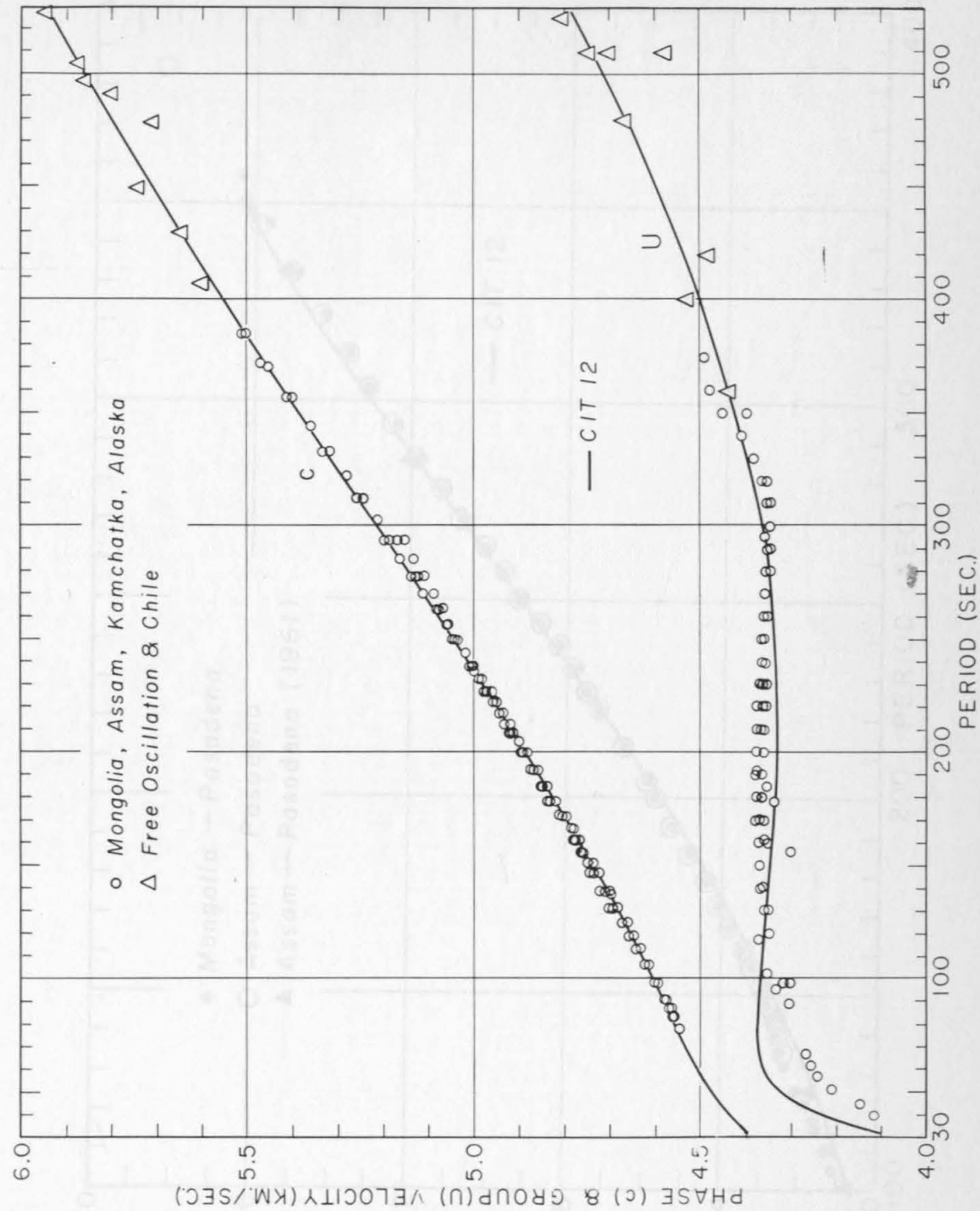
o Mongolia, Assam, Kamchatka, Alaska
Δ Free Oscillation & Chile
C
U
CIT 12
PHASE (c) & GROUP(U) VELOCITY (KM./SEC.)
PERIOD (SEC.)
6.0
5.5
5.0
4.5
4.0
30
100
200
300
400
500

Fig. 24

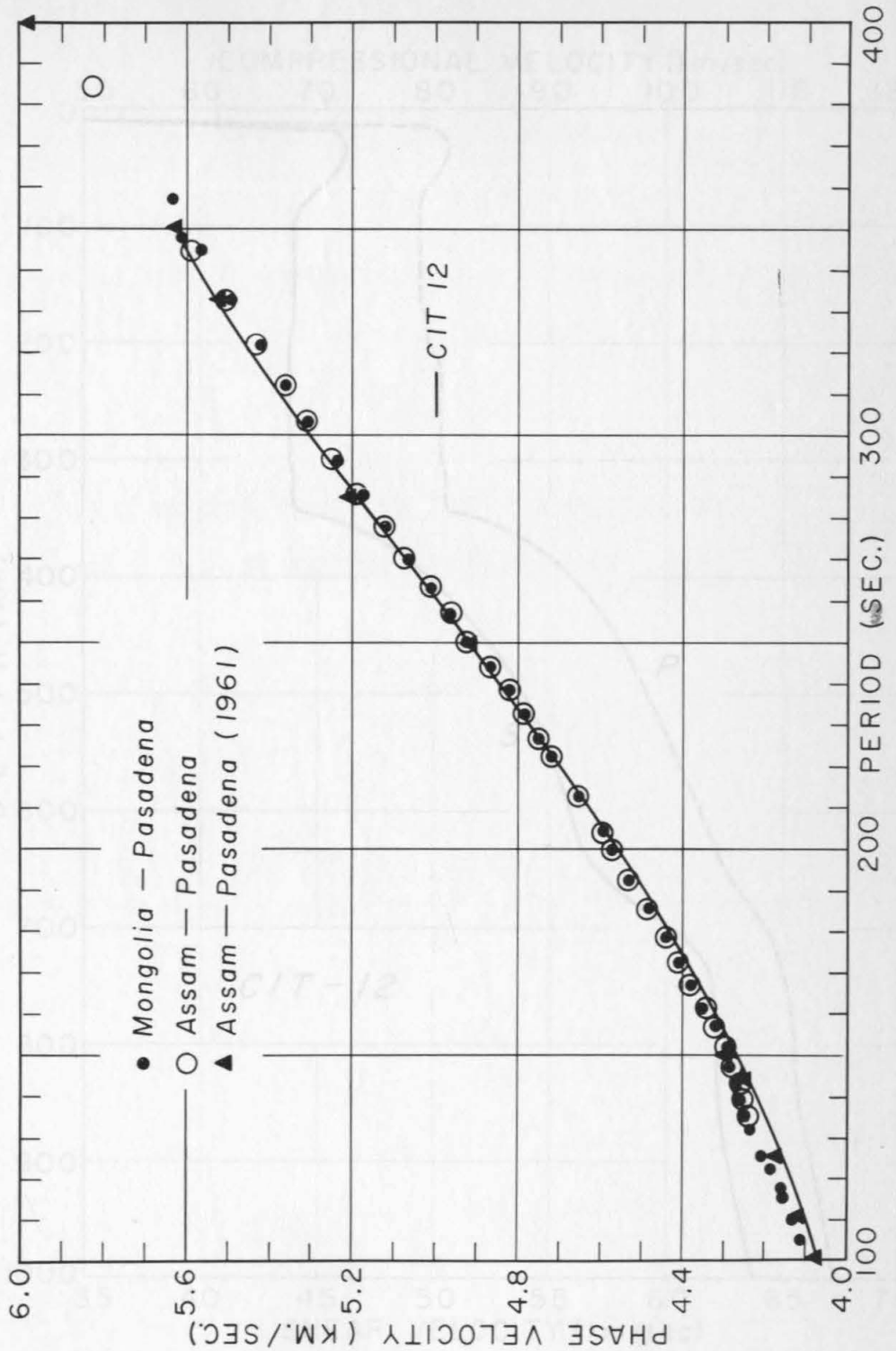
PHASE VELOCITY (KM./SEC.)
6.0
5.6
5.2
4.8
4.4
4.0
100
200
300
400
PERIOD (SEC.)
• Mongolia — Pasadena
○ Assam — Pasadena
▲ Assam — Pasadena (1961)
— CIT 12

Fig. 25

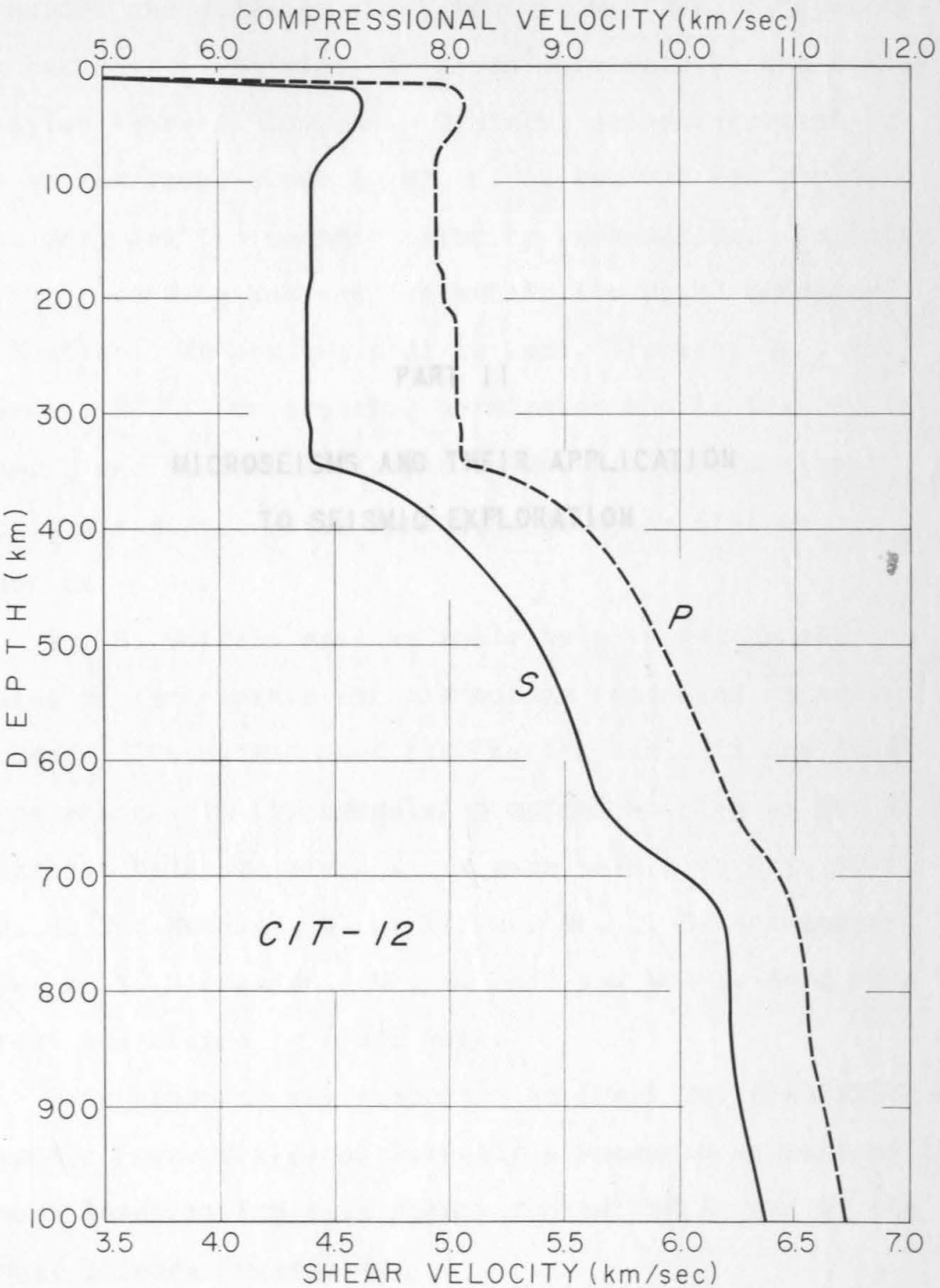
COMPRESSIONAL VELOCITY (km/sec)
5.0
6.0
7.0
8.0
9.0
10.0
11.0
12.0
0
100
200
300
400
500
600
700
800
900
1000
DEPTH (km)
P
S
CIT-12
3.5
4.0
4.5
5.0
5.5
6.0
6.5
7.0
SHEAR VELOCITY (km/sec)

Fig. 26

PART II

MICROSEISMS AND THEIR APPLICATION TO SEISMIC EXPLORATION

ACKNOWLEDGEMENTS

The author is indebted to Professor Frank Press for his support and guidance throughout this study. The microseism recordings in Tulsa, Oklahoma were made by the Jersey Production Research Company. Grateful acknowledgement is given to the Company and to Mr. F. G. Boucher for giving us the data and the seismic velocity information. In China Lake the recording was carried within the Naval Ordnance Test Station. We are grateful to Capt. Blenman, Jr., the Commander, NOTS, for granting permission and to Drs. P. St. Amand and K. Odencratz, and to Mr. R. Zbur for their valuable assistance while working within the Station boundaries.

Mr. N. Motta's most valuable help in design and building of instruments for microseism recording is acknowledged. The author used the Fourier analysis and least squares phase velocity computer programs written by Mr. S. S. Alexander. Valuable discussions were held with Drs. S. W. Smith, A. Ben-Menahem, W. L. Pilant, Mr. C. B. Archambeau, and Mr. S. S. Alexander. Mr. W. Taft and Mr. J. Romo were of great assistance in field work.

This research was supported by Grant No. AF-AFOSR-25-63 of the Air Force Office of Scientific Research as part of the Advanced Research Projects Agency Project VELA, and by the National Science Foundation.

The figure preparations were supervised by Mr. L. Lenches, and the author wishes to extend special thanks to him.

ABSTRACT

A study of microseisms is made to determine some of their statistical properties and to investigate the feasibility of their use in determining the shallow structures of the earth's crust by the phase velocity method. It is found that the microseisms in the period range of 1 to 6 seconds arrive from several directions with comparable strength and at the same time. There are occasional short intervals of 10 - 40 seconds during which microseisms are mostly unidirectional. It is also found that these relatively short period microseisms are not stationary in the wide sense over time intervals longer than 5 or 10 minutes.

The phase velocities of microseisms recorded with an array of 8 instruments are measured in four different locations. The velocities, although scattered, are found to be in agreement with the theoretical dispersion curve for the fundamental Rayleigh mode, computed using the available seismic velocity information. An error analysis is made and the confidence limits are placed within ±20 percent of the measured velocities.

TABLE OF CONTENTS

INTRODUCTION

In most earlier applications of the dispersive properties of surface waves to crustal studies, waves with periods longer than 10 seconds were used, and the near surface properties of the crust were ignored. The knowledge of the very shallow structure of the crust in localized areas carries great geologic significance. It is only in a very small fraction of the continents that the thickness of the sedimentary rocks have been investigated by gravity and by seismic reflection and refraction methods. The surface wave dispersion method could be used in such areas as well as the igneous and metamorphic regions for similar investigations, provided waves with short wavelengths can be recorded and their phase velocities can be measured.

One source of short period surface waves are microseisms. Although these waves are more complicated than the transient surface waves generated by earthquakes and explosions, their use is advantageous because they are universal and always present. This project was undertaken to evaluate the feasibility of measuring the phase velocities using a small multi-channel array of matched vertical seismometers, and determining the shallow structures from the observed phase velocity curves.

Microseisms have been investigated by seismologists since the advent of the science, and some papers on the subject were published as early as 1874 (de Rossi, 1874). Most of the studies in this field are directed toward the clarification of three major points: (1) The origin of microseisms, (2) nature of the microseismic waves, mode of propagation, and direction of approach, (3) some statistical properties of microseisms and their treatment as noise.

There are several well known theories of origin of microseisms, but no one theory completely accounts for all the observations (references are listed in Gutenberg and Andrews, 1952, 1956; Gutenberg, 1958; Haubrich and Iyer, 1962). It has been generally accepted that microseisms originate in the oceans or in great lakes. In this generalization the high frequency vibrations due to wind and industrial noise are excluded. Microseismic waves are of both Rayleigh and Love type with the Rayleigh waves being more common (Ramirez, 1940; Wilson, 1942; Blaik and Donn, 1954; Darbyshire, 1954; Deacon, 1954; Gutenberg, 1958; Jensen, 1958; Båth, 1962; Iyer, 1962). The periods of the waves extend from 0.2 second to 30 seconds (Oliver, 1962), with the most commonly observed spectral band being from 1 to 10 seconds. The waves are mostly of the fundamental mode with some higher modes at shorter periods (Gutenberg, 1958; Archambeau and Alexander, 1963). The direction of

approach of the microseisms varies with time, and usually the waves arrive in more than one direction at a given time (Kishinouye, 1947; Leet, 1949, 1950; Ramirez, 1953; Blaik and Donn, 1954; Donn, 1954; Gutenberg, 1958; Okano, 1961; Haubrich, Munk, and Snodgrass, 1963). The multi-directionality is due to extended and numerous sources and to lateral refraction and reflections (Blaik, and Donn, 1954; Donn, 1954). Microseismic waves are attenuated when crossing geologic discontinuities. Also, Rayleigh-to-Love conversion has been observed over the discontinuities (Gutenberg, 1958; Rykunov and Mishin, 1961).

With the interest in seismic noise and noise elimination, the statistical properties of microseisms have become important in recent years (Spieker, 1961; Haubrich and Iyer, 1962). Not enough work has been done in this field, however, to draw general conclusions.

A few attempts have been made for measuring the phase velocity of microseisms using a tripartite method (Ramirez, 1940; Mukherjee, 1948; Dinger, 1951; Lynch, 1951; Gutenberg, 1958; Okano, 1961; Rykunov, 1961). In most cases the measured velocities scattered greatly and were of no physical significance. In some other cases the average of the measured velocities was too high for the particular structure. In these measurements, however, the multi-directionality of

the waves and the fact that the tripartite array could be used only when the waves were unidirectional were not taken into account.

Before choosing the method of microseism phase velocity measurement, it was necessary to investigate the statistical properties and the multi-directionality in detail in the period range of our application (1 to 6 seconds). These investigations will be discussed briefly in the next section, then, the instruments designed for recording the microseisms in the field, the techniques used for phase velocity measurement, and the results obtained for four different areas will be described. Discussion of the interference effects, numerical sources of error, and the reliability of the measured phase velocities will precede the conclusions.

STATISTICAL PROPERTIES AND DIRECTION OF APPROACH OF MICROSEISMS

Statistical Properties

The investigation of the statistical properties of microseisms were not begun until recent years due to the fact that such an investigation requires great amounts of data in digital form or in analog form suitable for analysis. The first continuous digital recording of microseisms along with the correlation and cross-spectra results are described by Haubrich and Iyer (1962). Another group (Spieker, 1961) investigated the stationarity of microseisms in time and space. The latter study shows that, in general, microseisms recorded at a given station are not stationary over a time interval of one hour. In other words, the autocorrelation function is not invariant over such a time span. This implies that in any kind of analysis where stationarity is assumed time length cannot exceed one hour. In space, it was found that waves were "almost" stationary over a distance of one kilometer, where stationarity in this case refers to invariance of the time autocorrelation function from one station to another at the same time.

Since it is advisable to know the stationarity properties before the microseisms could be subjected to conventional spectral analysis, such a study was carried out

using the microseisms recorded in Pasadena by the Caltech digital seismograph. A series of autocorrelation functions of microseisms recorded on two different days were computed using 2 minute long records. Before the correlation the time series were filtered. The microseism spectrum covers a wide frequency band extending from about 0.03 cps to 10 (or higher) cps. One would not expect the properties to be the same over the entire frequency range, since microseisms within different bands are associated with different sources. The filtering was done to pass the waves in the period range of our interest, 0.5 to 5.0 seconds. The autocorrelation functions $R_t(\tau)$ were computed using record segments starting at t = 0, 3, 6, 13, 20, and 27 minutes. These are shown in figure 1 for two different days: September 18, 1962 and January 30, 1963.

Now, let us compare the autocorrelation functions for different origin times. If microseisms were stationary in the general sense, the autocorrelation functions would be identical. In looking at the January 30th case, one sees that from t = 0 to t = 3 minutes $R_t(\tau)$ changes some, but peak-to-peak correspondence is good. From t = 3 to t = 6, the change is more obvious. $R_t(\tau)$ at t = 6 and t = 13 are very much alike. So is the case for t = 20 and t = 27. But, from t = 6 to t = 20 minutes, there is a very definite change in the shape of $R_t(\tau)$.

For September 18th microseisms, one observes a more systematic change in $R_t(\tau)$ as t increases from $t = 0$ to $t = 3$ and $t = 6$ minutes. For the 7 minute jumps in the origin times the variations in $R_t(\tau)$ are outstanding. From these examples it can be concluded that in this particular period range (0.5 to 5 seconds) the microseisms appear to be stationary for time intervals less than about 10 minutes. For longer time durations they are not stationary.

The implications of nonstationarity is that the correlation functions and power spectra are time dependent, and cannot be treated simply as functions of frequency. Depending on the rate of time variation, the correlation functions have to be computed over relatively short time intervals and the power spectra have to be obtained by taking the Fourier transform of these short time functions. These time dependent spectra are called "instantaneous spectra" (Page, 1952; Silverman, 1957). They could be considered the generalized spectra with the conventional, time independent spectra being a special case. In practice, however, the use of the instantaneous spectrum concept is limited to special cases.

One question may arise in regard to our stationarity test. The autocorrelation functions were computed using finite records of 2-minute durations. In the rigorous definition of the correlation functions of aperiodic time

series, the limits are extended to infinity. In practice this is not possible, and one is limited to the finite record lengths. A process which might be stationary in reality, could be found to be nonstationary in practice when finite time intervals are used in testing. It is useful from the practical point of view to define stationarity in terms of the time durations pertinent to a given experiment, since infinitely long time intervals cannot be realized.

Another statistical property of microseismic waves that requires investigation is their variation in space. A measure of this variation can be obtained by computing the coherence between the simultaneous recordings at two stations. Since microseisms are continuous wave trains, coherence R would be equal to one for unidirectional stationary arrivals. Any deviation from R=1 would be due to the interference of uncorrelated waves, and R would decrease with the increasing interference. The coherence between recordings at two stations with varying distances was computed using a unidirectional, 45-second long section of the microseisms recorded in the Imperial Valley, California. The traces recorded simultaneously at five stations were digitized at the rate of 10 samples per second. The digital data were detrended and filtered with a low-pass digital filter with cut-off at one second. Power spectra were obtained from the Fourier transform of the two-sided covariance functions, and

the coherence between pairs of stations was computed using the definition given in the Appendix. The results for five distances are shown in figure 2. Over a distance of 1.5 km the waves are coherent although there is a very slight decrease in coherence with increasing distance. This decrease is more pronounced at shorter periods.

The spatial coherency of the waves is a very important test for the feasibility of the phase velocity method. Unless the waves can be correlated from one station to another, they cannot be used for phase velocity measurements. Figure 2 illustrates the excellent interstation coherence of the recorded microseisms over the maximum dimensions of the array. For periods longer than 2 seconds the coherence is always larger than 0.8.

Direction of Approach of Microseisms

Several methods are used for determining the direction of approach of microseisms. Three methods using the horizontal and vertical components of the motion are described by Båth (1962). The tripartite method utilizes the same component of the motion at three stations. The "cross-spectrum" method utilizes the complex cross-spectral components of the three-component station to give the direction of arrival. The azimuthal angle θ is given by

$$\theta = \tan^{-1} \frac{Q_{NZ}}{Q_{EZ}} \qquad (1)$$

where N, E, Z, refer to north, east, and vertical components, and Q_{ij} is the imaginary part of the complex spectrum $S_{ij} = C_{ij} + iQ_{ij}$. A parameter characteristic of the beam width is (Haubrich, Munk, and Snodgrass, 1963).

$$B = \frac{Q_{NZ}^2 + Q_{EZ}^2}{C_{ZZ}\,(C_{NN} + C_{EE})} \qquad (2)$$

For Rayleigh waves approaching from a single direction B=1, and for waves arriving with uniform density from every direction B=0. In general the beam width is found to be less than B=0.5 (Haubrich, Munk, and Snodgrass, 1963) indicating that the direction of arrival is not unique.

All the above methods of determining the direction of microseisms would work as long as the basic assumption that the microseisms consist of unidirectional Rayleigh waves, or uncorrelated Rayleigh and Love waves would hold. In the absence of these conditions, which in general is the case, the direction determined by any one of these methods is some kind of an average which has no physical significance.

A method which is most suitable for the study of microseism direction is the particle trajectory method. For pure unidirectional, fundamental mode Rayleigh waves the two horizontal, north and east, components of the motion are linearly related, while, in general, the particle motion traces a retrograde ellipse in the vertical plane. Two examples of such motion for microseisms are shown in

figures 3a, 3b, 3c. The data was taken from the Caltech digital seismograph and narrow-band filtered around the period T = 4 second to minimize the interference of other frequencies. All these figures show that in these cases the particle motions in the vertical plane are undisturbed retrograde ellipses. Hence, these waves consist of uni-directional fundamental mode Rayleigh waves. The direction can be computed with an accuracy of better than ± 5 degrees. Figure 4 illustrates the case where the wave is not a uni-directional, pure Love or pure Rayleigh wave. Figures 5a and 5b show two cases where the direction of the interfered wave changes by about 90 degrees within 11 and 25 seconds, respectively. The effectiveness and the accuracy of the direction from orbital motion can be illustrated with the identification of the P and the SH waves from a small tremor during a strong microseismic storm on January 30, 1963. Figure 6 shows the linear relations between the N-S and E-W components and the rotation of the line of polarization by exactly 90 degrees from P to SH. The earthquake was so small ($M < 3$) that it was recorded on the digital seismograph which was running at a very high gain, and was not visible above the noise level on photographic recordings in Pasadena. Okano (1961) carried out a similar investigation of micro-seism motion using a vector seismograph. His conclusions

also support the rapid interference and direction changes of microseismic waves.

The rapid changes of direction introduce the most serious difficulty in the measurement of phase velocity of microseisms. The effect of interference on the observed phase velocity of the waves is derived later for special cases. When interfered, the waves are modulated in space, and if a simple tripartite array were used for phase velocity measurement, in general it would not be possible to correlate the peaks from one station to another. If the phase differences were measured from Fourier phase spectra or cross-spectra, the results would have no physical significance since the spectra cannot be written as the product of a space independent amplitude factor with an exponential phase factor. In previous phase velocity measurements these complications were ignored, and as a result no reasonable phase velocity curve was obtained for microseisms. A typical example of such an effect is illustrated by Okano (1961, figure 12) where the phase velocities of 3 to 5 second microseisms are uniformly scattered between 1.0 km/sec and 3.0 km/sec.

A METHOD FOR MEASURING PHASE VELOCITY OF MICROSEISMS

A method that is to be used for measuring phase velocity of microseisms must have the following properties: 1. It must work with time records 20 - 30 seconds long, 2. it must have some provision for identifying interfered and pure unidirectional wave trains, 3. it must have enough accuracy for measurement of phase velocity over small arrays.

The limitation of record length arises from the fact that it is only possible to find short segments of the record where the microseisms are unidirectional. Since cross-spectra cannot be used with such short record lengths, Fourier phase spectra and direct time delay measurements have to be utilized between stations. The second requirement is to assure an uninterfered wave train regardless of length, and it can be realized by using a close array of stations to follow the progress of the wave train. The restriction on the maximum size of the array is due to the fact that shallow structures of the earth's crust may change rapidly, and the array must be small to measure velocities over limited areas. To meet these qualifications special instruments were built, and phase velocities were measured at four different locations.

Instrumentation

A set of 8-channel portable instruments were designed and built for field recording of microseisms. In designing the instruments the author placed emphasis on matching the phase response of the system rather than shaping the amplitude response curve. Otherwise instrumental effects would mask the phase difference of the signal, which over a short array is only a small fraction of a circle. The seismometers used were modified, one second, variable reluctance, portable Benioff instruments. The periods were made adjustable by using an external suspension system and varying the axes of the suspending negative length springs from the vertical. The maximum deviation between the seismometer periods was kept less than 2 percent of the mean period. The signal from seismometers was transmitted to a test panel in the recording trailer using seismic cables. The seismometers were run at critical damping where the damping resistance, taking into account the cable resistance, was adjusted at the input of the amplifiers.

The amplification was done by transistorized, double-loop, D-C amplifiers with a maximum voltage gain of 200,000. A low-pass R-C filter unit with three different roll-off frequencies and slopes of either -12 or -18 db/octave was inserted between the two stages of the amplifier. In

construction of the filter 1 percent resistors were used and capacitors were bridged closer than 0.01 μf to minimize the differential phase shift between channels. The outputs of the amplifiers were capacity coupled to balanced dual emitter followers. The time constant of these couplings was an order of magnitude larger than that used between the amplifier loops, and hence, it had no effect on the frequency band of interest. The emitter followers were coupled through minimum loss networks to "T" pads and these to recording galvanometers. The need for such a coupling network arose because of the low impedance of galvanometers (12 ohms) and the 1,000 ohm minimum limit on the load impedance of the amplifiers. The paper speed in the camera was variable from 0.5 to 4 cm/sec. The timing signals were provided by a Times Chronometer, and 0.2 second, 1 second, and 1 minute marks were put on the record. The block diagram of the whole system is shown in figure 7, and the frequency response to ground displacement with intermediate stage filtering is given in figure 8.

To insure the uniformity of the response during field operations a series of test circuitry was built into the test panel for checking the response of the amplifier-filter unit, total system response, and free period of seismometers. The tests were performed for eight channels

at the same time by means of a central switching system. The seismometer periods were measured for instance, by switching 1 megohm resistors to the amplifier inputs, displacing the mass by putting D.C. current through the seismometer coils and then turning the current off and recording the motion of the undamped oscillations of the pendulums. The system response was measured to a step-function input by a similar procedure.

Field Procedure

An L-type seismometer array was adapted for recording of the data in the field. Three seismometers were placed on each line with one or two seismometers at the apex. The maximum length of the lines was 1590 meters, and this dimension was adapted as an optimum length for measuring time delays with reasonable accuracy and yet being small enough to assure good correlation and localization over a uniform portion of the geologic structures. The seismometers were set on the surface and covered to minimize the direct effects of the wind and the sun. At each location several recordings of 5 - 15 minutes length were made with appropriate gain and filter settings. Before and after each recording the response of the system and seismometer periods were checked using the central test panel.

Analysis of Data

The long recordings were visually edited to find the portions of the record with the least amount of interference and most suitable for analysis. The selected segments of the photographic traces were digitized at 0.1 second intervals, and the analyses were carried out on the IBM 7090 computer. In the analysis the digital data were detrended, filtered with appropriate digital filter, and the resulting time series was plotted for re-examination. The time delay from one channel to another was determined by one or more of the four different methods.

1. The peak-to-peak correlation was carried out over all the stations. Since the distances between stations were small compared to the wavelength, such correlations were valid. The difficulty in this method, however, arises in determining the periods exactly (Toksöz and Ben-Menahem, 1963).

2. A coherent segment of the record was Fourier analyzed and the time delays were computed from the differences of Fourier phase spectra. When a very short section of the record is being analyzed, the number of independent spectral estimates, hence the number of phase velocity points, is very small since frequency increment is given by

$$\Delta f = \frac{1}{2T} \qquad (3)$$

where T is the length of the time series. Also, in such a case, the finiteness effects of the time window are significant. If a long section of the record were chosen, the Fourier phases would be affected by the small incoherent segments that might be included.

3. Where the record lengths permitted, cross-correlation of the narrow-band-pass filtered traces was done to determine the time shift of the maximum of the cross-covariance function. This procedure is similar to (1) but it averages over all the peak-to-peak correlations and requires a longer time series. Microseisms arrive in bursts. If the distance between stations were large and the time delay in the order of a length of a burst, then the maximum of the cross-covariance function would be controlled by the envelope, and hence, the group velocity. When the record length is short and the time delay very small compared to the length of a beat, the cross-covariance function would depend on individual oscillations. In other words, the correlation would be peak-to-peak rather than envelope-to-envelope. As a result the time shift would be controlled by the phase velocity. In our analysis, short segments of recordings from near stations were used. Hence, the velocities computed from the time delays were the phase, and not the group velocities.

4. The cross spectra were obtained from the covariance functions, and the phases were used to compute the time delay. For an 8-channel array the spectral density matrix is an 8 by 8 Hermitian matrix for each independent spectral estimate. For practical reasons only one column and row of this matrix was used in computing phase velocities. This method, too, is limited because it requires long, pure time series.

The phase velocities were computed for each frequency using the observed time delays, and the coordinates of the stations in the array. Let t_{ij} be the arrival time of the j^{th} phase at the i^{th} station. Then

$$t_{ij} = \Delta_i \cos \alpha_i \frac{\cos \delta_j}{C_j} + \Delta_i \sin \alpha_i \frac{\sin \delta_j}{C_j} + t_{oj} \qquad (4)$$

$$= a_i X + b_i Y + C_i Z$$

where Δ_i = distance from the origin to the i^{th} station, α_i = the azimuth of the i^{th} station, δ = azimuth of the normal to the wave front, C = phase velocity,

$$X = \frac{\cos \delta_j}{C_j} \quad , \quad Y = \frac{\sin \delta_j}{C_j} \quad , \quad \text{and } Z = t_{oj}.$$

The three unknowns, X, Y, Z, in equation (4) can be solved for if data are available from at least three stations. If more than three stations are available, then a least squares solution can be obtained and the standard deviation, σ,

can be computed (Wilson, 1957; Aki, 1961; Young, 1962).

$$\delta = \tan^{-1} (Y/X)$$

$$C = (X^2 + Y^2)^{-\frac{1}{2}} \qquad (5)$$

$$\sigma_\xi = \left[\sum_k \left(\sigma_{x_k} \frac{\partial \xi}{\partial x_k} \right)^2 \right]^{\frac{1}{2}}$$

where ξ corresponds to C, or δ. This method gives a measure of interference by the magnitude of the standard deviation, since in case of interfering wave trains the observed phase velocity changes in space. In all measurements the standard deviations of the phase velocity and direction were used as criteria for weighing the reliability of the computed phase velocities. Also in computing, stations were dropped from the array one at a time, and each time the velocity was computed using the new array with one less station. This is reasonable since local interference may affect one station and not the others, and its inclusion in computations contributes large amounts of error into the phase velocities.

RESULTS FOR DIFFERENT REGIONS

Microseism field measurements were carried out at two regions, Imperial Valley, California and within the Naval Ordnance Test Station at China Lake, California using the 8-station array described in the previous section. In addition to this, microseismic data supplied to us from measurements near Tulsa, Oklahoma were used. The structures and velocity-depth curves were known for China Lake and Tulsa locations. In Imperial Valley, only gravity profiles were available at the locations where microseisms were recorded.

China Lake: The microseism measurements were carried out in July, 1962. This area was chosen because of the availability of roads away from the domestic noise centers, and for the reason that structure was known from detailed gravity and seismic investigation. Because of excessive heat, however, many problems were encountered in recording. A sample of the microseisms recorded in the deepest part of the basin at China Lake and the geometry of the array are shown in figure 9. Figure 10 shows the geologic section, obtained by seismic refraction and gravity interpretations (Zbur, 1962). The two thin layers at the top of the section consist of loose sand and shaley sands. The third layer is made of lake beds which contain some pyroclastics. The

thickest sedimentary layer consists of sandstone, silty sandstone, and some conglomerates. The basement rock is granidiorite (Zbur, 1962). The Poisson's ratios that are listed for computing the shear velocities from compressional velocities were averaged from measured results for similar rock types (Heiland, 1946, p. 467). The theoretical Rayleigh wave phase velocity curves for the fundamental and first higher modes along with the experimental phase velocity points, measured using Fourier analysis and peak-to-peak correlation methods, are shown in figure 11. The phase velocities were computed within a narrow spectral band between periods of 2 and 6 seconds. At longer periods, the relative amplitudes were very low, and the phase results were not reliable. At shorter periods, the interstation coherence was low due to excessive interference of short period microseisms. The decrease in coherence for periods shorter than 2 seconds was also observed at other locations, and the phase velocity measurements could not be extended much below this limit. The direction of approach of microseisms at China Lake was from the southwest.

In examining figure 11, one observes that the experimental points agree reasonably well with the theoretical phase velocity curve of fundamental mode Rayleigh waves. This confirms the results of the particle motion studies described earlier; namely, the Rayleigh wave portion of

microseisms in this period range consists of fundamental mode. The agreement between the theoretical curve and the experimental points in figure 11 shows that the phase velocity of microseisms can be measured with a reasonable accuracy using an array of closely spaced stations and the method of analysis described above.

Tulsa: Some microseism recordings were carried out at the Earth Sciences Laboratory of the Jersey Production Research Company using 2-second modified gravimeters in a tripartite array. The records as well as the time-depth curve from a velocity survey were given to us. Figure 12 shows a sample record. Figures 13 and 14 are the power spectral density of the center trace and the coherence between the center and the E traces, respectively. The structure and measured compressional velocities with assumed density and Poisson ratios are shown in figure 15. The experimental phase velocities were computed using the Fourier phase spectra of 40 second segments of the record, and by peak-to-peak correlations in the time domain. The results obtained using the cross-spectra of a long record were scattered to such an extent that they could not be considered reliable. The theoretical phase velocity curves and experimental points are shown in figure 16. The observed phase velocities are evenly scattered around the theoretical curve.

In this case, too, phase velocities were measured over a limited period range between 1.5 and 5 seconds. The direction of approach of these waves was from the northeast. For the long period microseisms whose periods are longer than 7 seconds, the phases were not accurate enough to compute the phase velocities; but, the direction could be determined approximately. These long period microseismic waves were arriving from the southwest, which means that the source was in the Pacific Ocean, and the waves had propagated across the continent. There was other evidence indicating that the waves in the short and long period ranges were from independent sources. The power spectral density shown in figure 13 has two broad peaks: The main peak centered around T = 4 seconds, and the secondary peak around T = 10 seconds. Between T = 5 and T = 8 there is a low-power band. This is also confirmed by the coherence shown in figure 14. The interstation coherence in the period range of 5 to 8 seconds has a minimum. For period longer than 8 and shorter than 5 seconds the coherence is very close to 1.0. In conclusion we can say that, in this case, microseisms in these two frequency bands were not related. As the direction determinations show, the long period microseisms originated in the Pacific Ocean and the shorter period microseisms in the Atlantic.

Let us now make a comparative study of phase velocity measurements in China Lake and in Tulsa. Although the recording instruments were different at these two locations the quality of the records are about the same as figures 9 and 12 illustrate. The procedure of digitization and analysis were identical in both cases. The structures are known equally well under both of the recording sites. In each case the observed phase velocities of Rayleigh wave microseisms correspond to the fundamental mode. Yet, as the comparison of figures 11 and 16 demonstrates the agreement between the experimental phase velocity points and the theoretical curve is much better in the case of China Lake as compared to Tulsa. The reason for this is the superiority of the multi-channel array as compared to the tripartite method. In the case of the tripartite array any error that is made in measuring phases or time delays directly affects the phase velocity. In the case of the multi-channel array the individual station errors tend to average out statistically, to minimize the effect on measured phase velocities.

Imperial Valley: In the case of China Lake and Tulsa sites, the structures (i.e. depths, compressional velocities, and densities) were known. The agreement between the measured phase velocities and the theoretical values were reasonably good. Now, the technique will be used to determine the structures in an area where, a priori, the exact

velocity distribution is not known. Microseisms were recorded at two locations near El Centro and Holtville, California to interpret the results and to determine the thickness of the sedimentary layer. The locations, labeled Imperial-1 and Imperial-2 are shown on a map in figure 17. Imperial-1 is situated in the center of a negative gravity anomaly (Kovach, 1962). The array and a sample record are exhibited in figure 18. Phase velocities were computed from Fourier phase spectra of three different segments of the record and also from peak-to-peak correlations using the digitally filtered records. Fourier amplitude and phase spectra of one record segment is shown in figure 19. The dips in the amplitude spectrum followed by a change of slope or minimum in the phase spectrum are the results of interference.

The experimental phase velocities as well as two theoretical phase velocity curves for two different models are given in figure 20. The elastic parameters for models A and G are listed in Table 1. In model A, the depth to the igneous basement is the same as that given by Kovach (1962) from the interpretation of his gravity data. The velocities were projected from the results of seismic refraction profiles located approximately 18 km from the area. Model G is what is considered to be "the best fit" to the experimental phase velocities. Since the data are scattered, it is difficult to define objectively what the

"best fit" should be. The steepest portion of the phase velocity curve is controlled by the depth to the basement, and it is not likely that one can keep the depth given in model A and vary the velocities within the limits measured for the area to obtain a good fit to observed phase velocity data. Kovach (1963, personal communication) has commented that the depths computed from the gravity data may have an uncertainty of 10 percent. A decrease in depth of 10 percent will make the structure 1-A very close to 1G.

The experimental phase velocities measured from the Imperial-2 recordings are shown in figure 21. With each point, the standard deviation is also shown. The theoretical model was computed using the depths and velocities of Kovach's refraction Profile 3 located about 5 km north of the Imperial-2 recording site. The phase velocity parameters, as well as the parameters for the Profile 3 are given in Table 2. It may be noted that, in this case, the basement depths of both models agree. The above examples are the first attempts made to use microseisms to infer something about the structure. In these cases we had some knowledge of the velocity of rocks. Without the velocity information, it would be more difficult to determine the structure with data over a limited frequency band. In a basin, if the velocity contrast between the sedimentary rocks and the basement rocks is high, then a typical phase velocity curve

would have a steep portion. The period range over which the slope is large would strongly depend on the depth to the basement. The flat portions of the curve, of course, would be controlled by the basement velocity at long periods, and by the near surface sedimentary rock velocities at short periods. Once this information is extracted from the data, the inversion from the dispersion data to the structure would not be difficult. In general, structures encountered in this application would not exceed 5 or 8 layers, and the uniqueness problem would not be a very serious obstacle, if sufficient data over a wide frequency band are available.

SOURCES OF ERROR AND RELIABILITY OF MEASUREMENTS

Before going into the evaluation of the applicability of the microseism phase velocity method, it is necessary to discuss the two major sources of error. These are interference and errors made in measurement.

Interference

It was pointed out earlier that microseisms are not unidirectional but in general arrive from different directions at the same time. The interfering wave trains may be of the same or of different periods. To evaluate the effects of interference on the phases it is necessary to formulate the problem and solve it for at least special cases.

Let us assume that microseisms are plane waves of Rayleigh type traveling in a horizontally homogeneous layered medium. Considering only the steady state case, the displacement at the surface can be represented as

$$W = A\, e^{i(\omega t - \underline{k} \cdot \underline{r})} \tag{6}$$

where $\underline{k}$ = vector wave number, and $\underline{r}$ = position vector. In Cartesian coordinates

$$\underline{k} \cdot \underline{r} = k\,(\ell x + my) \tag{7}$$

where $k = \frac{2\pi}{\lambda} = \frac{2\pi}{CT}$, C being the phase velocity and T the period. ℓ and m are the direction cosines of the wave front normal.

In the case of the waves arriving from different directions, it is necessary to superimpose all the arrivals at a given location. Let θ be the azimuth angle and let $f(\theta,\omega)$ represent the spectral amplitude of the wave of frequency ω arriving from direction θ. The direction cosines are $\ell = \cos\theta$ and $m = \sin\theta$. The total displacement is a double integral over the azimuth and frequency

$$W(t,x,y) = \int_{-\infty}^{\infty}\int_{-\pi}^{\pi} f(\theta,\omega)e^{i\omega t}e^{-ik(\omega)(x\cos\theta+y\sin\theta)}\,d\theta d\omega \qquad (8)$$

If only a single frequency ω is considered,

$$W(t,x,y) = e^{i\omega t}\int_{-\pi}^{\pi} f(\theta,\omega)e^{-ik(x\cos\theta+y\sin\theta)}\,d\theta \qquad (9)$$

We can examine (9) for special cases.

1. Two monochromatic waves arriving from opposite directions:

Choosing the coordinate system such that the waves are propagating along the X - axis and using $A = f(\theta=0^o)$, $B = f(\theta = 180^o)$ and $r = \frac{B}{A}$, equation (9) becomes

$$W(t,x) = A\,e^{i\omega t}\,(e^{-ikx} + r\,e^{ikx}) \qquad (10)$$

Re-writing (10) so that the phase term is factored out

$$W(t,x) = C\, e^{i(\omega t - \bar{\varphi})} \qquad (11)$$

where

$$C = A\left[1 + 2r\cos 2kx + r^2\right]^{\frac{1}{2}}$$

$$\bar{\varphi} = \tan^{-1}\left[\frac{1-r}{1+r}\tan(kx)\right]$$

It is obvious that the resultant wave is modulated in space, and it cannot be expressed as the product of a constant amplitude factor and a phase factor. In other words, we can no longer define a physically meaningful phase velocity. Suppose that the amplitude modulation factor is ignored and $\bar{\varphi}$ defined in equation 11 is taken as a "pseudo phase" and used in phase velocity computation. The measured phase velocities, then, would depend on the location (i.e. the X-coordinate) where the measurement is made.

To clarify this point, let us compare the phase of the pure wave, φ, with the "pseudo phase" of the interfered wave. The differential phase $\xi_\varphi = \bar{\varphi} - \varphi$ is shown in figure 22 as a function of the dimensionless coordinate $\frac{X}{\lambda}$, where λ = wavelength. In this plot the parameters are: amplitude ratio $r = 0.2$, the wave number of the pure wave $k = 1\ km^{-1}$, and the true phase velocity in the medium is $C = 2$ km/sec. Figure 22 clearly illustrates how the difference between the "pseudo phase" and the true phase oscillates

about the zero mean. This means that the phase of the interfered wave would lead that of pure wave at some locations and lag behind at others. The amount of maximum lead or lag would depend on the amplitude r of the interfering waves.

The obvious implication of this interference is that if one were to measure phase velocities assuming that there were a single wave train, the measured "pseudo phase velocities" would oscillate about the true value. Such minima and maxima in the phase velocities were observed over continental margins and two-dimensional sloping crust model (Alexander, 1963). In this case, the direct and reflected waves interact over the margin to set up the interference form.

II. Two equal-amplitude waves interfering perpendicularly:

Taking the coordinate axes such that one wave is propagating in the X- and the other in the Y-direction, from equation 9 one can write

$$W(t,x,y) = A\, e^{i\omega t} \left\{ e^{-ikx} + e^{iky} \right\} \qquad (12)$$

Combining the two terms to factor out a "pseudo phase" term, one gets

$$W(t) = 2A \cos \frac{k}{2} (x + y)\, e^{i\left[\omega t - \frac{k}{2}(x - y)\right]} \qquad (13)$$

This wave is also modulated in space and the apparent "pseudo phase velocities" vary between $\bar{C} = \infty$ for the X = Y line and $\bar{C}$ = C for the X = -Y line.

Measurement Errors

Because of the small size of the array, and the very small time differences used in computing phase velocities, the small errors made in measurements could affect the accuracy of the results significantly. These errors arise from three sources: (1) Mismatch in the instruments, (2) errors introduced in digitization, (3) numerical errors introduced in processing of the digital data.

In design and building of the microseism recording instruments, every attempt was made to minimize the phase differences between the different channels. The filter components were matched to better than 1 percent, and seismometer periods were adjusted such that at any one recording the maximum variation between periods was less than 2 percent. In addition to system checks, at least one test was made at each field location by setting all the seismometers within a small circle and recording microseisms. No differences could be observed visually between the 8 traces recorded. In the light of all these tests, it is safe to assume that the phase mismatch between different channels is in the order of ± 0.005 circles if not less. A phase

error of this order, however, could result in significant percentage error in phase velocities of longer period microseisms.

The digitization errors arise from the inability to read the center of a finite width trace as well as the limited accuracy of the digitizing devices. Let us suppose an error with standard deviation of 0.5 mm is introduced during digitization with a scale setting of 10 cm = 1,000 units. Then the error corresponds to $\sigma_n = 5$ units. The important question is how does this error propagate, and how does it affect the Fourier phases? Let us assume this error can be represented as a Gaussian random variable $n(t)$ with zero mean and constant power spectral density in the period range of interest. The Fourier cosine and sine coefficients of this random variable are also normally distributed. This can be proven starting from the definition of the coefficients a_k and b_k (Laning and Battin, 1956, p. 157)

$$a_k = \frac{2}{T} \int_0^T n(t) \cos k\omega t \, dt$$

$$b_k = \frac{2}{T} \int_0^T n(t) \sin k\omega t \, dt \qquad (14)$$

where k = integer, $\omega = \frac{2\pi}{T}$, and T = record length. Define the functions $C_k(t)$ and $S_k(t)$ by

$$C_k(t) = \begin{cases} \frac{2}{T} \cos k\omega t & \text{for } 0 \leqslant t \leqslant T \\ 0 & \text{otherwise} \end{cases}$$

and (15)

$$S_k(t) = \begin{cases} -\frac{2}{T} \sin k\omega t & \text{for } 0 \leqslant t \leqslant T \\ 0 & \text{otherwise} \end{cases}$$

Making use of the relations

$$C_k(\tau) = C_k(T - \tau)$$

$$S_k(\tau) = -S_k(T - \tau) \qquad (16)$$

equation 14 can be written as

$$a_k = \int_0^T C_k\,(T - \tau)\; n(\tau)\; d\tau$$

(17)

$$b_k = \int_0^T S_k\,(T - \tau)\; n(\tau)\; d\tau$$

Since integrals in (17) are convolution integrals, a_k and b_k can be considered as the responses of linear filters to the input n(t). Therefore, a_k and b_k are Gaussian random variables.

The variance σ_f^2 of a_k and b_k is given in terms of the power spectral density $N(f_k)$ of n(t) by (Laning

and Battin, 1956, p. 160)

$$\sigma_f^2 \simeq N(f_k)\,\frac{1}{T} \tag{18}$$

In equation 18 terms of the order of $\frac{1}{T^2}$ are neglected. Now, let us find the relation between σ_f^2 and σ_n^2. Since it is assumed that the noise is white in the frequency band of interest and that the noise power is zero outside this band due to pre-analysis filtering, then

$$N(f) = \begin{cases} N_o & |f_1| \leq |f| \leq |f_2| \\ 0 & \text{otherwise} \end{cases} \tag{19}$$

Representing the time autocorrelation function of $n(t)$ as the transform of the spectral density and assuming the process is ergodic, one obtains (Davenport and Root, 1958, p. 105)

$$2T\,R(\tau) = \frac{2N_o}{\pi\tau}\,\sin 2\pi\tau\,\Delta f\,\cos 2\pi\tau\,f_o \tag{20}$$

where $$f_o = \frac{f_1 + f_2}{2}\,, \quad \Delta f = \frac{f_2 - f_1}{2}$$

The variance of $n(t)$ can be defined in terms of the autocorrelation function

$$2T\sigma_n^2 = R(0) = 2N_o\,\Delta f \tag{21}$$

In this particular case $\Delta f \simeq 1$ cps, since frequencies

higher than 1/2 cps are filtered out. Then, from equations 18 and 21

$$\sigma_n^2 \simeq \sigma_f^2 \tag{22}$$

which implies that the variance of the Fourier coefficients of the random noise is the same as that of the noise.

Let $y(t)$ represent the microseism signal $s(t)$ plus the white Gaussian digitization noise $n(t)$,

$$y(t) = s(t) + n(t) \tag{23}$$

The Fourier coefficients of $y(t)$ would also have a normal distribution with a mean equal to that of $s(t)$ and variance of σ_f^2. Since the records are detrended prior to the analysis the mean of $s(t)$ is zero. Let C_c and C_s be the Fourier cosine and sine coefficients of $y(t)$. The phase is

$$\varphi = \tan^{-1} \frac{C_s}{C_c} \tag{24}$$

and the variance of the phase is

$$\sigma_\varphi^2 = \sum_i \left(\frac{\partial \varphi}{\partial C_i}\right)^2 (\sigma_i)^2 = \sigma_f^2 \sum_i \left(\frac{\partial \varphi}{\partial C_i}\right)^2 \tag{25}$$

where C_i refers to C_c and C_s. Leaving out the algebra, equation 25 can be reduced to

$$\sigma_\varphi^2 = \frac{\sigma_f^2}{A^2} \tag{26}$$

where A is the Fourier amplitude.

The error in the phase velocity C can be expressed in terms of the error in the phases. Since $C = \frac{X}{t} = \frac{X}{T(\Delta\varphi)}$, the fractional error is

$$\frac{\partial C}{C} = -\frac{\partial \varphi}{\Delta \varphi} \tag{27}$$

In terms of standard deviations

$$\sigma_c = \frac{C}{\Delta \varphi}\, \sigma_\varphi \tag{28}$$

To have a better idea about the size of the phase velocity error, it is helpful to use a numerical example. For a typical record analyzed A = 400, the standard deviation of the error in the phase is $\sigma_\varphi \simeq 0.0125$ circles. If the phase velocity is computed between two stations 1 km apart, and if the true phase velocity at T = 4 sec is C = 2 km/sec, then from equation 28 the standard deviation of the phase velocity at 4 seconds is σ_c = 0.2 km/sec or 10 percent of the phase velocity. For most of the microseism phase velocities measured using the Fourier phase spectra this error figure is a typical value. In the case of phase velocities measured by peak-to-peak correlations the peaks at best can be timed to ± 0.05 seconds. In addition here, there is the uncertainty of period measurements (Toksöz and Ben-Menahem, 1963).

The truncation and computer round-off errors are negligible compared to other errors where the amplitudes are

large. It is only at very small amplitudes that these errors become appreciable and the phases unreliable.

Reliability of the Results

Combining all the errors from the various sources described above, we can set-up a confidence limit applicable to the phase velocities measured. If a tripartite array were used, and unidirectional microseismic waves were recorded, then the only sources of error would be instrumental errors, and errors introduced during the process of the phase velocity computation. These are independent errors, and the standard deviation of the fractional errors in phase velocity due to each one could be as much as 10 percent of the phase velocity. If there is interference, then there is no bound to the maximum error. In the case of a multi-channel array the errors would be less due to averaging. When an 8-channel array is used instead of 3 stations, the standard deviation of the error is reduced by the factor of $[3/8]^{\frac{1}{2}} = 0.61$. Of course interference errors, which are always present to some extent in the case of microseisms, would increase this error figure. It is for these reasons that the confidence limit was set at 20 percent, and phase velocities with standard deviations higher than the 20 percent of the mean value were rejected.

CONCLUSIONS

The attempt to find a method of measuring the phase velocity of microseisms and using the phase velocity curve to determine the shallow crustal structures resulted only in partial success. When the project was planned the complications resulting from interference were underestimated, and it was hoped that there would always be a single direction from which the significant fraction of microseisms arrived. In such a case, small amounts of microseisms arriving from other directions could be treated as random noise, and their effect could be minimized by using long time records and power spectra methods. After the first field measurement, it was found that the unidirectionality assumption was wrong. A detailed study of particle motion showed that the microseisms in the period range of 1 to 6 seconds arrived in more than one direction at the same time with comparable strength. One could only find occasional short intervals of 10 - 40 seconds during which microseisms were mostly unidirectional and could be used for phase velocity purposes. It was also found that these relatively short period microseisms were not stationary over time intervals longer than 5 or 10 minutes.

The measured phase velocities of microseisms scattered, and the points did not fall on a smooth curve. Since it was

shown that errors due to the data processing and measurements could be as high as 20 percent of the observed values, this scattering was expected. The reasons for such large errors were the small size of the recording array, instrumental limitations, and digitizing inaccuracies, omitting the interference effects. Using a completely different system with digital recorders and very stable seismometers, these errors may be reduced by an order of magnitude, but the interference effects could not be changed.

A solution to the interference problem is to detect and use the unidirectional wave trains. One method of detection is the use of 3-component seismometers at each, or at least at one, station in the array. The uninterfered Rayleigh wave train is characterized by a linear relation between the two horizontal components of the motion and a 90^{o} phase delay from the horizontal to the vertical component. This means that both horizontal components and the derivative of the vertical component would be zero at the same time. One can then design a system which would test for nulling of the horizontal motion at the same time with the nulling of the derivative of the vertical motion. This system can be used to initiate the recording with a positive test and terminate it with the failing of this test. With this method one would be assured of recording unidirectional and uninterfered Rayleigh wave data.

The use of special arrays may be considered to improve the results. The difficulty of designing an efficient array is that there are two unknown parameters, direction and phase velocity, and without the knowledge of one the other cannot be found. If the velocities were known, then an array could be designed with a strong unidirectional response. Conversely, if there were a known single direction, then the phase velocities could be determined accurately. This difficulty could be avoided to some extent by using "electronically steerable" arrays. At first a phase velocity could be assumed and the azimuth determined. Then the velocity is varied to maximize the response. Using this velocity the direction is improved and another velocity is computed. This procedure of iteration could be continued indefinitely.

The measured phase velocity curves, in spite of the scattering, supply enough information for determining the shallow crustal structures and depths of sedimentary basins. An example of this is the Imperial-1 structure where the basement depth found from gravity interpretations was too deep to be compatible with the observed phase velocities. This depth had to be reduced by 13 percent to obtain a good fit. In conclusion one can say that, with some knowledge of the compressional and the shear velocities in a region, the microseism phase velocity method is potentially as

useful as the gravity method in determining shallow crustal structures. The method of measurement of the phase velocities, however, is more difficult and less suitable for routine work in comparison to the gravity method.

REFERENCES

Aki, K., Crustal structure of Japan from the phase velocity of Rayleigh waves, Bull. Earthquake Res. Inst., (Tokyo), 39, 249-277, 1961.

Alexander, S. S., Surface wave propagation in the Western United States, Ph.D. Thesis, California Institute of Technology, 1963.

Archambeau, C. B., S. S. Alexander, and E. Biehler, Identification and elimination of microseism noise at depth using theoretical Rayleigh wave and observed noise displacement, Report, Contract AF 33(600)-42890, United ElectroDynamics, Inc., Pasadena, California, 1963.

Bath, M., Direction of approach of microseisms, Geophys. J. Roy. Astr. Soc., 6, 450-461, 1962.

Blaik, M., and W. I. Donn, Microseism ground motion at Palisades and Weston, Bull. Seism. Soc. Am., 44, 597-612, 1954.

Darbyshire, J., Structure of microseismic waves; estimation of direction of approach by comparison of vertical and horizontal components, Proc. Roy. Soc. London A, 223, 96-111, 1954.

Davenport, W. B., Jr., and W. L. Root, An introduction to the theory of random signals and noise, McGraw-Hill Book Company, Inc., New York, 1958.

Deacon, G. E. R., Sea waves and microseisms, Brit. Assoc. Advance. of Sci., 11, 356-357, 1954.

de Rossi, M. S., Primi resultati delle osservazioni in Roma e Rocca di Papa sulle oscillazioni microscopiche dei pendoli, Atti. Acad. Pontifica, 38, 168, 1874.

Dinger, J. E., Method for increasing accuracy of bearings obtained by tripartite microseismic station, Earthquake Notes, 22, 27-28, 1951.

Donn, W. L., Direction studies using microseisms ground particle motion, Trans. Am. Geophys. Union, 35, 8-21, 1954.

Gutenberg, B., Microseisms, Advances in Geophysics, 5, Academic Press , Inc., New York, 1958.

Gutenberg, B., and F. Andrews, Bibliography on microseisms, Second edition, Scientific Report No. 1, Contract AF (122)436, California Institute of Technology, Seismological Laboratory, 1952.

Gutenberg, B., and F. Andrews, Bibliography on microseisms, Part 2, Second edition, Scientific Report No. 2, Contract AF 19(122)436, California Institute of Technology, Seismological Laboratory, 1956.

Haubrich, R. A., and H. M. Iyer, A digital seismograph system for measuring earth noise, Bull. Seism. Soc. Am., 52, 87-93, 1962.

Haubrich, R. A., W. H. Munk, and F. E. Snodgrass, Comparative spectra of microseisms and swell, Bull. Seism. Soc. Am., 53, 27-37, 1963.

Heiland, C. A., Geophysical exploration, Prentice-Hall, Inc., New York, 1940.

Iyer, H. M., World-wide microseismic study, Nature, 194, 1031-1033, 1962.

Jensen, H., A procedure for determination of direction of approach of microseismic waves, Medd. Geod. Inst. Kobenhavn, 36, 18 p., 1958.

Kishinouye, F., and R. Ikegami, A study of microseisms after A. W. Lee's method, Bull. Earthquake Res. Inst., (Tokyo), 25, 43-48, 1947.

Kovach, R. L., Geophysical investigations in the Colorado Delta region, Ph.D. Thesis, California Institute of Technology, 1962.

Laning, J. H., Jr., and R. H. Battin, Random processes in automatic control, McGraw-Hill Book Company, Inc., New York, 1956.

Leet, L. D., Microseisms, Sci. Am., 180, 42-45, 1949.

Leet, L. D., Earth waves, Harvard University Press and John Wiley and Sons, New York, 1950.

Lynch, J. J., Fordham's new tripartite station at Poughkeepsie, Earthquake Notes, 22, 6-7, 1951.

Mukherjee, S. M., On microseisms recorded in India and Ceylon, Indian Meteor. Dept. Scientific Notes, 10, 41-49, 1948.

Okano, K., Observational study on microseisms, Part 1, Bull. Disaster Prev. Res. Inst., Kyoto Univ., 44, 1961.

Okano, K., Observational study on microseisms, Part 2, Bull. Disaster Prev. Res. Inst., Kyoto Univ., 47, 1961.

Oliver, J., and R. Page, Concurrent storms of long and ultralong period microseisms, Bull. Seism. Soc. Am., 53, 15-26, 1963.

Page, C. H., Instantaneous power spectra, J. Appl. Phys., 23, 103-106, 1952.

Ramirez, J. E., An experimental investigation of the nature and origin of microseisms at St. Louis, Missouri, Bull. Seism. Soc. Am., 30, 35-84, 139-178, 1940.

Ramirez, J. E., Tripartite stations and direction of approach of microseisms, Symposium on Microseisms, Sept. 9-19, 1952, Nat'l. Acad. Sci., Nat'l Res. Council, 1953.

Rykunov, L. N., Correlation method of study of microseisms, Bull. (Izv.) Acad. Sciences USSR, 1037-1039, 1961.

Rykunov, L. N., and S. V. Mishin, Some features of microseism propagation along continental paths, Bull (Izv.) Acad. Sciences USSR, Geophys. Ser., 529-533, 1961.

Silverman, R. A., Locally stationary random processes, IRE, Trans. on Infor. Theory, IT-3, 182-187, 1957.

Spieker, L. J., (Project manager), Seismometer array and data processing system, Final report, Phase 1, Contract Af 33(600)41840, Texas Instruments, Inc., Dallas, Texas, 1961.

Toksöz, M. N., and A. Ben-Menahem, Velocities of mantle Love and Rayleigh waves over multiple paths, Bull. Seism. Soc. Am., 53, (in press), 1963.

Wilson, E. B., Jr., An introduction to Scientific Research, McGraw-Hill, New York, 1952.

Wilson, J. T., A statistical study of the periods and amplitudes of microseisms, Trans. Am. Geophys. Union, Part II, 228-231, 1942.

Young, H. D., Statistical treatment of experimental data, McGraw-Hill Book Company, Inc., New York, 1962.

Zbur, R., A geophysical investigation of Indian Wells Valley, California, M. S. Thesis, Univ. of Utah, 1962.

LIST OF TABLES

TABLE 1

Comparison of Phase Velocity and Gravity Results

at Imperial-1

Gravity

Layer Thickness km	Depth to Bottom km	Density gr/cm³
1.9	1.9	2.3
1.8	3.7	2.55
∞	∞	2.67

Imperial-1A Model

Thickness d(km)	Depth h(km)	Density g/cm³	Comp. Vel. km/sec	Poisson's Ratio	Shear Vel. km/sec
0.7	0.7	2.1	1.75	0.40	0.72
1.2	1.9	2.3	2.32	0.37	1.05
0.3	2.2	2.3	2.62	0.33	1.32
1.5	3.7	2.55	3.80	0.31	2.00
∞	∞	2.67	5.54	0.27	3.11

Imperial-1G Best Fit Model

Thickness d(km)	Depth h(km)	Density g/cm³	Comp. Vel. km/sec	Poisson's Ratio	Shear Vel. km/sec
0.5	0.5	2.10	1.70	0.40	0.70
0.30	0.8	2.1	1.80	0.40	0.75
0.4	1.2	2.3	2.40	0.33	1.20
0.5	1.7	2.3	2.80	0.33	1.40
0.7	2.4	2.50	3.80	0.30	2.05
0.8	3.2	2.50	4.10	0.30	2.20
∞	∞	2.67	5.90	0.27	3.30

TABLE 2

Comparison of Phase Velocity and Refraction Results at Imperial-2

Refraction

Thickness (km)	Depth to Bottom (km)	Compressional Velocity km/sec
0.45	0.45	1.75
0.97	1.42	2.32
0.26	1.68	2.62
1.40	3.08	3.80
∞	∞	5.54

Phase Velocity Best Fit Model

Thickness. d(km)	Depth h(km)	Density g/cm^3	Comp. Vel. km/sec	Poisson's Ratio	Shear Vel. km/sec
0.45	0.45	2.10	1.75	0.40	0.72
0.97	1.42	2.30	2.32	0.37	1.05
0.26	1.68	2.30	2.62	0.33	1.32
1.40	3.08	2.55	3.80	0.31	2.00
∞	∞	2.67	5.54	0.27	3.11

FIGURE CAPTIONS

Figure 1. The autocovariance functions of microseisms at different time intervals. Covariances were computed using 2 minute records sampled at 0.2 second intervals.

Figure 2. Coherence of microseisms recorded simultaneously at four different distances.

Figure 3. Particle motion of microseisms which are fairly unidirectional. (a) and (b) are plots of N-S versus E-W and Z versus N-S components at two different times. (c) shows an excellent retrograde elliptic motion.

Figure 4. Particle motion from interfering microseisms.

Figure 5. (a) and (b) are the plots of the horizontal motion of microseism particle motion showing the rapid changes in the direction of approach.

Figure 6. Polarization of the P and the SH motion from a small tremor. The directions marked as N and E correspond to N 30°E and S 60°E, respectively.

Figure 7. Block diagram of the 8-channel microseism recording system.

Figure 8. The recording system amplitude response to ground displacement.

Figure 19. Fourier amplitude and phase spectra of a segment of Imperial-1 microseism.

Figure 20. The microseism phase velocities measured from four different recordings at Imperial-1. The theoretical Rayleigh wave curves are for 1-A and the best fit 1-G models.

Figure 21. Microseism phase velocities and theoretical curve for the best fitting model at Imperial-2. The vertical bars plotted with the points are standard deviations.

Figure 22. Plot of phase difference $\xi_\varphi = \bar{\varphi} - \varphi$ versus X/λ for interfering waves for r = 0.2.

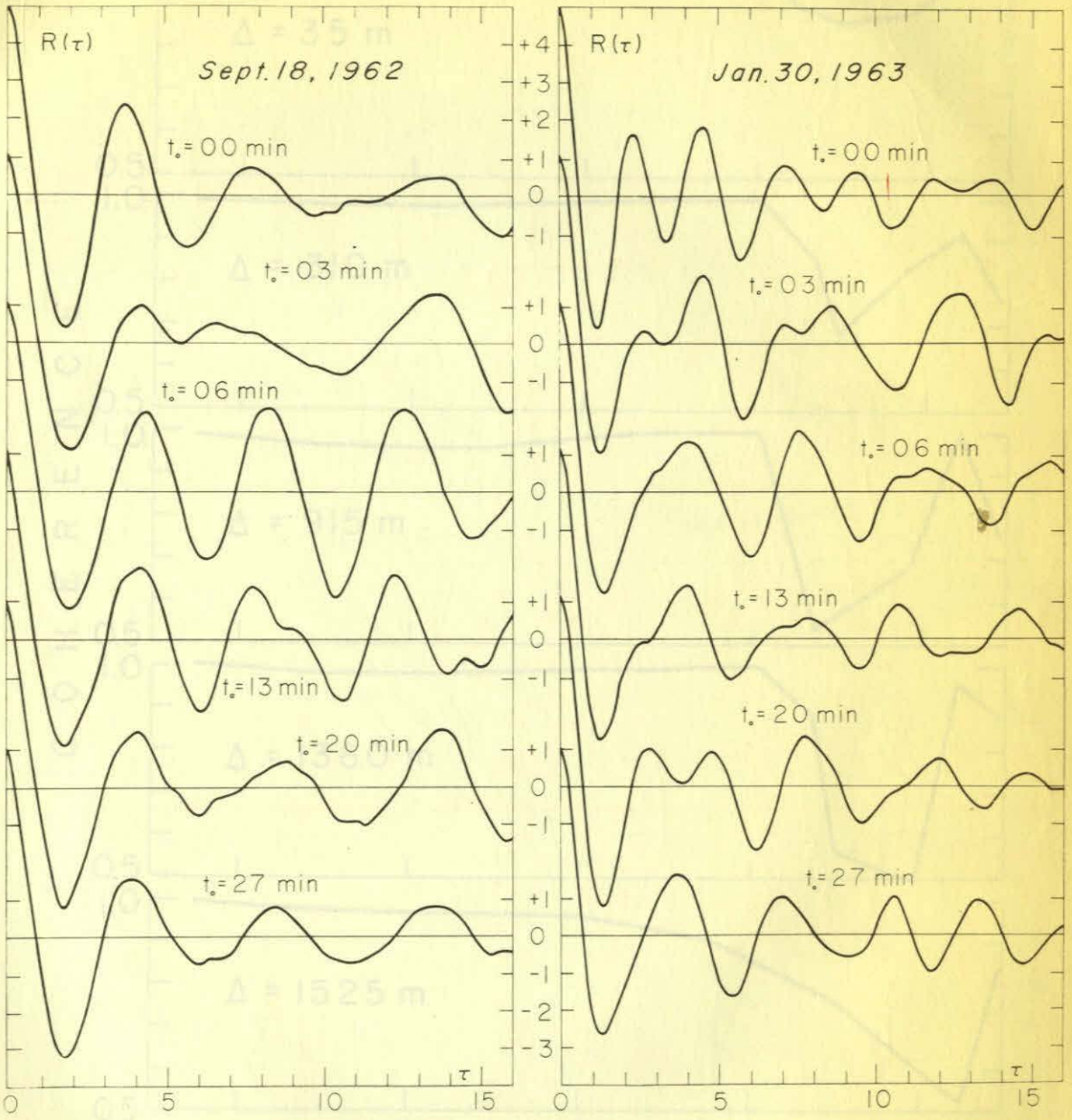
R(τ)
Sept. 18, 1962
t₀ = 00 min
t₀ = 03 min
t₀ = 06 min
t₀ = 13 min
t₀ = 20 min
t₀ = 27 min
+4
+3
+2
+1
0
-1
-2
-3
0
5
10
15
τ
R(τ)
Jan. 30, 1963
t₀ = 00 min
t₀ = 03 min
t₀ = 06 min
t₀ = 13 min
t₀ = 20 min
t₀ = 27 min
0
5
10
15
τ

Fig. 1

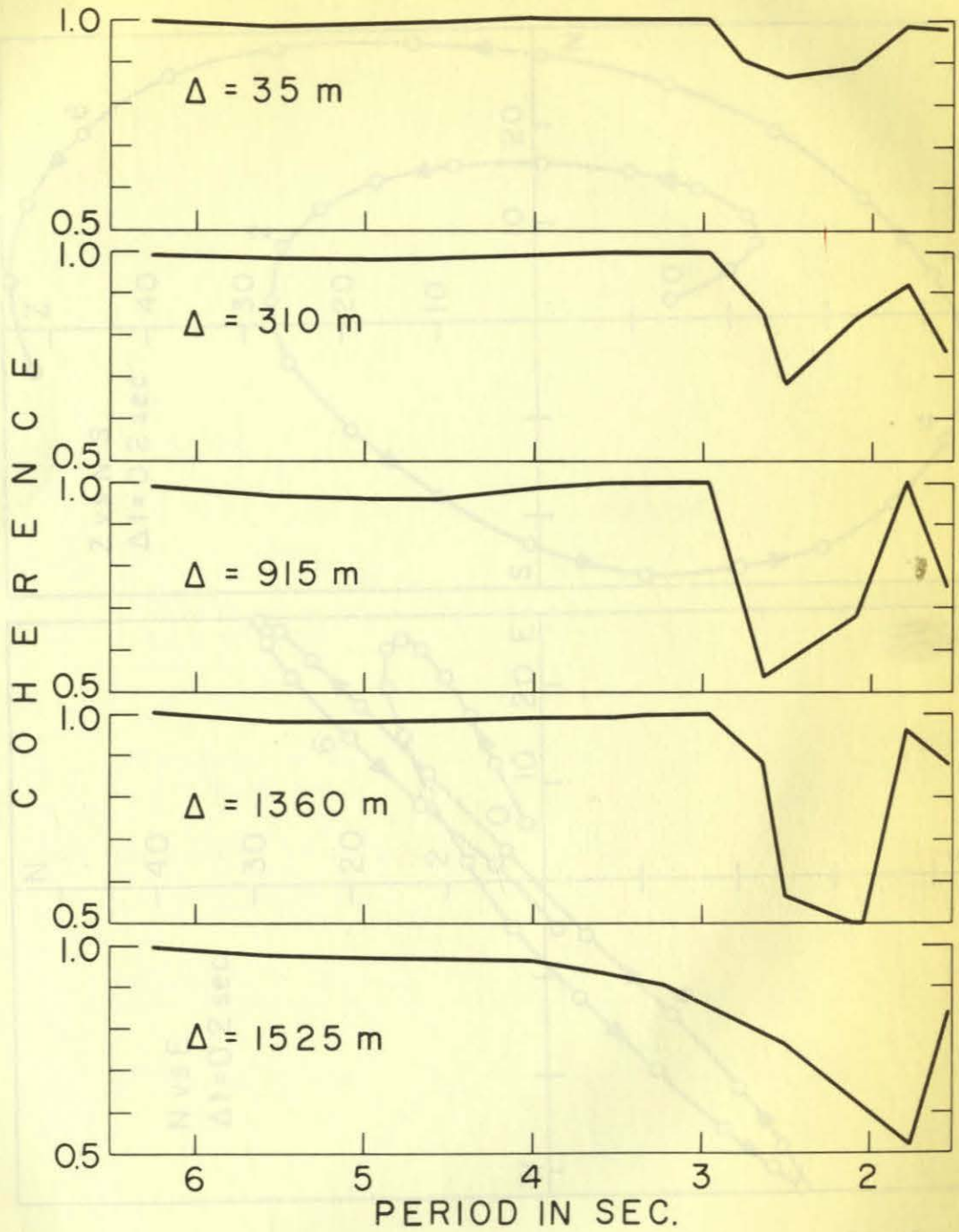
1.0
Δ = 35 m
0.5
1.0
Δ = 310 m
0.5
1.0
Δ = 915 m
0.5
1.0
Δ = 1360 m
0.5
1.0
Δ = 1525 m
0.5
COHERENCE
6
5
4
3
2
PERIOD IN SEC.

Fig. 2

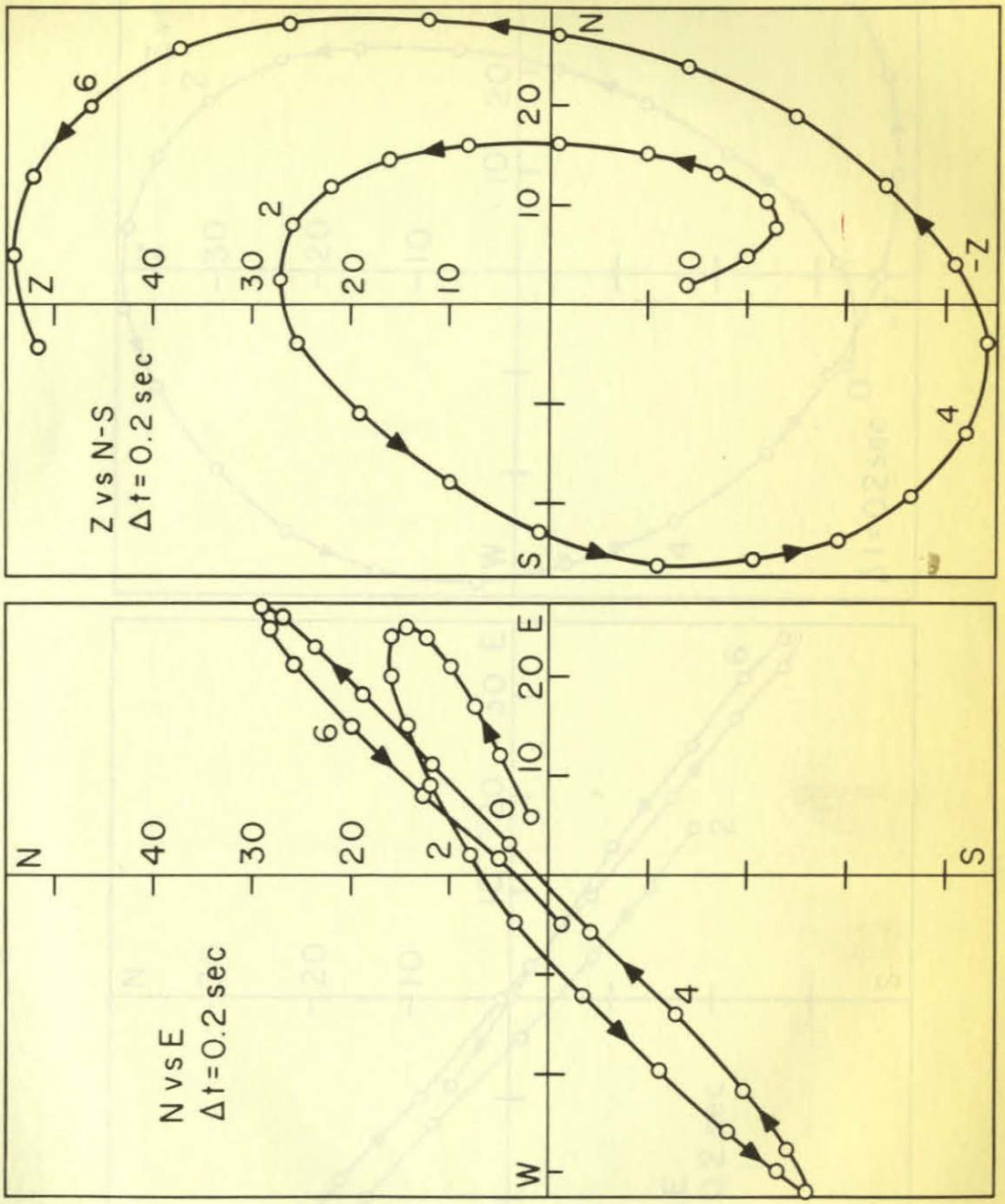

Fig. 3(a)

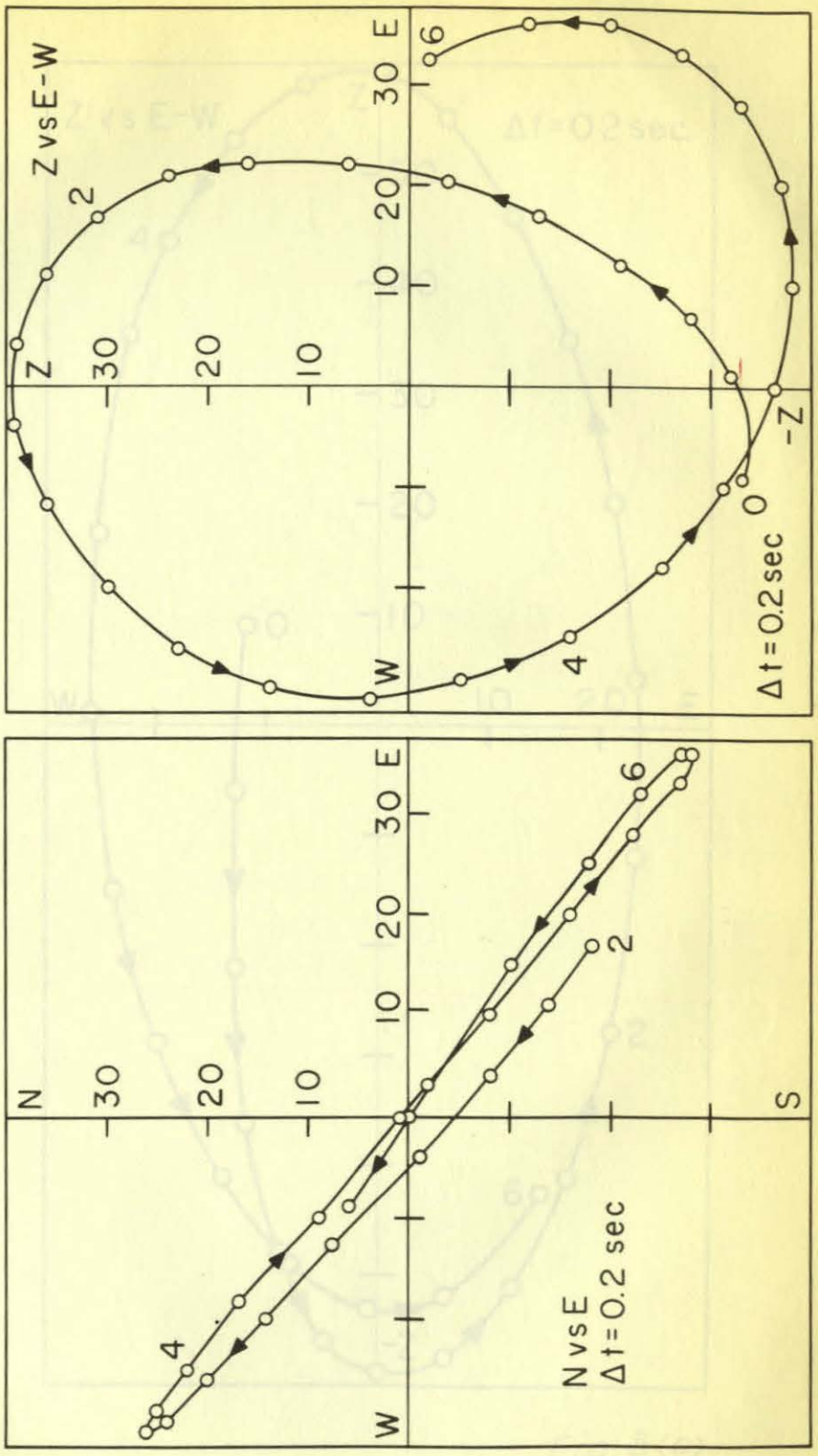
Z vs E-W
Z
30
20
10
2
W
30 E
20
10
4
6
-Z
0
Δt = 0.2 sec
N vs E
Δt = 0.2 sec
N
S
W
30 E
30
20
10
20
10
2
4
6

Fig. 3(b)

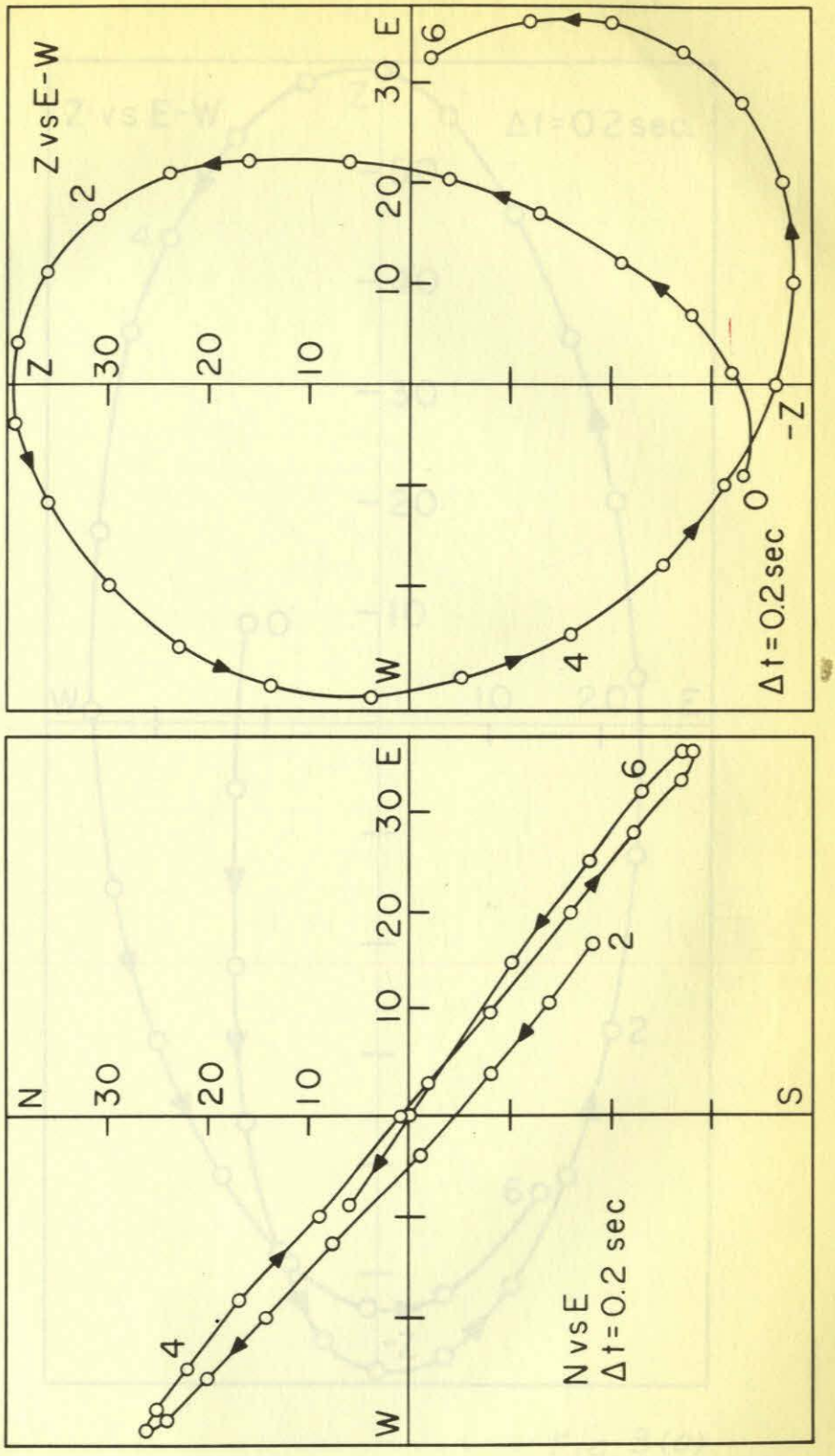

Fig. 3(b)

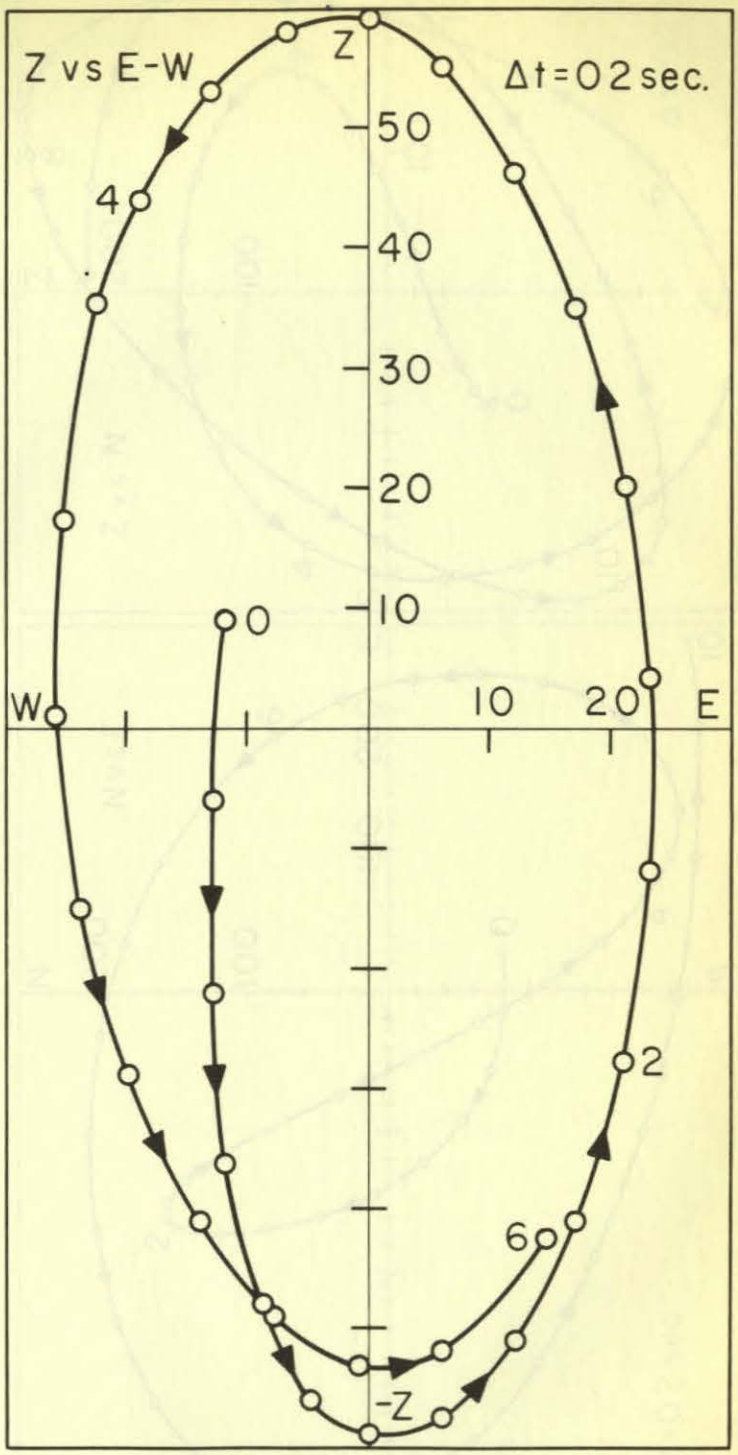

Fig. 3(c)

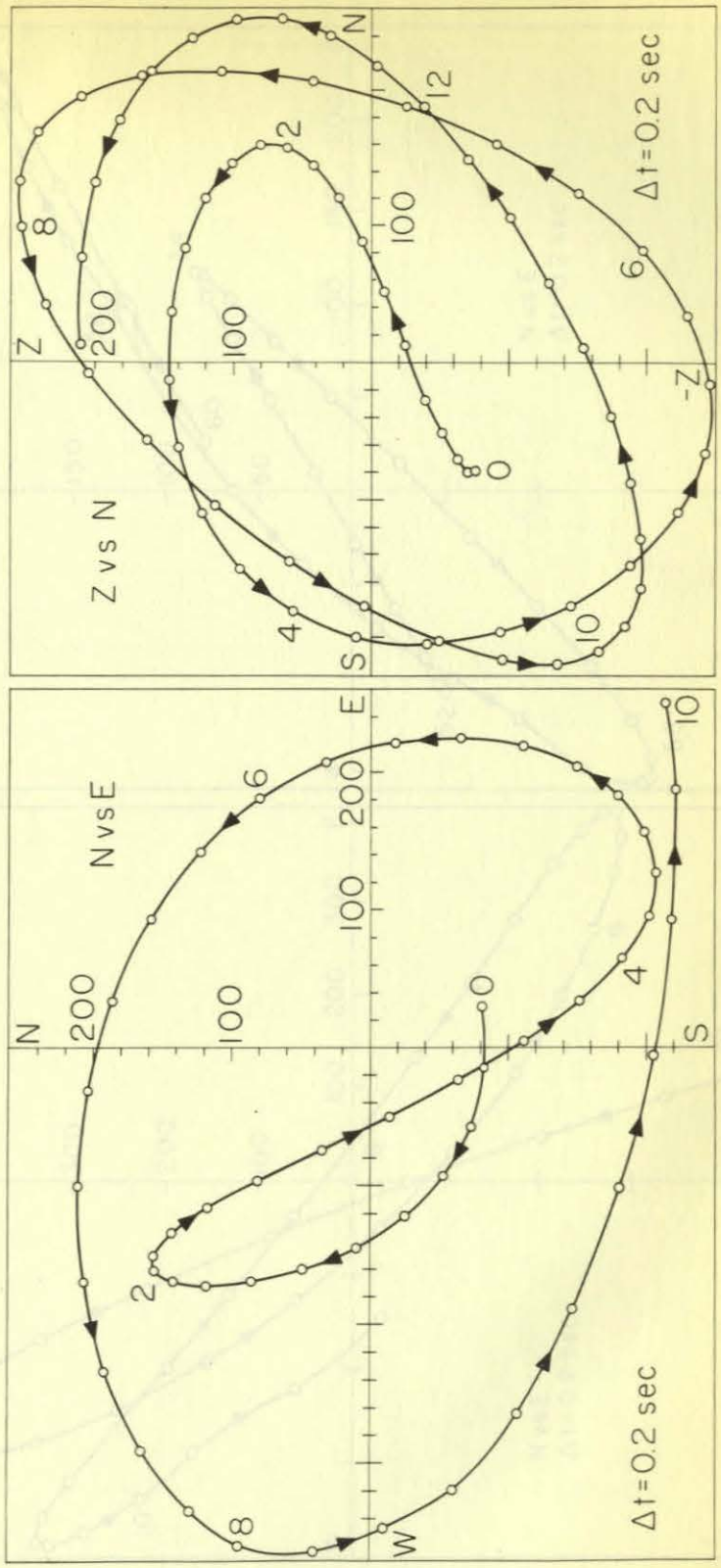

Fig. 4

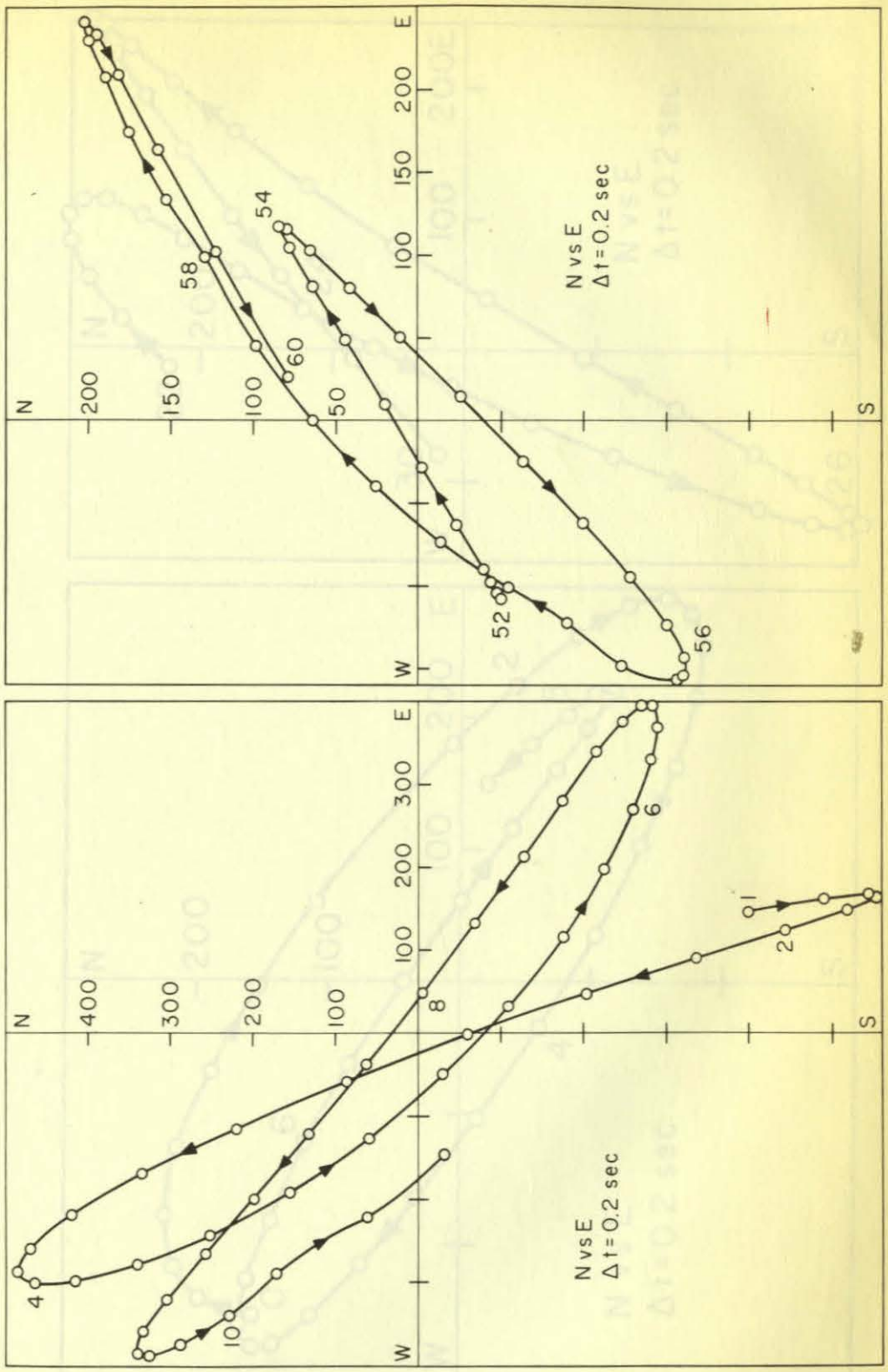
N vs E
Δt = 0.2 sec
N
S
W
E
-200
-150
-100
-50
100
150
200
52
54
56
58
60
N vs E
Δt = 0.2 sec
N
S
W
E
-400
-300
-200
-100
100
200
300
1
2
4
6
8
10

Fig. 5(a)

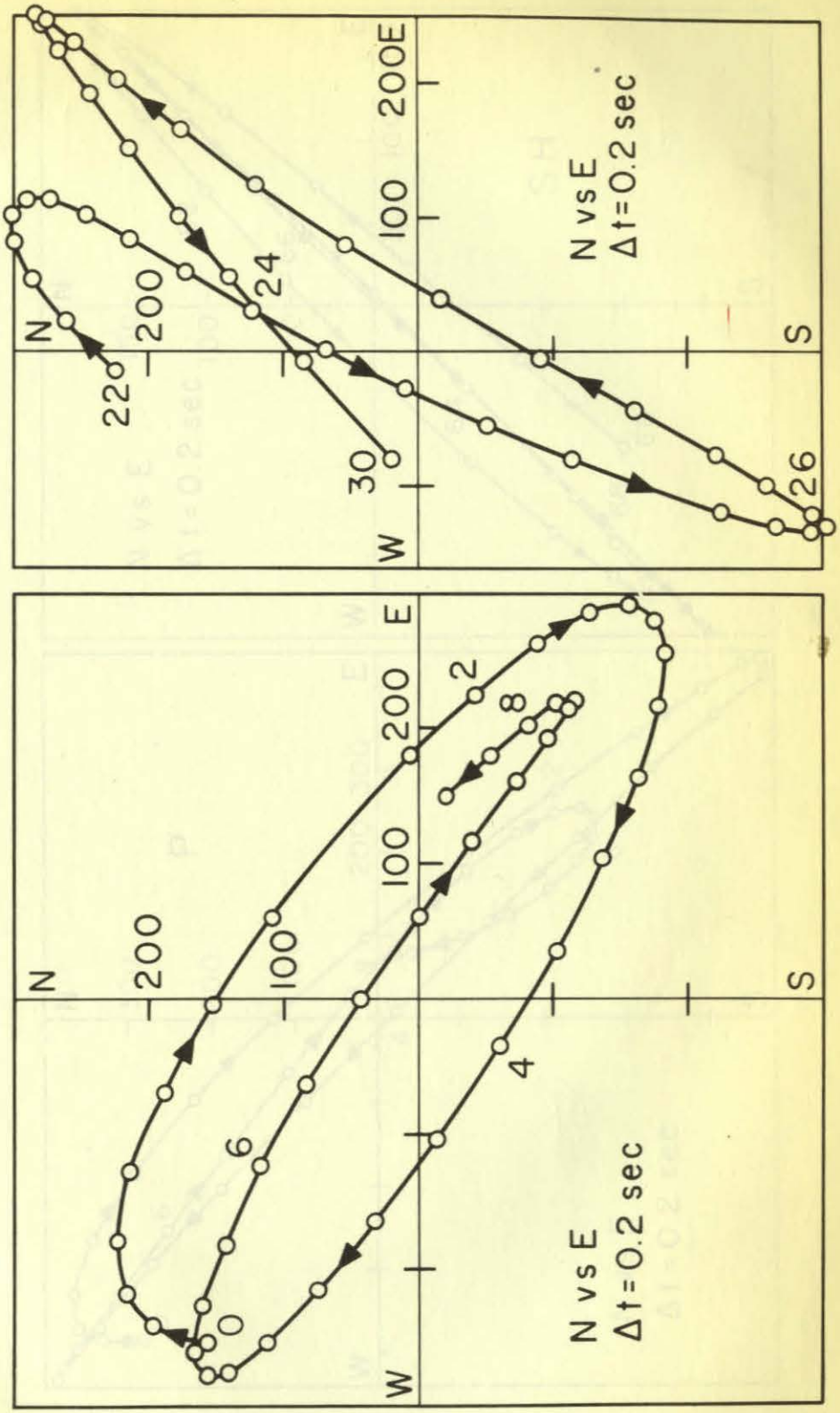
N
S
W
E
200
100
200
N vs E
Δt=0.2 sec
0
2
4
6
8
N
S
W
200E
100
200
22
24
26
30
N vs E
Δt=0.2 sec

Fig. 5(b)

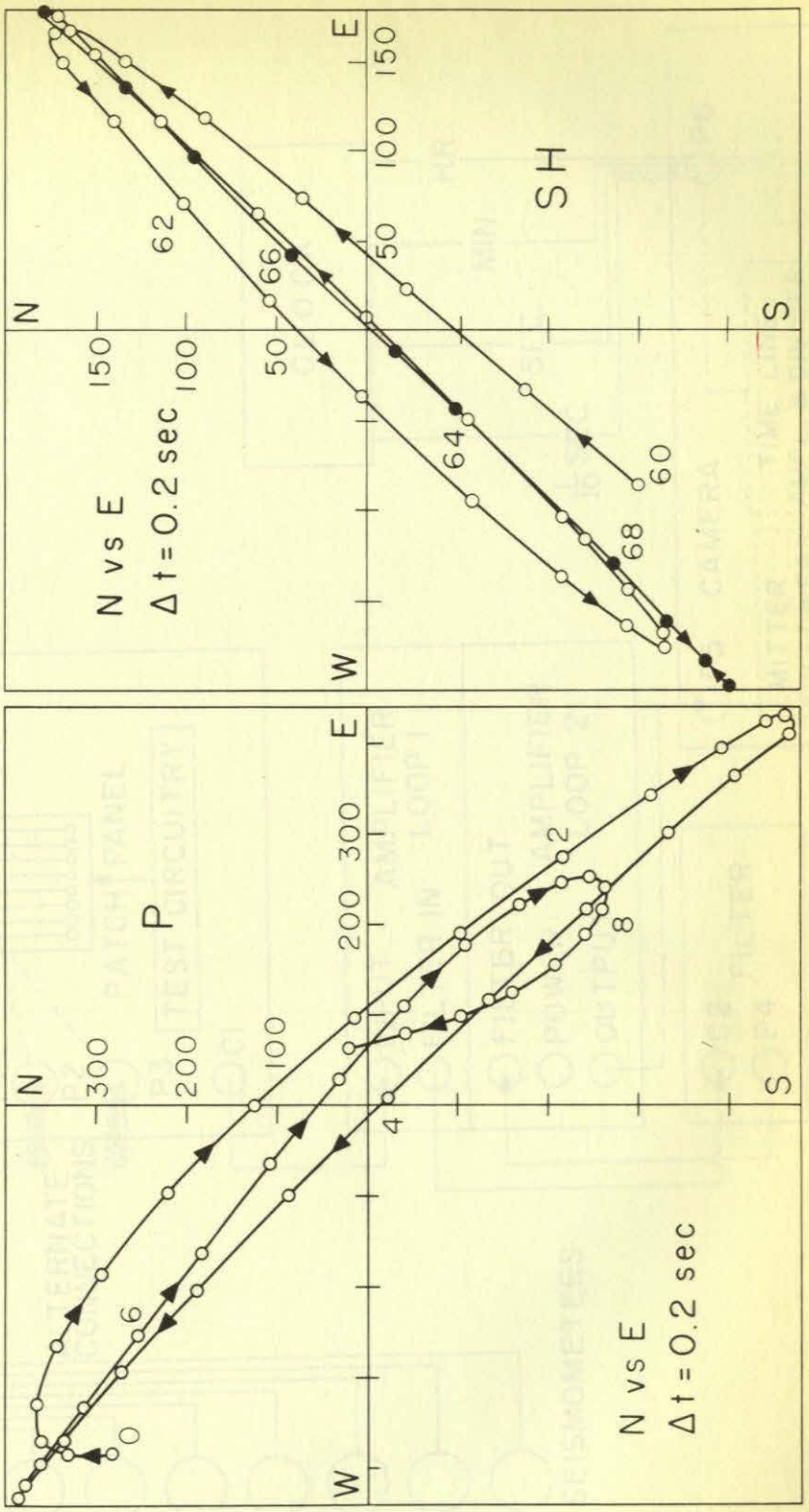
N vs E
Δ t = 0.2 sec
N
S
W
E
150
100
50
62
66
64
60
68
SH
P
300
200
100
200 300
0
6
4
2
8
N vs E
Δ t = 0.2 sec

Fig. 6

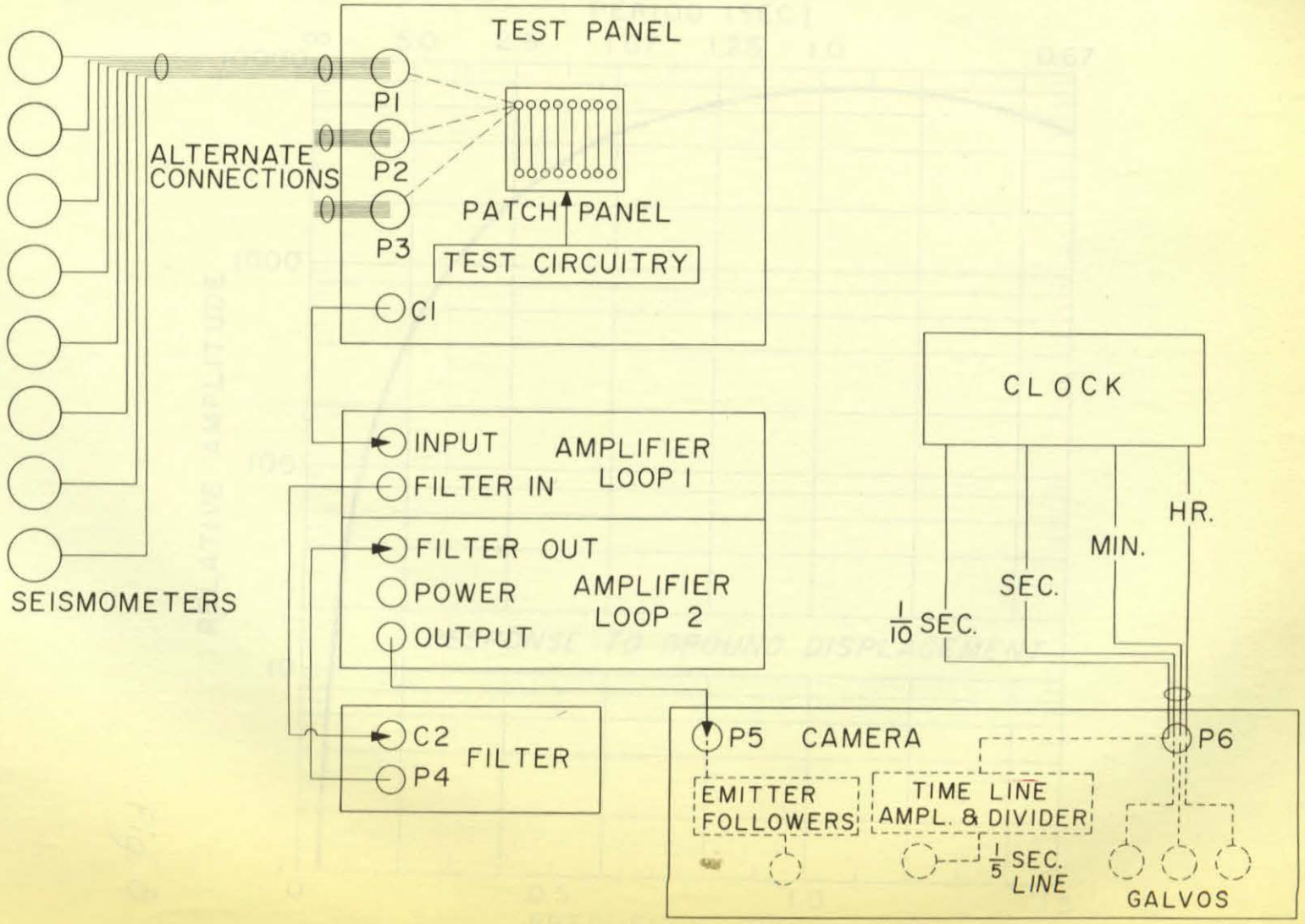
TEST PANEL
P1
P2
P3
ALTERNATE CONNECTIONS
PATCH PANEL
TEST CIRCUITRY
C1
SEISMOMETERS
INPUT
FILTER IN
AMPLIFIER LOOP 1
FILTER OUT
POWER
OUTPUT
AMPLIFIER LOOP 2
C2
P4
FILTER
CLOCK
HR.
MIN.
SEC.
1/10 SEC.
P5
CAMERA
P6
EMITTER FOLLOWERS
TIME LINE AMPL. & DIVIDER
1/5 SEC. LINE
GALVOS

Fig. 7

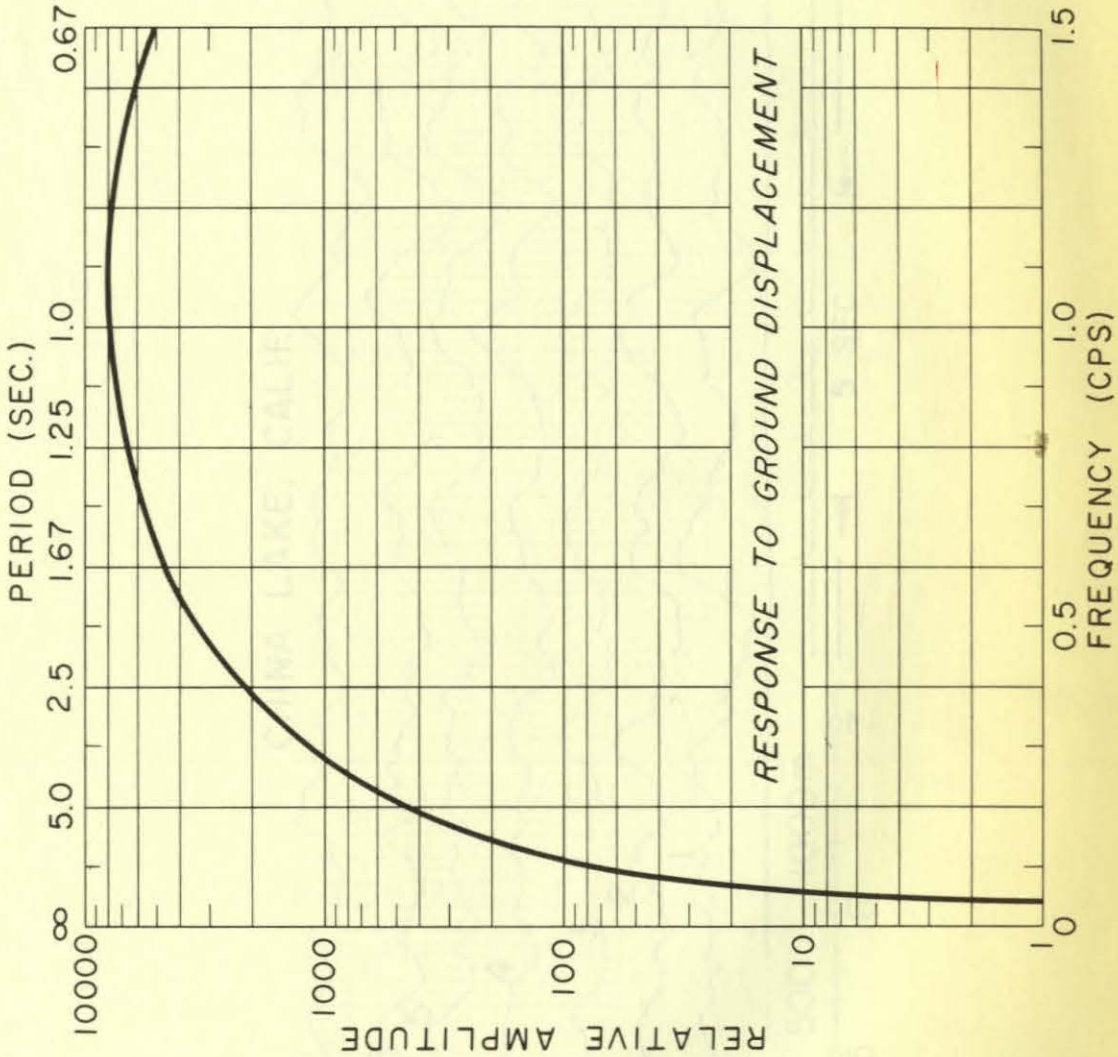
RESPONSE TO GROUND DISPLACEMENT
RELATIVE AMPLITUDE
10000
1000
100
10
1
PERIOD (SEC.)
∞
5.0
2.5
1.67
1.25
1.0
0.67
FREQUENCY (CPS)
0
0.5
1.0
1.5

Fig. 8

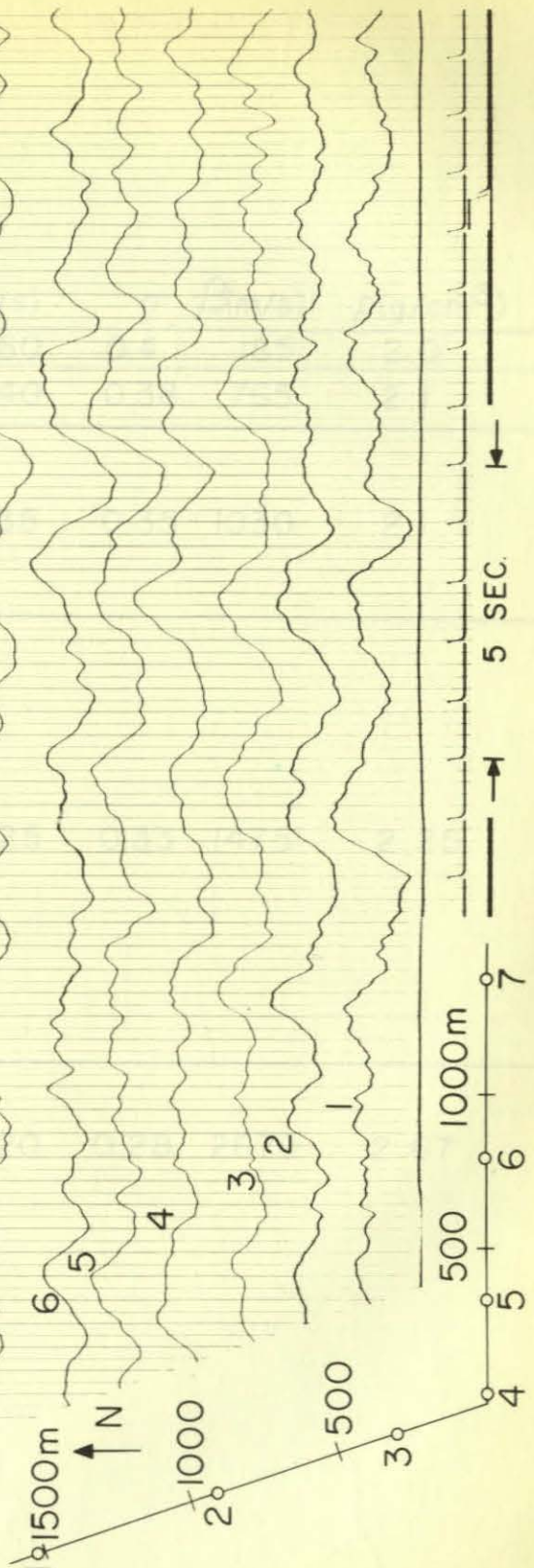
CHINA LAKE, CALIF.
7
6
5
4
3
2
1
1500m
1000
500
N
1
2
3
4
5
6
7
500
1000m
5 SEC.

Fig. 9

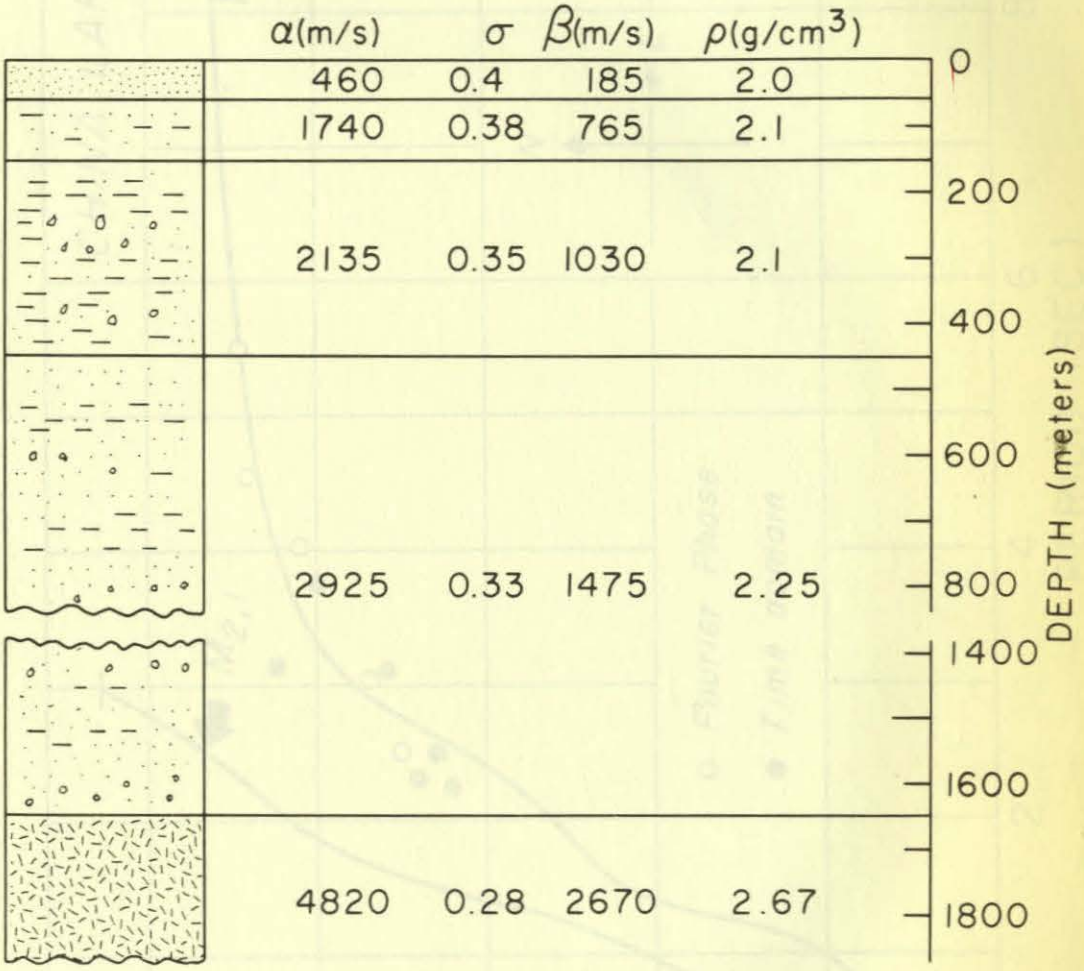
α(m/s)
σ
β(m/s)
ρ(g/cm³)
460
0.4
185
2.0
1740
0.38
765
2.1
2135
0.35
1030
2.1
2925
0.33
1475
2.25
4820
0.28
2670
2.67
0
200
400
600
800
1400
1600
1800
DEPTH (meters)

Fig. 10

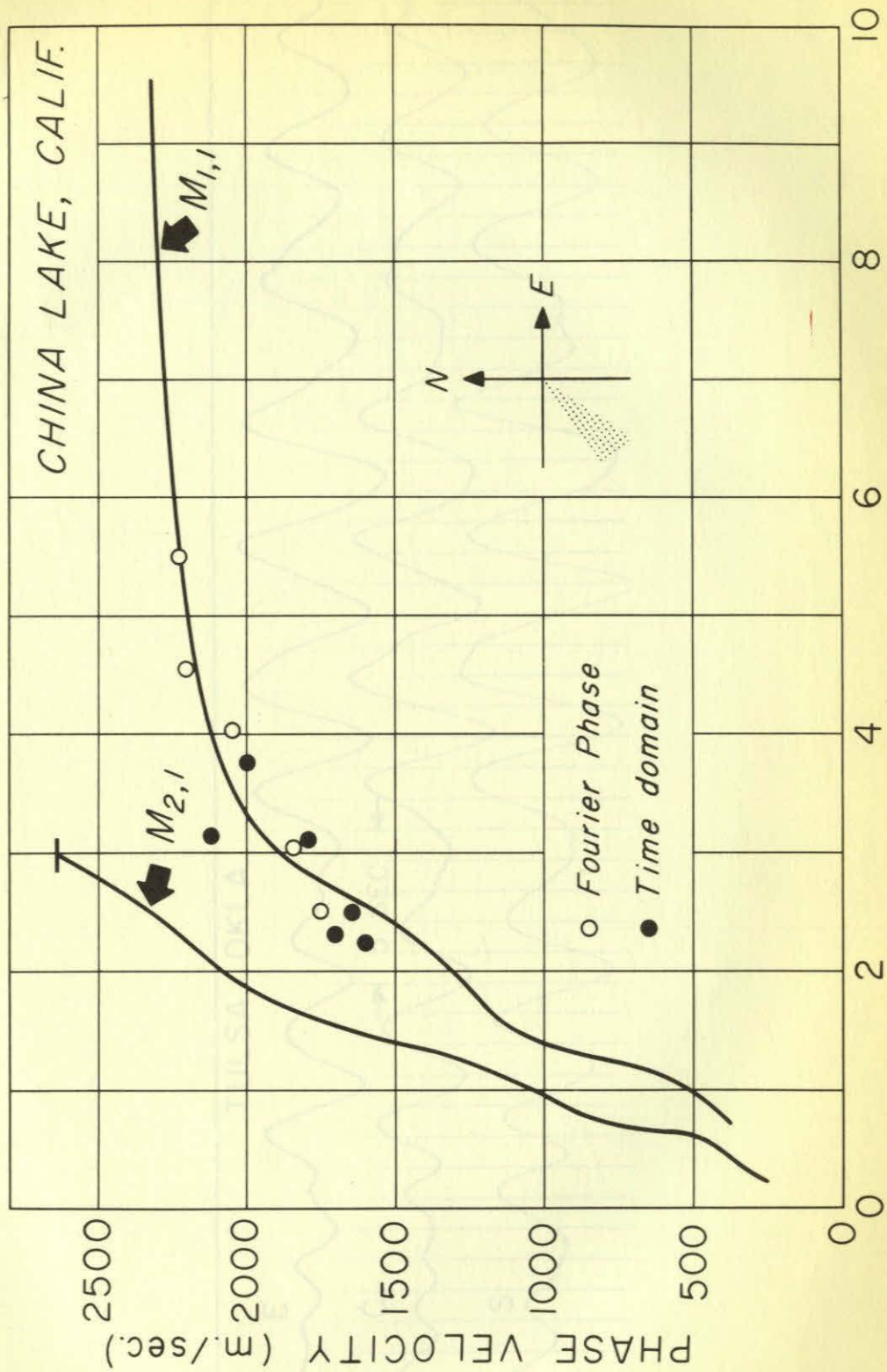
CHINA LAKE, CALIF.
$M_{1,1}$
$M_{2,1}$
N
E
o Fourier Phase
• Time domain
PHASE VELOCITY (m./sec.)
2500
2000
1500
1000
500
0
0
2
4
6
8
10
PERIOD (SEC.)

Fig. 11

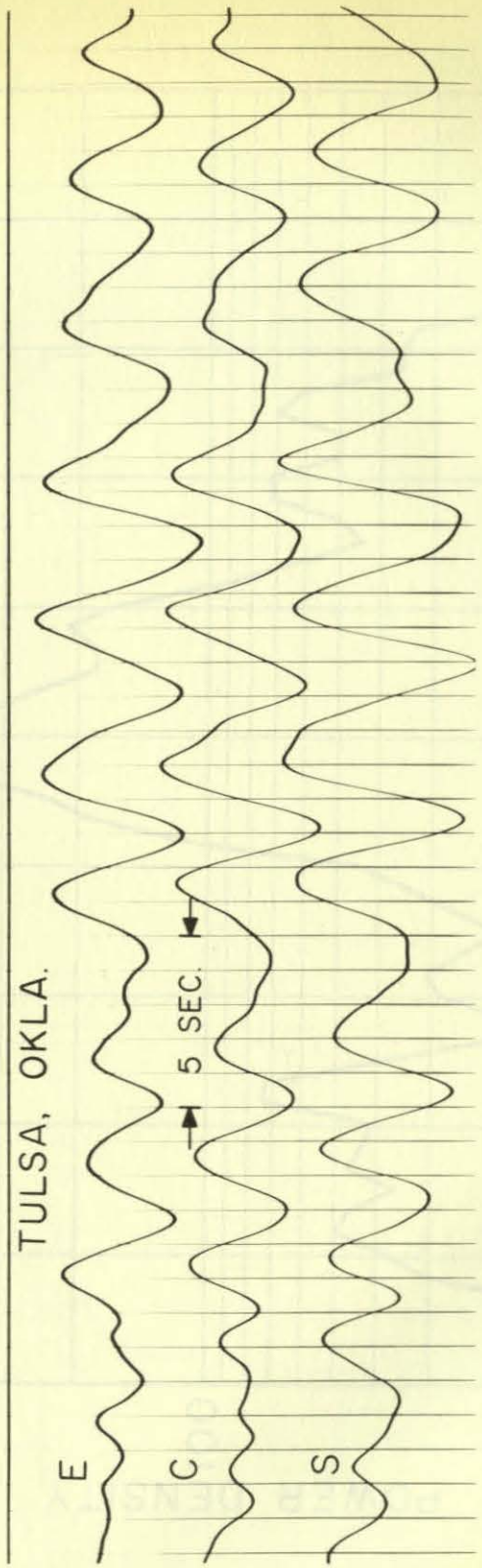

Fig. 12

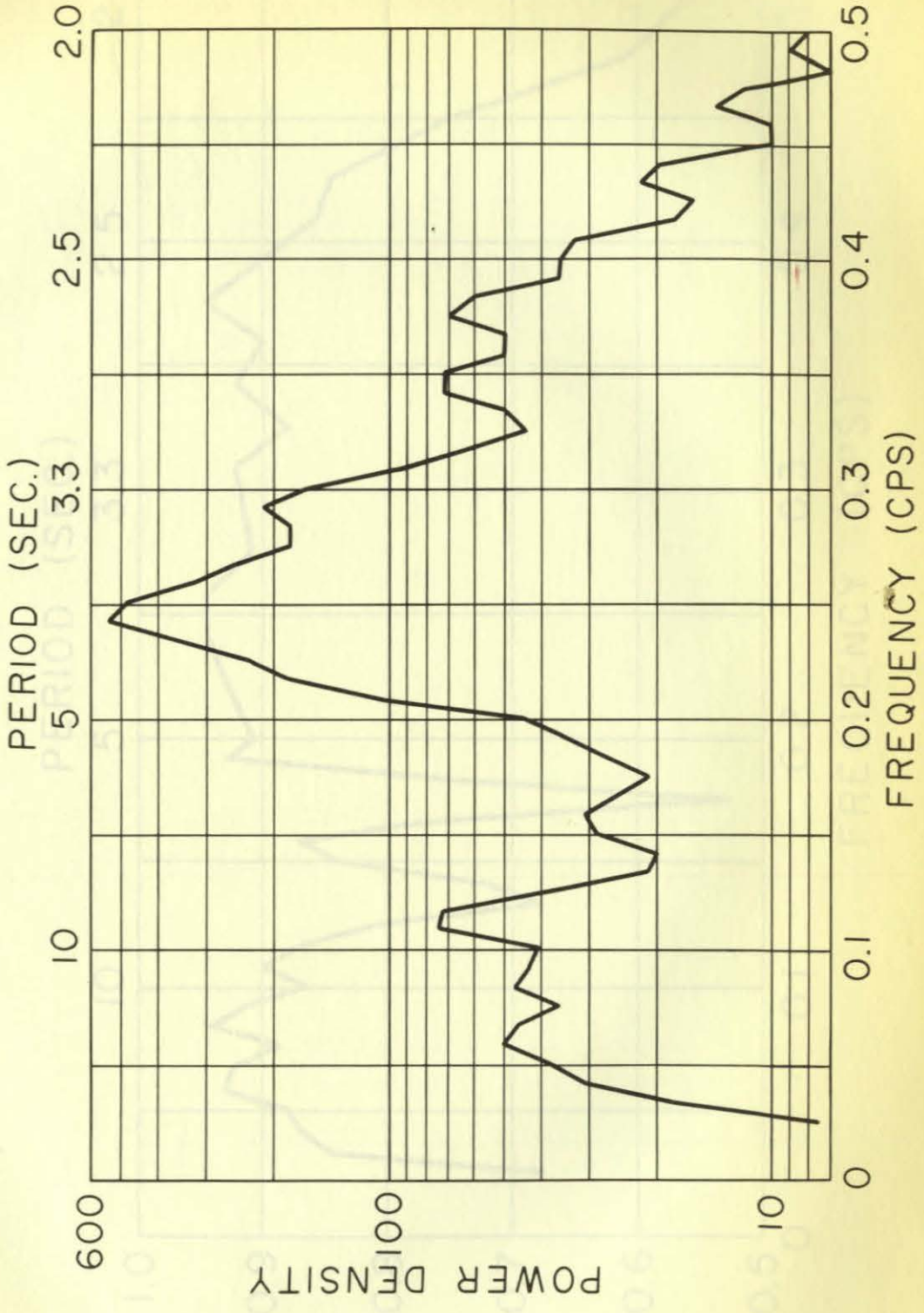
PERIOD (SEC.)
2.0
2.5
3.3
5
10
FREQUENCY (CPS)
0.5
0.4
0.3
0.2
0.1
0
POWER DENSITY
600
100
10

Fig. 13

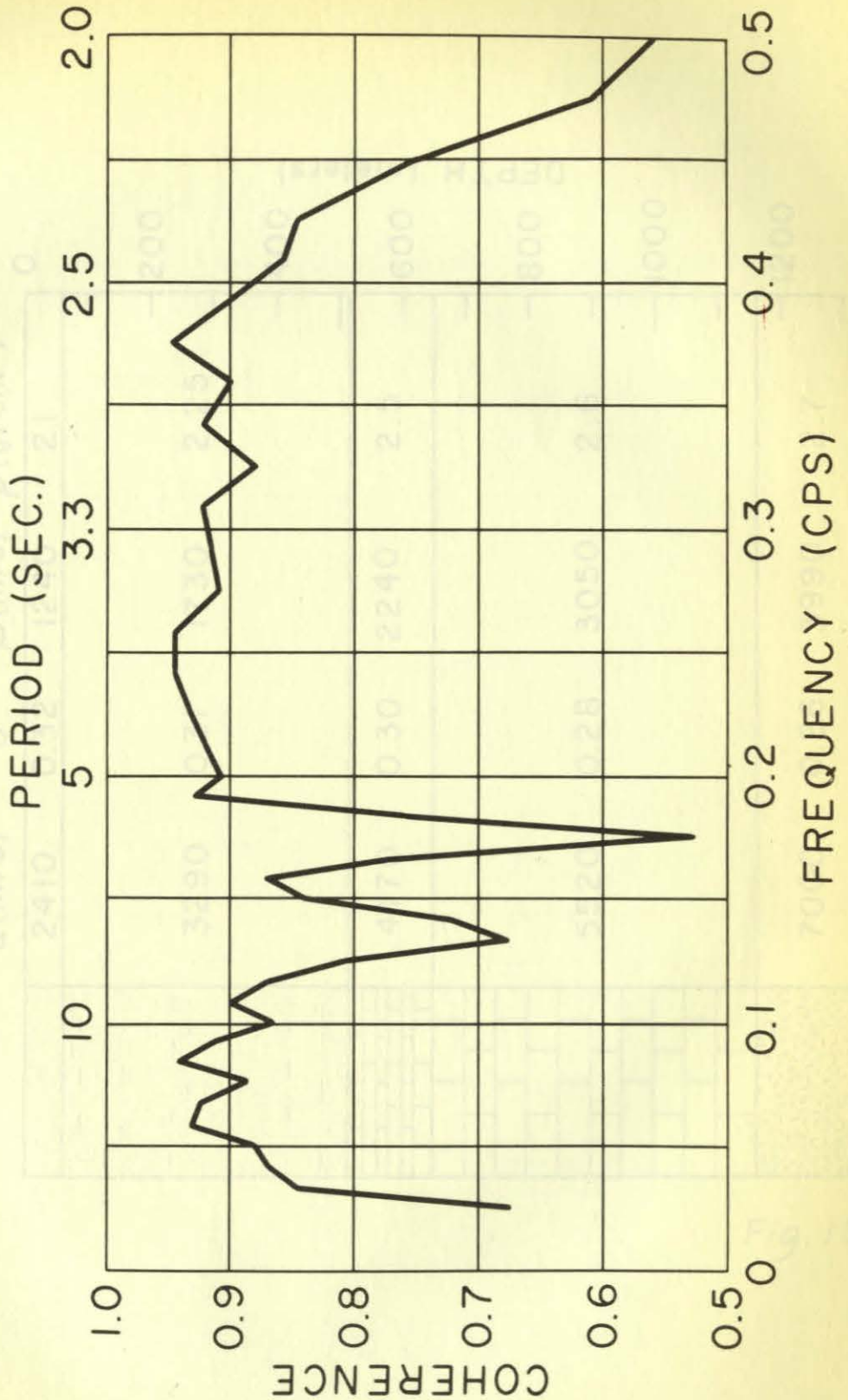
PERIOD (SEC.)
2.0
2.5
3.3
5
10
FREQUENCY (CPS)
0.5
0.4
0.3
0.2
0.1
0
COHERENCE
1.0
0.9
0.8
0.7
0.6
0.5

Fig. 14

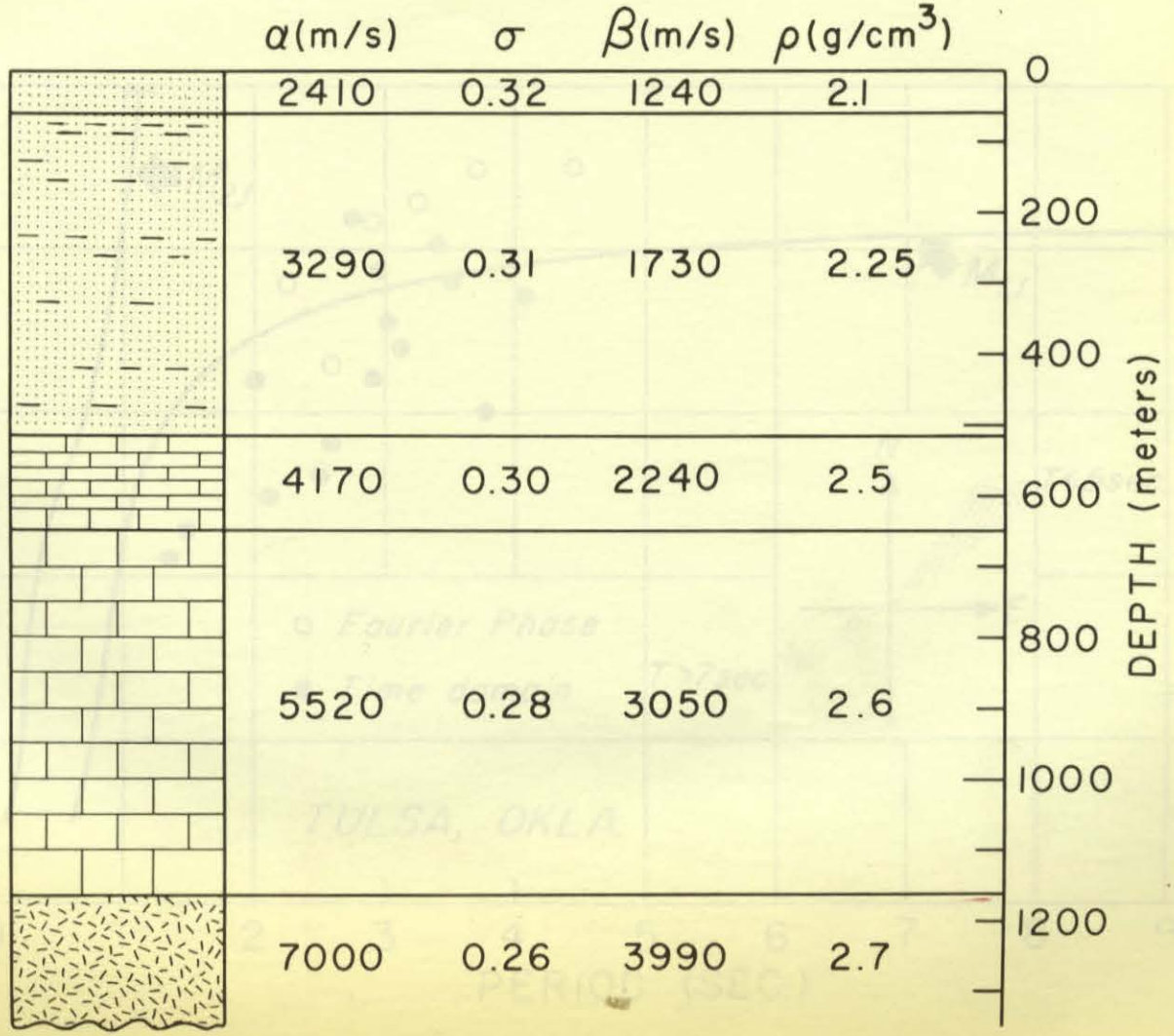
α(m/s)
σ
β(m/s)
ρ(g/cm³)
2410
0.32
1240
2.1
3290
0.31
1730
2.25
4170
0.30
2240
2.5
5520
0.28
3050
2.6
7000
0.26
3990
2.7
0
200
400
600
800
1000
1200
DEPTH (meters)

Fig. 15

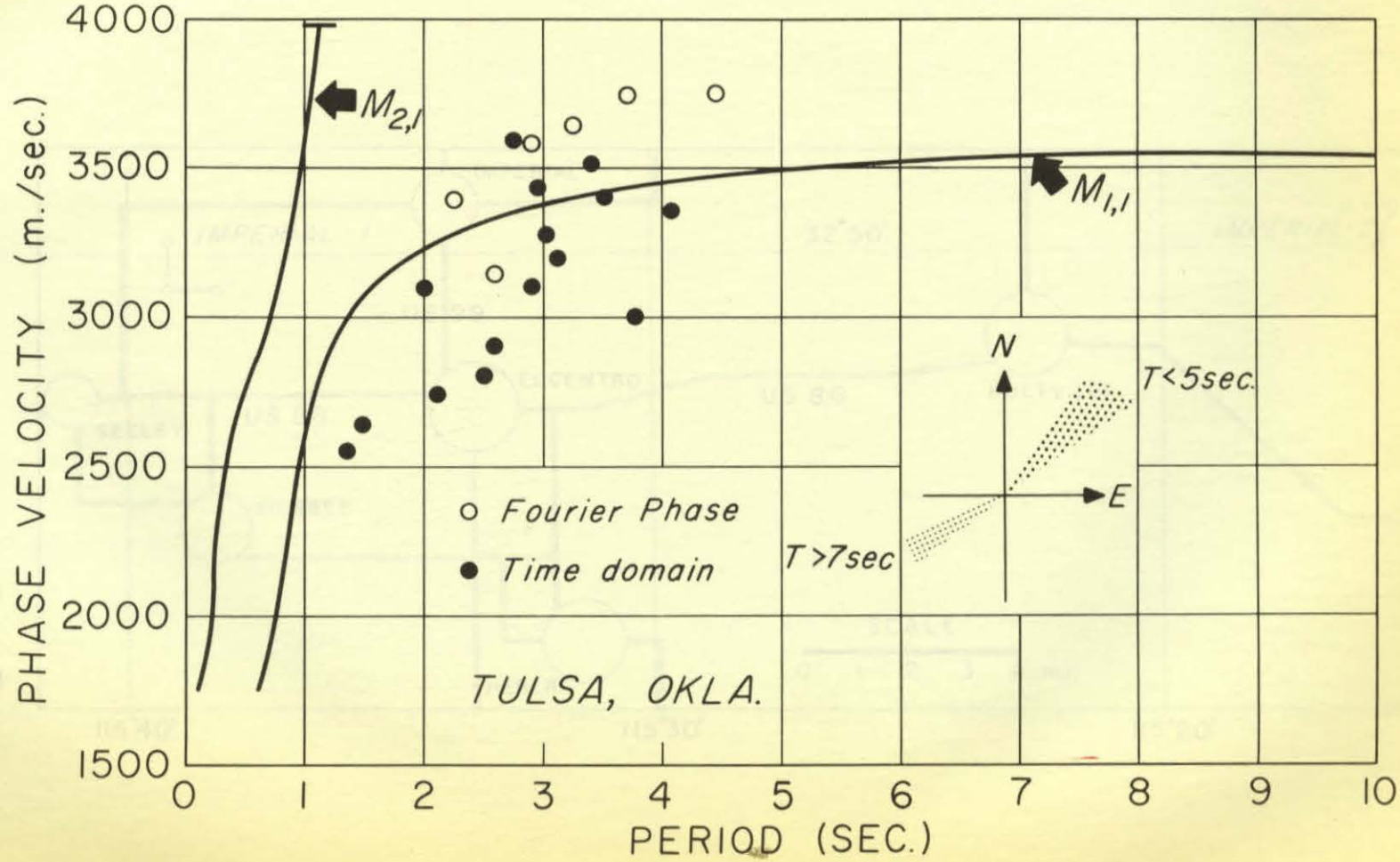
4000
3500
3000
2500
2000
1500
PHASE VELOCITY (m./sec.)
0
1
2
3
4
5
6
7
8
9
10
PERIOD (SEC.)
$M_{2,1}$
$M_{1,1}$
Fourier Phase
Time domain
TULSA, OKLA.
N
E
T<5sec.
T>7sec

Fig. 16

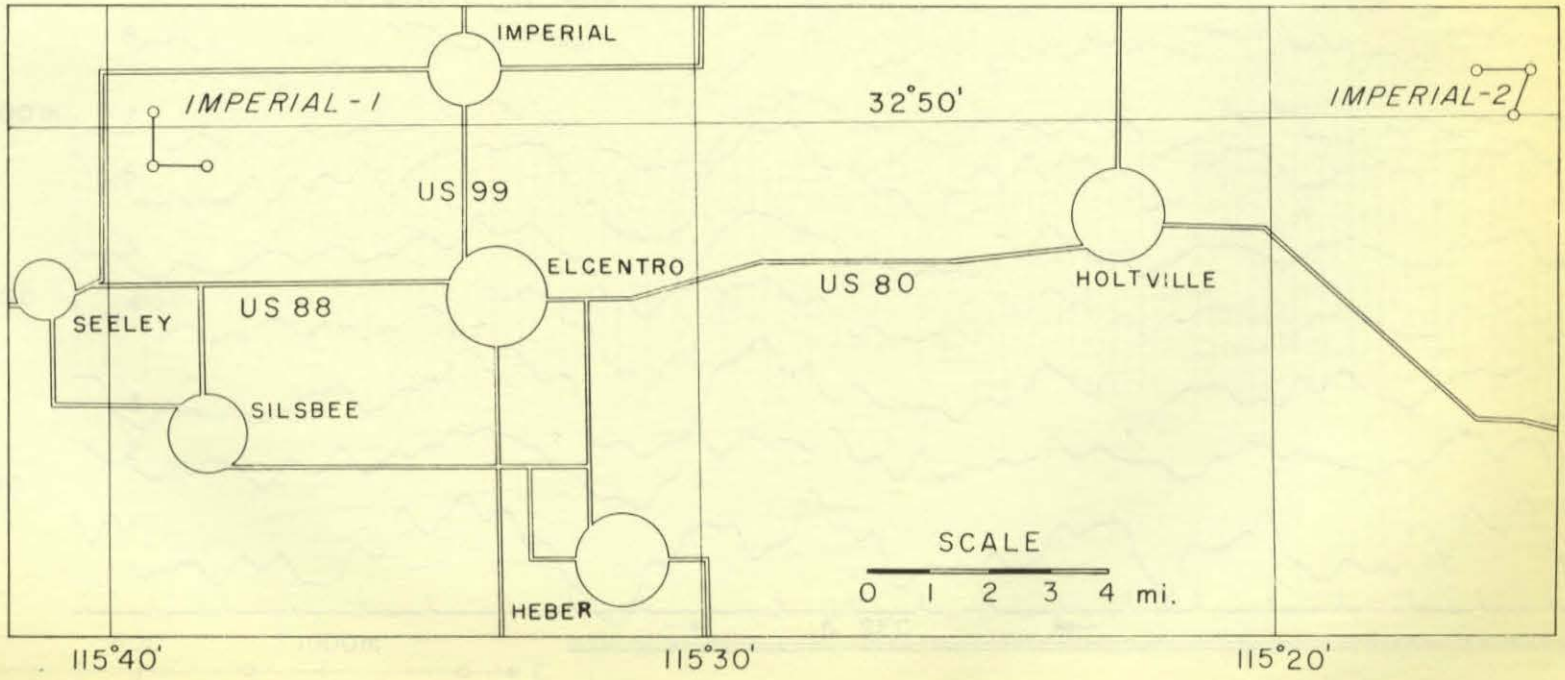
IMPERIAL
IMPERIAL - 1
32°50'
IMPERIAL-2
US 99
ELCENTRO
US 80
HOLTVILLE
SEELEY
US 88
SILSBEE
SCALE
0 1 2 3 4 mi.
HEBER
115°40'
115°30'
115°20'

Fig. 17

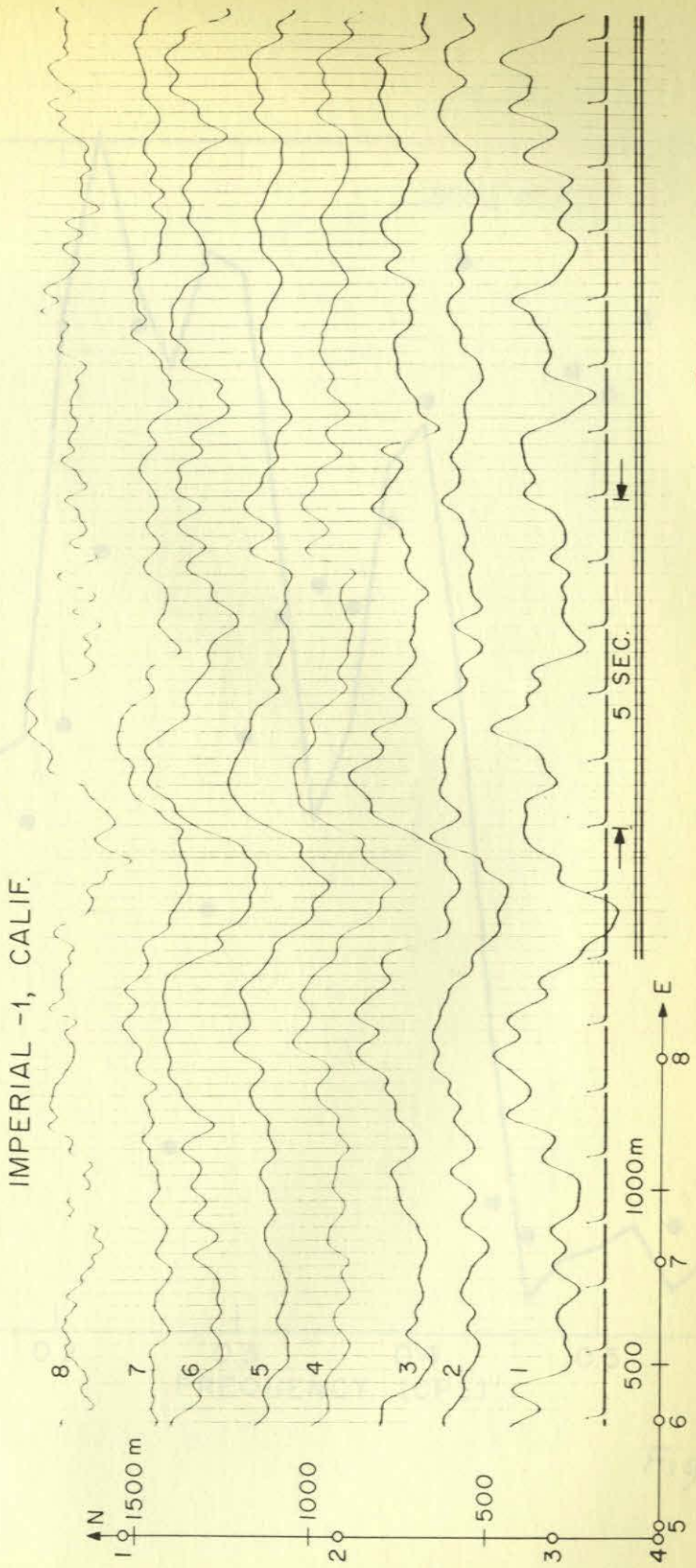
IMPERIAL -1, CALIF.
8
7
6
5
4
3
2
1
5 SEC.
N
1500 m
1000
500
1
2
3
4
500
1000m
5
6
7
8
E

Fig. 18

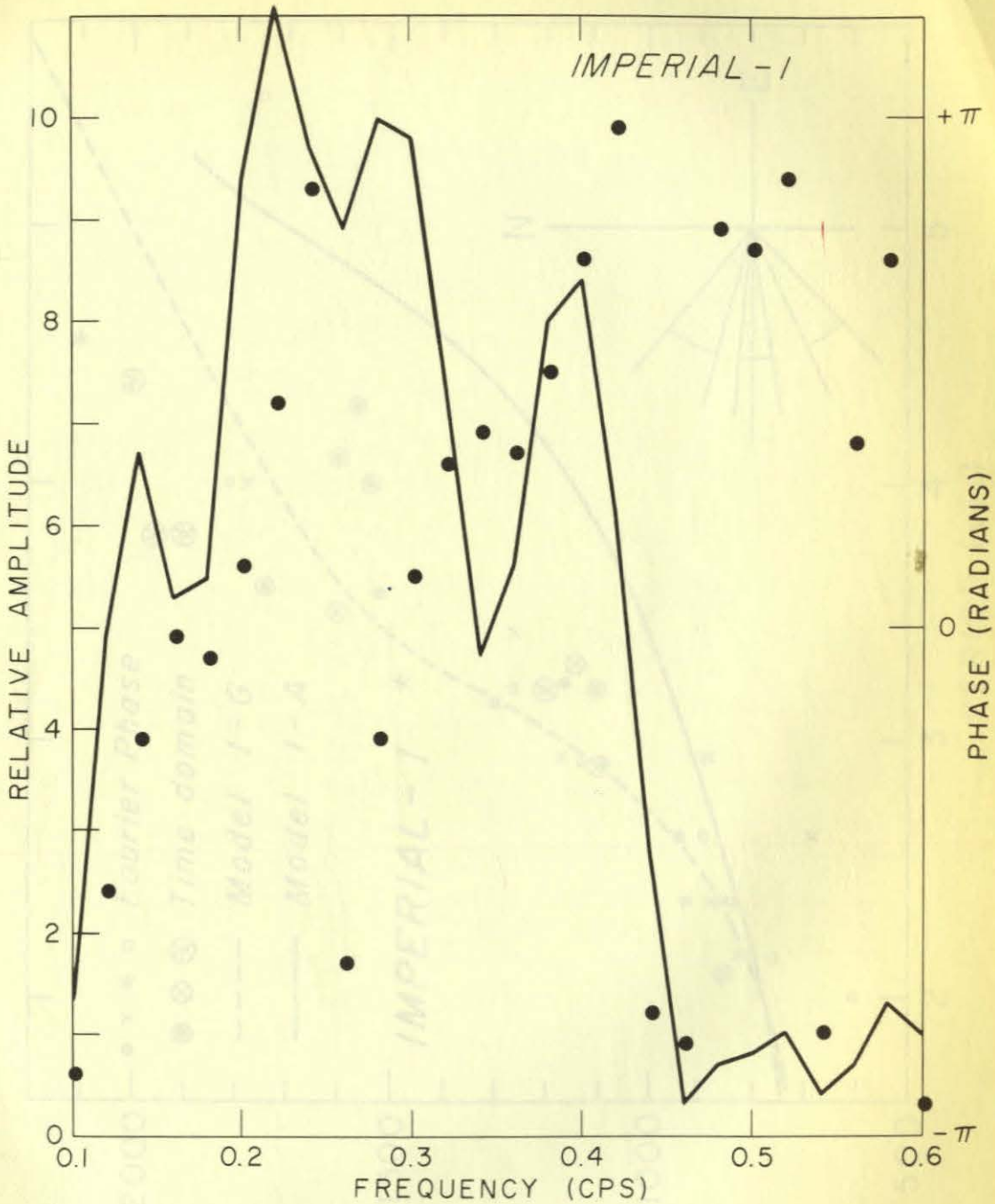
IMPERIAL - 1
RELATIVE AMPLITUDE
PHASE (RADIANS)
FREQUENCY (CPS)
0
2
4
6
8
10
0.1
0.2
0.3
0.4
0.5
0.6
+π
0
-π

Fig. 19

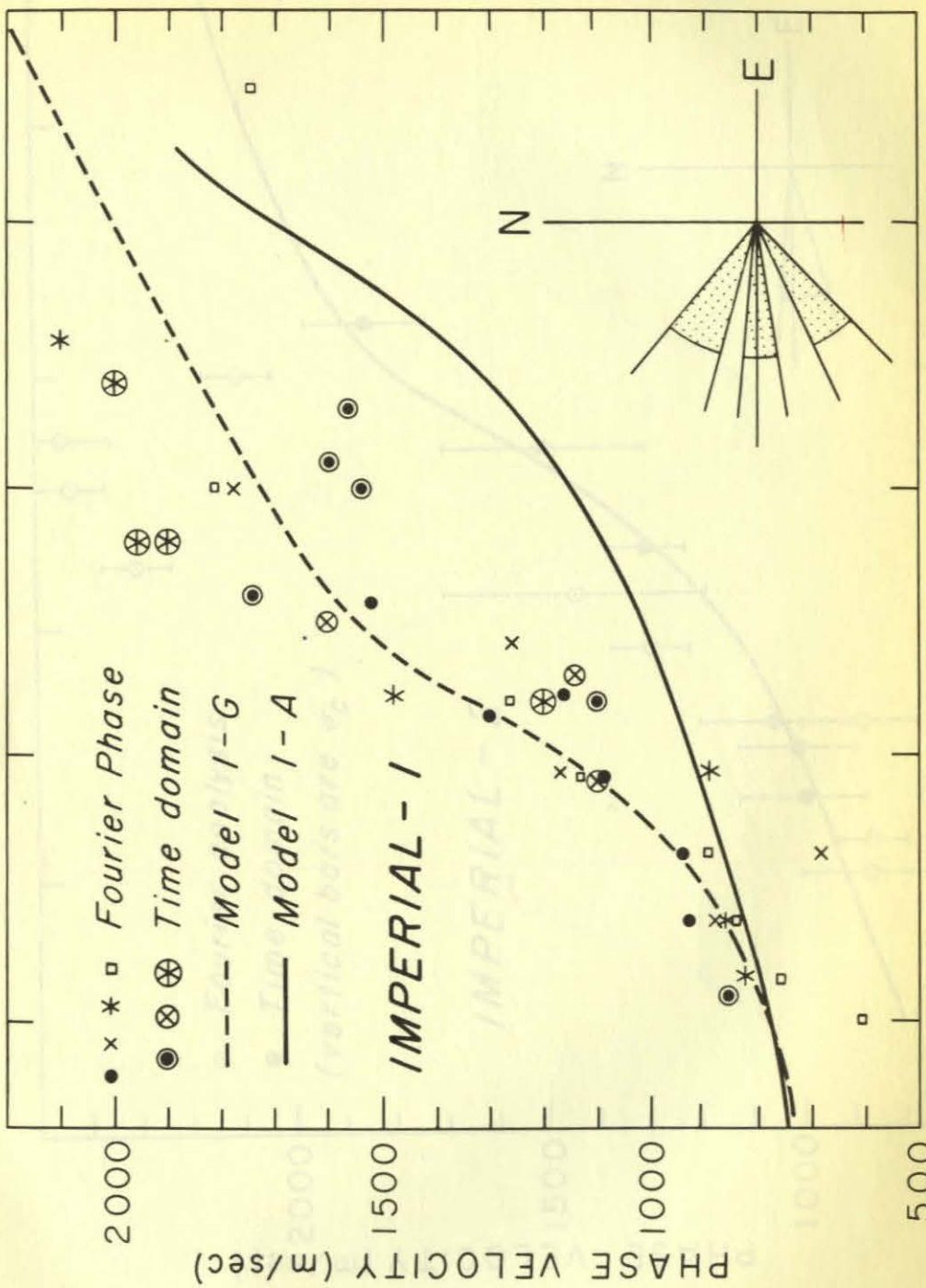
PHASE VELOCITY (m/sec)
2000
1500
1000
500
PERIOD (sec)
2
3
4
5
IMPERIAL - I
Fourier Phase
Time domain
Model I-G
Model I-A
N
E

Fig. 20

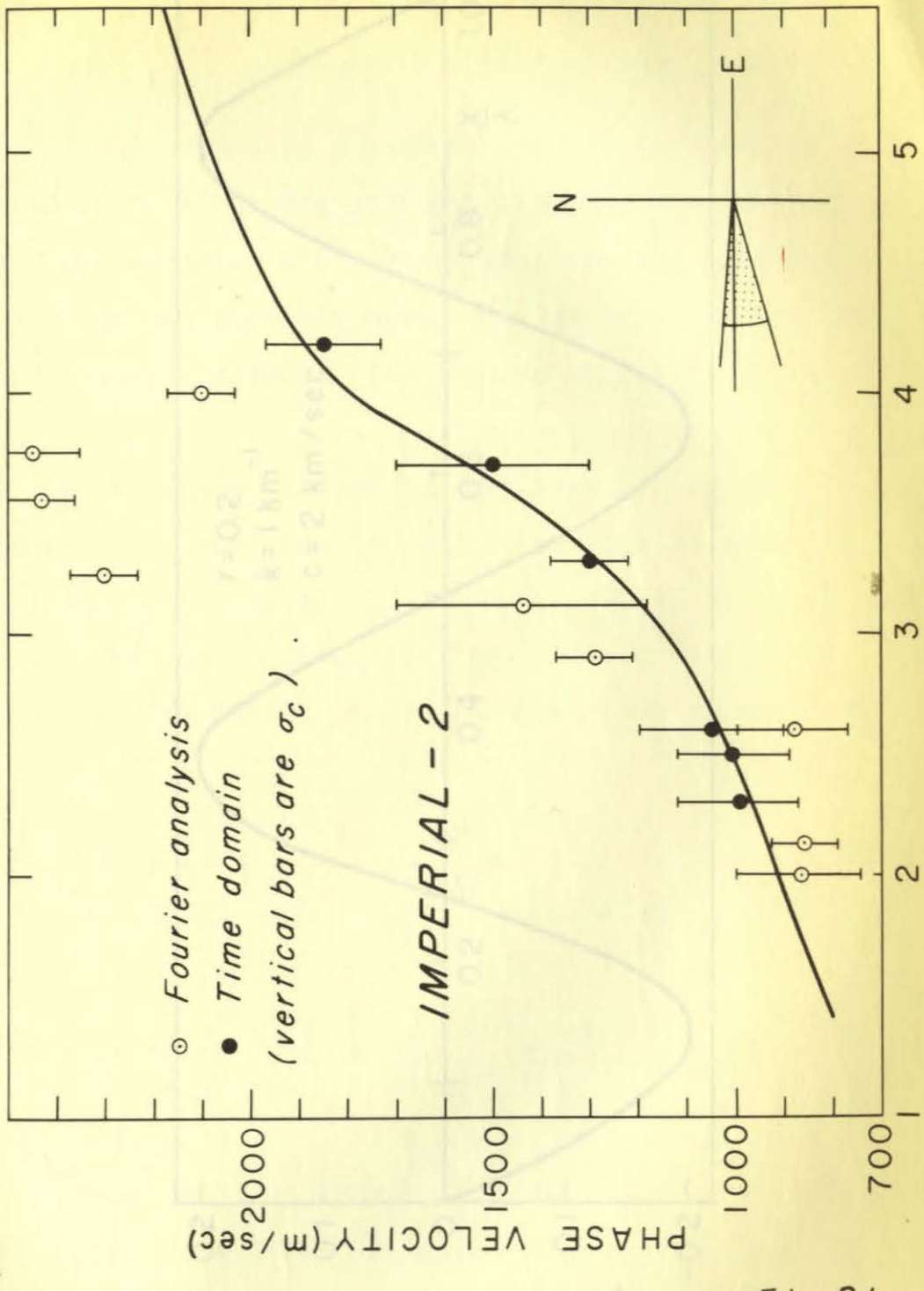
PHASE VELOCITY (m/sec)
2000
1500
1000
700
1
2
3
4
5
PERIOD (sec)
N
E
IMPERIAL - 2
○ Fourier analysis
● Time domain
(vertical bars are σ_c)

Fig. 21

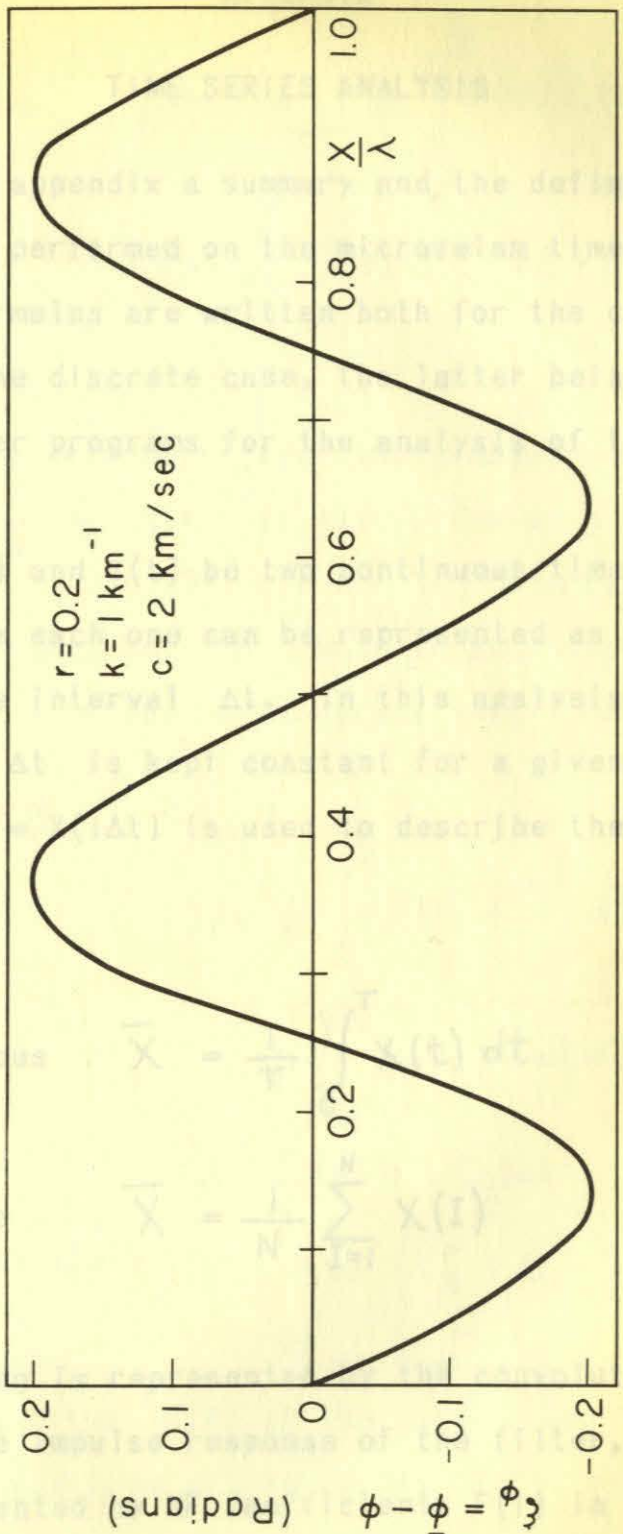

Fig. 22

APPENDIX

TIME SERIES ANALYSIS

In this appendix a summary and the definitions of the operations performed on the microseism time series are given. The formulas are written both for the continuous case and for the discrete case, the latter being the form used in computer programs for the analysis of the digital data.

Let $X(t)$ and $Y(t)$ be two continuous time functions. In digital form each one can be represented as a series sampled at some interval Δt. In this analysis, as in most applications, Δt is kept constant for a given series. The notation $X(I) = X(I\Delta t)$ is used to describe the sampled function.

Mean

Continuous $$\overline{X} = \frac{1}{T}\int_0^T X(t)\,dt$$

Discrete $$\overline{X} = \frac{1}{N}\sum_{I=1}^{N} X(I)$$

Filter

Filtering is represented by the convolution integral. Let $F(t)$ be the impulse response of the filter, and let this be represented by NF coefficients $F(I)$ in digital form.

The filtered wave X(t) is

Continuous $$X_f(\tau) = \lim_{T\to\infty} \frac{1}{T} \int_{-\frac{T}{2}}^{\frac{T}{2}} F(t)\, X(\tau - t)\, dt$$

Discrete $$X_f(J) = \sum_{I=1}^{NF} F(I)\, X(J+I-1)$$

Taper

To smooth the end of the time windows before Fourier analysis, the series X(I) is multiplied by a cosine taper of the form $\frac{1}{2}(1 - \cos k\pi)$, k = 0 - 1. This taper is similar to "hanning" window, but its length is adjustable and a variable fraction of the total record length may be tapered.

Fourier Transform

Continuous $$F(\omega) = \frac{1}{T} \int_{-\frac{T}{2}}^{\frac{T}{2}} X(t)\, e^{-i\omega t}\, dt$$

$$= \frac{1}{T} \int_{-T/2}^{T/2} X(t) \left[\cos\omega t + i \sin\omega t\right] dt$$

$$= C_c(\omega) + i\, C_s(\omega)$$

Amplitude $$A = \left(C_c^2 + C_s^2\right)^{\frac{1}{2}}$$

Phase $$\varphi = \tan^{-1} \frac{C_s}{C_c}$$

Discrete: Let F(K) be the independent spectral estimates obtained from a time series X(I) of (L + 1) samples.

$$F(K) = \frac{1}{L}\left\{\left[X(1) + 2\sum_{I=2}^{L} A(I)\cos\frac{(I-1)(K-1)}{L}\pi + A(L+1)\cos(K-1)\pi\right]\right.$$

$$\left. + i\left[2\sum_{I=2}^{L} A(I)\sin\frac{(I-1)(K-1)}{L}\pi + A(L+1)\sin(K-1)\pi\right]\right\}$$

Correlation

Assume that the time functions X(t) and Y(t) are stationary in the wide sense. The correlation functions would be independent of the time of origin.

Continuous

Autocorrelation

$$R_{xx}(\tau) = \lim_{T\to\infty}\frac{1}{2T}\int_{-T}^{T} X(t)\,X(t+\tau)\,dt$$

Cross-correlation

$$R_{xy}(\tau) = \lim_{T\to\infty}\frac{1}{2T}\int_{-T}^{T} X(t)\,Y(t+\tau)\,dt$$

$$R_{yx}(\tau) = \lim_{T\to\infty}\frac{1}{2T}\int_{-T}^{T} Y(t)\,X(t+\tau)\,dt$$

Discrete

If N is the total number of samples in a time series, then

$$R_{xx}(K) = \frac{1}{N-K}\sum_{I=1}^{N-K+1} X(I)\,X(I+K-1)$$

$$R_{xy}(K) = \frac{1}{N-K}\sum_{I=1}^{N-K+1} X(I)\,Y(I+K-1)$$

$$R_{yx}(K) = \frac{1}{N-K}\sum_{I=1}^{N-K+1} Y(I)\,X(I+K-1)$$

Properties of the correlation functions

$$R_{xx}(0) = \langle X^2 \rangle = \text{mean intensity of the wave}$$

$$R_{xx}(\tau) = R_{xx}(-\tau)$$

$$R_{xy}(-\tau) = R_{yx}(\tau)$$

Power Spectra

The Fourier transform of the auto- and cross-correlation functions are called spectra and cross-spectra, respectively.

$$S_{xx}(\omega) = \int_{-\infty}^{\infty} R_{xx}(\tau)\, e^{-i\omega\tau}\, d\tau$$

$$S_{xy}(\omega) = \int_{-\infty}^{\infty} R_{xy}(\tau)\, e^{-i\omega\tau}\, d\tau$$

S_{xx} is real, but S_{xy} has real and imaginary parts:

$$S_{xy}(\omega) = C_{xy}(\omega) + i\, Q_{xy}(\omega)$$

where C is co-spectrum and Q is quadrature spectrum. From the properties of cross-correlation function

$$S_{xy}(\omega) = S^{*}_{yx}(\omega)$$

where $*$ represents the complex conjugate.

Between X(t) and Y(t)

Coherence $$R(\omega) = \left[\frac{S_{xy} \cdot S_{yx}}{S_{xx}\, S_{yy}}\right]^{\frac{1}{2}} = \left[\frac{C_{xy}^2 + Q_{xy}^2}{S_{xx}\, S_{yy}}\right]^{\frac{1}{2}}$$

Phase

$$\varphi_{xy}(\omega) = \tan^{-1}\left(\frac{Q_{xy}}{C_{xy}}\right)$$

The cross-spectra are normally written as a matrix. For the 8-channel microseism array the spectral density matrix for each frequency is

$$S = \begin{bmatrix} S_{1,1} & S_{1,2} & S_{1,3} & S_{1,4} & S_{1,5} & S_{1,6} & S_{1,7} & S_{1,8} \\ S_{2,1} & S_{2,2} & S_{2,3} & S_{2,4} & S_{2,5} & S_{2,6} & S_{2,7} & S_{2,8} \\ S_{3,1} & S_{3,2} & S_{3,3} & S_{3,4} & S_{3,5} & S_{3,6} & S_{3,7} & S_{3,8} \\ S_{4,1} & S_{4,2} & S_{4,3} & S_{4,4} & S_{4,5} & S_{4,6} & S_{4,7} & S_{4,8} \\ S_{5,1} & S_{5,2} & S_{5,3} & S_{5,4} & S_{5,5} & S_{5,6} & S_{5,7} & S_{5,8} \\ S_{6,1} & S_{6,2} & S_{6,3} & S_{6,4} & S_{6,5} & S_{6,6} & S_{6,7} & S_{6,8} \\ S_{7,1} & S_{7,2} & S_{7,3} & S_{7,4} & S_{7,5} & S_{7,6} & S_{7,7} & S_{7,8} \\ S_{8,1} & S_{8,2} & S_{8,3} & S_{8,4} & S_{8,5} & S_{8,6} & S_{8,7} & S_{8,8} \end{bmatrix}$$

From the properties of the cross-spectral elements, it is obvious that S is a Hermitian matrix.